8-2010

Dynamic Chemical Shift Imaging for Image-Guided Thermal Therapy

Brian A. Taylor

Recommended Citation

DYNAMIC CHEMICAL SHIFT IMAGING FOR IMAGE-GUIDED THERMAL THERAPY

A

DISSERTATION

Presented to the faculty of
The University of Texas
Health Science Center at Houston
and
The University of Texas
M. D. Anderson Cancer Center
Graduate School of Biomedical Sciences
in Partial Fulfillment
of the Requirements
for the degree of

DOCTOR OF PHILOSOPHY

by

Brian Allen Taylor, B.S.
Houston, Texas
August 2010

iii

Do your best to present yourself to God as one approved, a workman who does not need

to be ashamed and who correctly handles the word of truth.

2 Timothy 2:15 (NIV)

Acknowledgements

There are many people who contributed to this dissertation. First of all, I would like to thank my advisor, Dr. Jason Stafford, for the countless hours of guidance and encouragement he has given me over the past four years. I greatly benefitted from his constant motivation to grow as a scientist. I'm very blessed to be able to work with him.

I would also like to thank the people who served on my committees throughout my time in graduate school. Dr. John Hazle provided expert guidance on my lab work and presentations which was a tremendous help throughout my time in the lab. I am thankful for his leadership in the department and his commitment to education to which I am a beneficiary of. Dr. Ed Jackson also provided valuable leadership to the education program. I am very thankful for his time and commitment to students. In addition, I would like to thank him for his efforts on the T32 grant (T32CA119930). Much of this work may not have been possible without his support and for that I am greatly appreciative. I would also like to thank Drs. Ma and White for their valuable input throughout the process of completing this dissertation research. Drs. Bankson and Wendt were key in helping my project get started through serving on my advisory and/or examination committees. I am very appreciative of their guidance.

There are also many people in the lab and department I would like to thank. Dr. Ken Hwang of GE Healthcare provided critical support for many MR acquisition issues. Dr. Andrew Elliott provided countless hours of support on thermal therapy experiments. I am very thankful for his help and patience during many long experiments in the MR

room. Drs. Fuentes, Shetty and Melancon as well as Josh Yung and Adam Springer provided crucial support for me in the lab. I really enjoyed working with each one of you. I'm also thankful for the opportunity to work with Hua Ai, Marie Feng, Samuel Fahrenholtz, and Sina Najmaei who applied part of this work to their own projects.

I would also like to thank the friends who supported me during my time in graduate school. Specifically, I am so thankful for the friends I've met at Second Baptist Church. You are truly friends whom I hope to know for a lifetime. Last but certainly not least, I would like to thank my family who provided continuous love and support as I pursue my graduate studies far away from home. I would not be where I am today without you.

DYNAMIC CHEMICAL SHIFT IMAGING FOR IMAGE-GUIDED THERMAL THERAPY

Brian Allen Taylor, B.S.

Supervisory Professor: R. Jason Stafford, Ph.D.

Magnetic resonance temperature imaging (MRTI) is recognized as a noninvasive means to provide temperature imaging for guidance in thermal therapies. The most common method of estimating temperature changes in the body using MR is by measuring the water proton resonant frequency (PRF) shift. Calculation of the complex phase difference (CPD) is the method of choice for measuring the PRF indirectly since it facilitates temperature mapping with high spatiotemporal resolution. Chemical shift imaging (CSI) techniques can provide the PRF directly with high sensitivity to temperature changes while minimizing artifacts commonly seen in CPD techniques. However, CSI techniques are currently limited by poor spatiotemporal resolution.

This research intends to develop and validate a CSI-based MRTI technique with intentional spectral undersampling which allows relaxed parameters to improve spatiotemporal resolution. An algorithm based on autoregressive moving average (ARMA) modeling is developed and validated to help overcome limitations of Fourier-based analysis allowing highly accurate and precise PRF estimates. From the determined acquisition parameters and ARMA modeling, robust maps of temperature using the k-means algorithm are generated and validated in laser treatments in *ex vivo* tissue. The use of non-PRF based measurements provided by the technique is also investigated to aid in the validation of thermal damage predicted by an Arrhenius rate dose model.

Table of Contents

List of Figures

List of Tables

Chapter 1: Introduction

1.1 Thermal Therapies

Thermal therapies generally encompass all treatments based on the transfer of thermal energy out of or into the body. The overall objective of these therapies is to deliver a desired thermal dose to a target while minimizing the dose to normal tissues (1). The use of thermal energy in medicine is not a new concept. During the reign of the Roman Empire, facilities were created which contained hot baths in addition to the use of dry and humid heat to treat diseases. An Egyptian papyrus, dated at approximately 3000 BC, described the use of heat in surgery and is possibly the earliest manuscript known in thermal therapy. In the nineteenth and twentieth centuries, "fever therapy" was investigated to improve the immune response in certain pathologies (2).

The more modern discipline of thermal therapies came mostly from laboratories in the 1970s that were interested in radiation biology and how temperature affects the radio-sensitivity of cells (3). A number of cell culture and *in vivo* tumor model studies showed a cell-killing effect at temperatures above 41 °C (4). It was also found that the exposure time to kill cells was shorter when higher temperatures were used. In the 1980s, key studies were reported that assessed the efficacy of thermal therapies (4-7). The concept of thermal dosimetry was also introduced (8).

Although there were modest improvements in the ways to deliver heat into tissues, the enthusiasm for these treatments dwindled in the 1990s. According to a review published in 2006 by Habash (1),

> "The problem that was faced by the thermal-therapy community at that juncture was unrealistic thermal goals because of lack of adequate equipment for delivering thermal treatment and *inability to measure the treatment delivered*. A combination of the above difficulties is still a challenge to the design and implementation of successful clinical trials."

Since the publication by Habash, there have been improvements in the delivery and monitoring of these therapies (3). However, Habash's review underscores the importance of monitoring in order for thermal therapies to be effective.

Thermal therapies are typically divided into three categories. In the low temperature range, cryotherapy is used to freeze tissue with the goal of necrosis (9). Hyperthermia is used where the temperature at a region of the body or the whole body is raised to temperatures up to approximately 45 °C for an extended period of time (minutes to hours) (10). Another category is thermal ablation where very high temperatures (typically >50 °C) are used to destroy tissue in a conformal setting (3).

The main biological rationale for thermal therapies is based on cell-killing (4). Studies have shown that protein denaturation is the most likely mechanism that causes permanent damage to tissue (4, 11-14). When proteins denature, they are prone to aggregation. Without any molecular chaperones to aid in refolding the proteins, these aggregated proteins can affect the structure and function of many macromolecules that are vital for the cell's survival (4, 15).

The aggregation of proteins caused by hyperthermic temperatures is thought to be key to cells being more sensitive to radiation (12) and the efficacy of using both radiation

and thermal therapy is higher the closer the two are given in time.   If there is a delay of radiation after thermal treatment, heat shock protein levels are higher and more proteins are repaired and less aggregated making the cells more insensitive to radiation (16). There is also an additive effect using hyperthermia and radiation.   Cells which are hypoxic, have low pH values, and are in the S-phase in the cell cycle are sensitive to heat and are relatively resistant to radiation.   Hyperthermia can also increase the blood perfusion into cells thereby decreasing hypoxia and making the cells more radiosensitive (17).

Hyperthermia has also been shown to increase the efficacy of some drugs, including chemotherapeutic drugs (18).   Drugs that have chemical, rate-limiting reactions are expected to be more efficient at higher temperatures due to thermodynamic principles. For example, cisplatin alkylates DNA at a higher rate at higher temperatures, thereby increasing its efficacy (19). As with radiation therapy, the increase in blood flow in the tumor causes increased drug uptake and concentration which can aid in cell-killing (18).

Hyperthermia has been studied used as an adjuvant in gene and immuno-therapies. Gene therapy is defined as a treatment where genetic material is infused to cells to modify cellular function. In cancer treatment, the material must affect cells associated with the tumor and not in normal tissue. It must also not drastically affect the immune system in the infected patient. Studies have shown that gene-infected cells are more sensitive to hyperthermia. The increased temperature is expected to open the pores

of blood vessels to allow more genetic material to reach the tumor cells. It also increases the protein production in the affected cells and enhances the immune system's ability to send the infected cells to the tumor (20-23).

In hyperthermia, it is important to note the narrow temperature ranges that are needed for combination treatments with radiation and chemotherapy (24). This makes the accurate and precise monitoring of temperature *in vivo* very important. If a certain temperature is needed as an adjuvant to a therapy and going too high or too low in temperature can affect outcomes, then it is very important to have precise and accurate monitoring.

The goal of thermal ablation is to destroy a lesion using a high dose of thermal energy (above 50 °C) in a minimally-invasive way without damaging vital nearby structures. While protein denaturation does occur in this higher temperature range, and at a faster rate than seen in hyperthermia, the main effect seen in these therapies is coagulative necrosis. This has been studied as an alternative or adjuvant to conventional surgery and can be used in conjunction to other treatments, such as chemotherapy and radiation therapy, to treat localized disease. It can be a repeatable procedure and may be suited for patients who are not good candidates for open surgery. There are also various modalities to deliver heat to the target including focus ultrasound (FUS), radiofrequency (RF) applicators, microwaves, and lasers. The rapid heating of tissues to ablative temperatures requires fast monitoring in order to control the treatment, conform to the target and minimize thermal dose to critical normal structures (3).

4

In thermal therapies, it is important to model and determine where the thermal damage has occurred to verify that the target lesion has been successfully treated. Thus, damage prediction models have been developed to aid in treatment verification. In one of the seminal papers on thermal damage, Henriques studied the thermal damage in pig skin (25). He showed that the thermal damage from the denaturation of proteins follows an Arrhenius rate process. The rate process can be described as a rate-of-formation kinetic model of reaction products in a biochemical reaction. Briefly, molecules like proteins in their native state, C, must reach an energy barrier, E_a, to be activated, C^*, at a rate k_a. Some will relax back to the native state while some will denature at rate k_d. This denaturation rate can be described as

$$k_d = \frac{RT}{N\hbar} e^{\frac{-\Delta G^*}{RT}} \qquad (1.1)$$

where R is the universal gas constant (8.315 JK^{-1}mol^{-1} or 2.0 cal K^{-1}mol^{-1}), T is the temperature, N is Avogandro's number, and $\hbar$ is Plank's constant. The speed of the reaction is governed by Gibb's free energy of formation, ΔG^*. $\Delta G^* = \Delta H^* - T \Delta S^*$ where ΔH^* is the enthalpy of activation and ΔS^* is the entropy of activation. ΔH^* has an activation energy, E_a, where $\Delta H^* = E_a - nRT$ and n is the order of the reaction. $E_a >> RT$, thus

$$k_d = \frac{RT}{N\hbar} e^{\frac{-\Delta H^*}{RT}} e^{\frac{\Delta S^*}{R}} = Ae^{\frac{-\Delta H^*}{RT}} = Ae^{\frac{-E_a}{RT}} \qquad (1.2)$$

k_d can be expressed by a first-order Bernoulli differential equation where

$$-\frac{d[C]}{dt} = k_d[C] \qquad\qquad (1.3)$$

and

$$\Omega = \ln\left[\frac{C(0)}{C(t)}\right] = A\int_0^t e^{\frac{-E_a}{RT(\tau)}}d\tau \qquad\qquad (1.4)$$

where A is the frequency factor and $T(\tau)$ is the temperature in degrees Celsius as a function of time, τ (26).   Henriques selected rate coefficients so complete cellular damage is indicated by an Ω value of unity. Subsequent studies followed the one reported by Henriques and investigated parameters for various temperature ranges and tissues (27).

Almost 40 years later, Separato and Dewey proposed a method of measuring thermal dose as an unit of time at 43 °C (8). The cumulative time equivalent at 43 °C, t_{43}, can be described as

$$t_{43} = \sum_{t=0}^{t_f} R^{(43-\bar{T})}\Delta t \qquad\qquad (1.7)$$

where t_f is the final time point, $\bar{T}$ is the average temperature at time interval Δt, and R is a constant (R=0.25 below 43 °C and R=0.5 at 43 °C and above).

The dependence of accurate and precise temperature measurements are evidently seen in these models. Not only does the temperature need to be ascertained but also the temperature history over several time points. This makes temperature monitoring very

6

important to accurately determine if and where thermal damage has occurred. A temperature error of 1 °C over several minutes can cause the estimated thermal dose to be different than what was actually delivered. This may cause an over-treatment or under-treatment of the target. In addition, rapid monitoring is especially needed for high-temperature ablations to assure that temperatures are high enough to ablate the target as well as to make sure nearby critical structures receive nonlethal thermal doses. This calls for accurate and precise methods to measure temperature noninvasively to aid in assuring that an acceptable thermal dose is delivered. This is where image-guidance becomes important.

1.2   Image-Guidance of Thermal Therapies

Image-guidance has been shown to be critical in thermal therapies by providing localization, planning, and post-treatment verification. In addition, image-guidance provides the potential for real-time monitoring during treatment delivery which can help better conform thermal doses to the target while avoiding nearby critical structures and healthy tissue (28).

Ultrasound (US) (29), computerized tomography (CT) (30), and magnetic resonance (MR) (31) are imaging modalities which are capable of temperature feedback during thermal therapy procedures. Of these three modalities, MR has the desired properties of providing adequate localization, planning, and post-treatment verification using its wealth of soft-tissue contrast mechanisms without the use of ionizing radiation. MR can provide fast imaging in any plane. Most importantly for temperature monitoring,

MR is fundamentally temperature sensitive since both the relaxation properties and chemical environment of the spin system are tied to thermally dependent processes (32). As a result, magnetic resonance temperature imaging (MRTI) is recognized as a primary way to non-invasively provide rapid, quantitative temperature imaging in various tissues in order to provide useful thermal dosimetry and monitoring for thermal therapy procedures (33).

The most commonly employed quantitative MRTI method is based on the proton resonant frequency (PRF) shift (34-36), which has been established and validated as a technique for monitoring temperature changes for feedback and control of thermal therapies in a variety of anatomical sites (37). A fast complex phase difference (CPD) method (38) has been the preferred method to estimate the PRF shift indirectly. A major advantage of CPD techniques for PRF-based thermometry is its high spatial and temporal resolution ($\sim$1.5x1.5x4 mm^3, $\leq$5 sec (39)). However, there are several well-known limitations in this technique. Intravoxel lipid contamination (40, 41), inter- and intra-scan motion (42), tissue susceptibility changes (43) and static magnetic field drifts (44) are artifacts that are commonly encountered.

An alternative to CPD methods is a direct method of measuring PRF shift via chemical shift imaging (CSI) techniques (45-48), which has several advantages over CPD techniques. One is that the water proton resonant frequency is measured separately from other resonances whereas CPD measures the mixture of frequency components in each voxel resulting in a variable response. This immediately relieves the problem of

8

intravoxel lipid contamination, which requires saturation or suppression techniques in CPD. Also, the lipid signal can be used as an internal reference to account for field drifts, susceptibility and motion since it is relatively insensitive to temperature (37).

Researchers have developed CSI techniques to reduce artifacts seen in CPD techniques. However, these studies have constrained themselves in both sensitivity and spatiotemporal resolution by using interleaved shots to increase the spectral bandwidth to adequately sample the MR signal and keep peaks such as lipid unaliased in the spectra (45-47). In addition, high receiver bandwidths are often used to shorten the echo-readouts, and as an additional benefit, increases the spectral bandwidth to avoid aliasing. Use of these high bandwidths decreases the SNR and reduces the sensitivity of these techniques (45-47). A high echo-train length (ETL) has also been used to implement Fourier-based spectral analysis, which also degrades spatiotemporal resolution (46, 47).

The proposed research is intended to build upon and address areas involved in image acquisition and frequency estimation that has limited CSI techniques for MRTI. We propose that by carefully undersampling the MR signal, which causes aliasing of the lipid peak, we can allow lower receiver bandwidths to maintain a higher SNR at higher spatiotemporal resolutions than previously reported. In addition, it is hypothesized that, even with these relaxed parameters, the spatial, temporal and spectral resolutions currently used for temperature monitoring will not be severely degraded using advanced spectral processing techniques. Traditionally, 32 or greater samples have been acquired so frequency estimates can be reliably performed using a fast Fourier transformation

9

(FFT) (45-47).   The increased number of samples comes at a cost of spatiotemporal resolution.   Time-domain, frequency domain, and z-domain (via the z-transform) approaches to spectral estimation have been shown to accurately measure frequencies with limited amounts of data when a priori information of the signal is known (49). It has been recognized that an ideal NMR signal is characterized as an autoregressive (AR) process and a noisy NMR signal as an autoregressive moving average (ARMA) process (50). It is expected that an ARMA modeling approach will be more robust than Fourier transformation since the model accounts for both exponential decay and noise (50).   The autoregressive property of the signal can be used to directly model the parameters of the signal including the PRF of each specimen in the signal.   Other parameters, such as the amplitude and damping factor (apparent spin-spin relaxation time, T_2^*) of each peak can be simultaneously determined (50-54).

There are several potential advantages of implementing the proposed acquisition parameters and spectral processing algorithms (ARMA modeling).   One possible advantage is increased sensitivity to temperature changes compared to CPD techniques. By collecting more echoes during the same repetition time (TR) period as the single-echo CPD (38), this technique could potentially produce more accurate temperature estimates with lower uncertainty.   Additionally, the technique not only provides the ability to remove lipid signal across the volume without suppression or saturation pulses, but also provides the potential opportunity to use lipid as an internal reference for artifact suppression for increased accuracy and precision.

There also lies the opportunity with a model-based methods of observing both the T_1-W images and T_2* maps from each chemical specimen in addition to the PRF thereby providing multi-parametric monitoring of the treatment target. This potentially culminates into an enhanced MRTI technique compared to what is now available. In addition, all of this can be performed without dramatically sacrificing spatiotemporal resolution, which is critical for monitoring thermal therapies.

1.3 Hypothesis and Specific Aims

The hypothesis of this work is that through the use of a multi-gradient echo acquisition coupled with model-based spectral processing algorithms, CSI-based temperature maps utilizing this method can be generated with higher accuracy and precision compared to standard CPD techniques without sacrificing spatiotemporal resolution. The specific aims of this work are to:

1) Develop, validate and characterize via simulation a model-based spectral analysis algorithm for detection of water and lipid spectral frequencies with $\leq$ 1.0 °C accuracy and uncertainty.

2) Investigate the influence of various MR acquisition parameters on the sensitivity of detecting water and lipid frequency changes at high spatiotemporal resolutions for temperature imaging

3) Combine these approaches to acquisition and processing in order to develop and validate 2D temperature mapping techniques for generating more accurate and precise temperature estimates compared to CPD in phantom and *ex vivo* tissues.

To accomplish these goals, a model-based spectral processing algorithm was developed to accurately measure the PRF of each peak in a spectrum using a constrained number of echoes to maintain spatiotemporal resolution. This technique was validated using simulation over a range of SNR values and physiologically relevant water/lipid spectral parameters. An appropriate range of acquisition parameters providing highly sensitive PRF estimates in a rapid acquisition with adequate spatiotemporal resolutions were determined (Chapter 4). Heating experiments were performed in a water/lipid phantom as well as *ex vivo* bone marrow, brain, kidney, liver, and prostate tissue to validate the accuracy and precision of the temperature measurements as well as measure the dependence of T_2* and T_1-W amplitudes as a function of temperature (Chapter 5). Finally, a mapping algorithm that utilizes the k-means clustering algorithm was developed and validated to effectively provide a means by which to map water and lipid spectral parameters separately to aid in temperature mapping (Chapter 5).
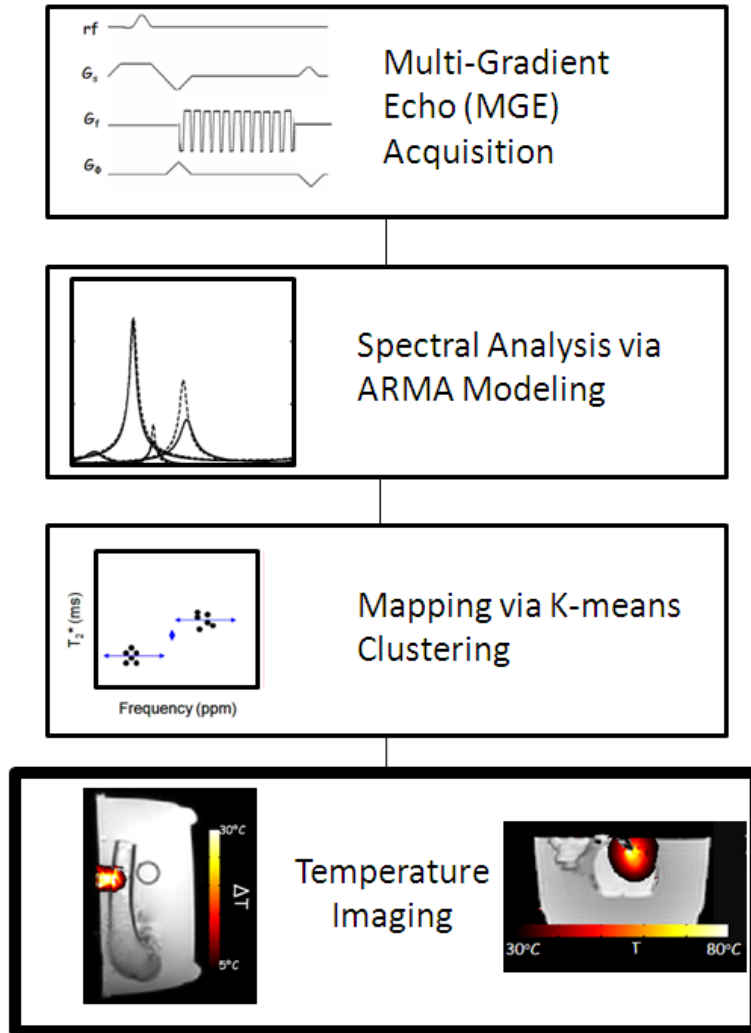
Figure 1-1 Approach for rapid MR temperature imaging

Data collected from a high spatiotemporal resolution MGE acquisition was processed via ARMA modeling to calculate multiple spectral parameters (PRF, T_2^*, amplitude). These parameters were inputs to a k-means clustering algorithm to separate chemical species such as water and lipid which were used to create highly accurate and precise temperature images.

Chapter 2:   Magnetic Resonance Temperature Imaging

2.1 *Introduction*

MR is a fundamentally temperature-sensitive modality since the relaxation properties of a spin system and local chemical environment are fundamentally thermodynamic processes (32). Therefore, multiple temperature-sensitive parameters are available; however, not all are equally useful for guiding thermal therapies. In this chapter, temperature-sensitive MR parameters will be reviewed. Focus will be given to the use of the proton resonant frequency (PRF) shift for temperature imaging, the dominant technique, via complex phase difference (CPD) and chemical shift imaging (CSI) techniques.

2.2 *The Temperature Sensitivity of Intrinsic MR Parameters*

There are a number of MR parameters intrinsic to tissue that can be exploited for temperature measurements. Chief among them at clinical field strengths are diffusion of water, proton density of water, T_1 and T_2 relaxation times, magnetization transfer, and the PRF shift.

2.2.1 *MOLECULAR DIFFUSION OF WATER*

In MR, the diffusion coefficient, *D*, is used to describe the thermal Brownian motion of molecules (55). The relationship of *D* to temperature is

$$D \approx e^{-E_a(D)/kT} \tag{2.1}$$

where $E_a(D)$ is the activation energy of the diffusion of water. From differentiation, the temperature dependence of water diffusion can be described as

$$\frac{dD}{dT} = \frac{E_a(D)}{kT^2} e^{-E_a(D)/kT} \qquad (2.2)$$

Therefore, if two diffusion measurements, D_T and $D_{T+\Delta T}$, are made at temperatures T and T+ΔT, then the temperature change will be

$$\Delta T = \frac{kT^2}{E_a(D)} \left(\frac{D_{T+\Delta T} - D_T}{D_T} \right) \qquad (2.3)$$

where it is assumed that $E_a(D)$ does not change with temperature.

In the clinical application of MRTI, the temperature sensitivity is quite high at about 2%/°C (33). However, the temporal resolution is relatively low and measurements can be highly sensitive to motion. Line-scan (56) and single shot echo-planar imaging (EPI) (57) has helped in reducing imaging time and in reducing artifacts due to motion. Also the use of the diffusion coefficient is independent of field strength.

A compounding factor is observed when physiological changes occur in the tissue during the thermal delivery. For instance, edema, protein denaturation and thermal coagulation can change the diffusion coefficient and these events are difficult to isolate from temperature changes (58). It is also important to note that diffusion can be anisotropic such as in white matter tracts in the brain and muscle fibers. Therefore, for accuracy, the tensor that describes the anisotropic diffusion needs to be measured which

increases the imaging time. It has been noted in a recent review that temperature measurements in adipose tissue using the diffusion coefficient is difficult due to the low values in lipid and different sensitivity compared to soft tissues (33). Lipid suppression is recommended when diffusion measurements are used to estimate temperature changes.

2.2.2 *PROTON DENSITY*

The temperature-dependence of the proton density (PD) stems from the fact that it depends linearly on the equilibrium magnetization, M_0, determined by the Boltzmann distribution where

$$PD \propto M_0 = \frac{N\gamma^2\hbar^2 I\left(I+1\right)B_0}{3\mu_0 kT} = \chi_0 B_0 \tag{2.4}$$

N is the number of spins, γ is the gyromagnetic ratio (42.58 MHz/T for hydrogen protons), $\hbar$ is Planck's constant, I is the quantum number of the spin system (1/2 for hydrogen protons), B_0 is the magnetic flux density, μ_0 is the permeability of free space, k is the Boltzmann constant, T is the temperature (in Kelvin), and χ_0 is the susceptibility. Note that χ_0 and T has an inverse relationship. This is known as the Curie law. Therefore, the change in susceptibility can be related to the temperature in PD-weighted images. Note that the PD does not change with temperature but the ratio of parallel and antiparallel spins, which will show as a change in susceptibility (33), is temperature dependent. The temperature sensitivity of PD is inversely proportional to temperature and ranges around -0.30 ± 0.01 %/°C from 37 to 80 °C (59). This is a relatively low temperature sensitivity that requires high SNR. To isolate effects from changes in T_1,

16

very long repetition times are needed, which yields lower spatiotemporal resolution (60). If lower TRs are needed, it may be difficult to isolate changes in PD with the relaxation times (61).

2.2.3 SPIN-LATTICE RELAXATION TIME (T_1)

The temperature-dependence of T_1 has been well known from NMR studies (62) and was one of the earliest parameters used for MRTI (63-67). Essentially, in tissues T_1 depends primarily on dipolar interactions during rotational and translational motion of molecules. This molecular motion is temperature-dependent thus T_1 can be a means to measure temperature. T_1 can be described by the following first-order Arrhenius rate process where

$$T_1(T) \propto e^{-E_a(T_1)/kT} \tag{2.5}$$

and $E_a(T_1)$ is the activation energy of the relaxation. It is known that T_1 and temperature dependence are tissue dependent. Generally, the temperature dependence of T_1 can be described as

$$T_1(T) = T_1(T_{ref}) + \alpha(T - T_{ref}) \tag{2.6}$$

where T_{ref} is a reference temperature and α is the temperature sensitivity (dT_1/dT). α has been measured in several tissues with difference values including 0.97 %/°C in adipose tissue (65) and 1-2 %/°C in soft tissue (63, 64, 66-68).

17

Although measuring T_1 requires a longer imaging time, the change in T_1 can be shown to be related to the change in signal from spin echo or gradient echo images. Generally, the signal, *S,* can be described as

$$S(T) \propto M_0(T)\sin\theta \frac{1-e^{-TR/T_1(T)}}{1-\cos\theta e^{-TR/T_1(T)}} \tag{2.7}$$

where θ is the flip angle. The signal decreases with increasing temperature due to increasing T_1 and decreasing M_0. By taking into account the small nonlinear temperature dependence of M_0, the change in *S* as a function of temperature can be described as

$$\frac{dS}{dT} = \alpha\frac{dS}{dT_1} - \frac{S}{T} \tag{2.8}$$

which takes into account both the decrease in M_0 and the increase in temperature or vice versa. Therefore, by neglecting the small T_2 (or T_2^* for gradient echo acquisitions) temperature dependence and weighting in T_1-W images, the change in signal in T_1-W images as a function of temperature can be described as

$$\frac{dS}{SdT} = -\frac{\alpha TR(1-\cos\theta)e^{-TR/T_1}}{T_1(T_{ref})^2\left(1-e^{-TR/T_1}\right)\left(1-\cos\theta e^{-TR/T_1}\right)} - \frac{1}{T_{ref}} \tag{2.9}$$

It is important to note that changes in tissue properties, such as coagulation, can cause changes in *S* which will affect temperature measurements (69).

2.2.4 Spin-Spin Relaxation Time (T_2)

As with T_1, there is an increase in T_2 relaxation time with increasing temperature. In observing the signal from a T_2-W image with increasing temperature, there can be a large sigmoidal decrease that can even remain during cooling of the tissue (70). This is an important characteristic of irreversible tissue damage which is useful to define the outcome of a thermal treatment. Therefore, although T_2 may not be good quantitative means to measure temperature changes, it often plays a role in treatment verification in high-temperature thermal ablations.

2.2.5 Magnetization Transfer (MT)

Generally, MT techniques use spectrally-selective RF pulse to saturate protons bound to macromolecules which are normally not visible in MR due to very short T_2 or T_2* values. During the RF pulse, the bound, saturated protons enter the primary pool of water protons or transfer the magnetization to the primary pool (71). These exchanges are temperature dependent. For example, MT-weighted signals were determined to be tissue dependent, with some tissues showing relatively no change in signal such as in adipose tissue and brain. In tissues where a change in signal was seen with temperature, effects on MT-W images were nonlinear with either increasing signal (muscle, heart, prostate, liver) or decreasing signal (blood) (72, 73). These variances in temperature sensitivities do not make MT a readily reliable method for MRTI.

2.2.6 PROTON RESONANT FREQUENCY (PRF) SHIFT

2.2.6.1 Physical Basis

Temperature sensitivity of the PRF was first reported by a group led by Pople in 1958 (35) and later by Hindman (34). The temperature dependence in the PRF arises from the hydrogen bonding between hydrogen protons and oxygen nuclei in water. In tissue, water is the most abundant compound that contains hydrogen protons. When temperature increases, the increased kinetic energy of the water protons result in a longer hydrogen bond with other water molecules and a shorter covalent bond between the hydrogen and parent oxygen atoms. This results in the proton lying in closer proximity to the oxygen's electron cloud, thereby changing the proton's chemical shift, σ (Figure 2-1). The PRF, f, can then be expressed as a function of the chemical shift where

$$f = \gamma B_0 \left(1 - \sigma\right) \tag{2.10}$$

γ is the gyromagnetic ratio (42.58 MHz/Tesla for hydrogen atoms) and B_0 is the applied magnetic flux density. The chemical shift, σ, theoretically is related to the electronic structure around the nucleus. Usually empirical approaches are used to describe the chemical shift since theoretical calculation requires extensive knowledge of the electron density in the ground and excited states of the molecule as well as the excitation energies. Generally, the chemical shift is the contribution of the electrons surrounding the nucleus as well as other surrounding molecules around the nucleus (74).

$$f = \gamma B_0 (1 - \sigma(T)) \qquad f = \gamma B_0 (1 - \sigma(T + \Delta T))$$
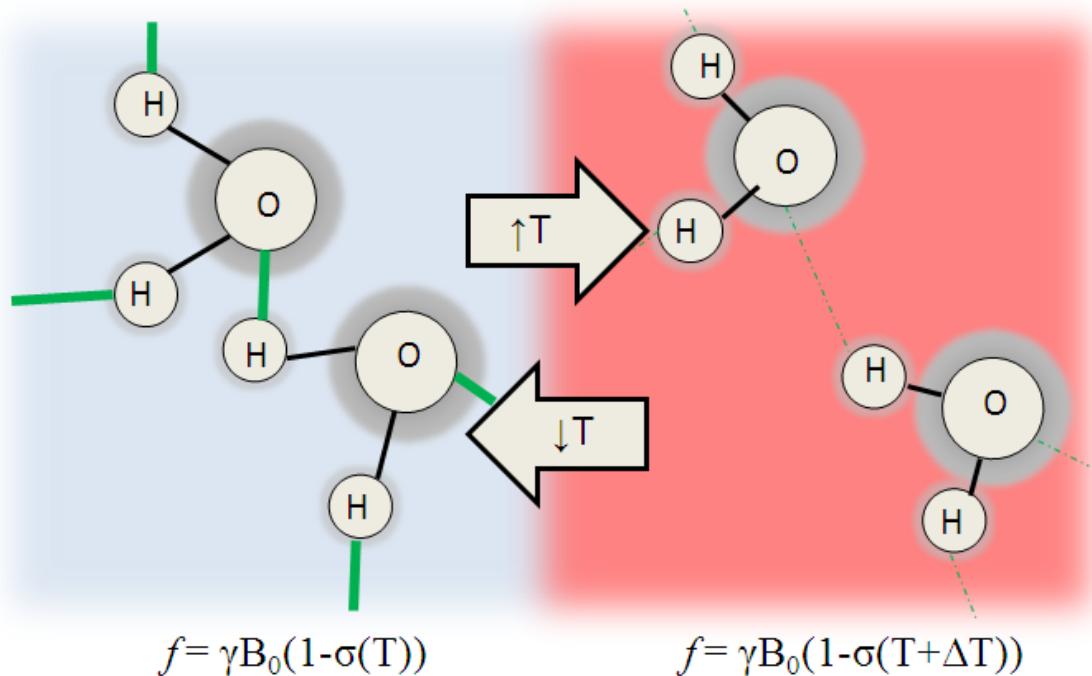
Figure 2-1 Illustration of temperature effects on the PRF

As temperature rises, the hydrogen bonds (green line) between hydrogen and neighboring oxygen atoms stretch, bend and break. This causes the hydrogen to move closer to its own oxygen's electron cloud making it better shielded and changing the chemical shift, σ.

2.2.6.2 Temperature Sensitivity of the PRF

Measuring the PRF shift as a function of temperature or measuring the distances between two spectral peaks to measure temperature has long been used in NMR in the field of analytical chemistry. When compared to other MRTI-based parameters, the temperature sensitivity coefficient of the water PRF is relatively the same for different tissues is close to pure water which has a temperature sensitivity coefficient (TSC) of

-0.010 ppm/ºC (34).   Many studies have been performed *in vivo* to measure the temperature sensitivity of the PRF. McDannold presented a thorough review of the TSC of the PRF using both CPD and CSI techniques. Most TSC values in several tissues have been found to be between -0.009 to -0.010 ppm/°C (75).   This corroborates what Hindman reported initially in pure water (TSC=-0.01 ppm/°C) (34).   However, some *in vivo* studies have measured values above and below this range. Peters et al. stated a possible reason for the discrepancies is due to the temperature-induced changes in the bulk magnetic susceptibility (76). This can also be affected by the orientation of the heat source in relation to the magnetic field. Electrical conductivity of tissues can also change the temperature dependence (77).

In fatty tissue, De Poorter et al. measured an overall TSC of -0.0097 ppm/℃ with a susceptibility constant of -0.0013 ppm/℃ giving a corrected field shift of -0.0088 ppm/℃ (43). In a separate study by a different investigator, when using lipid (bulk methylene) as an internal reference, the TSC of the difference was measured and found to be around -0.00852 ppm/℃ (37).   A study using a line scan echo-planar spectroscopic imaging (LSEPSI) technique on a mayonnaise and lemon juice phantom also found a similar TSC when using bulk methylene as an internal reference (45).

Ex vivo tissues have shown little change in sensitivity when compared to *in vivo* tissues (75, 78, 79). It is also important to note that the sensitivity does not change when tissues coagulate, which is in contrast to what is seen in T_1-based MRTI (37). This is crucial for safety at high-temperature ablations to be able to measure temperature after

22

damage has occurred to assure temperatures do not reach excessive levels to prevent charring of tissue.

There is also growing interest in trying to use CSI for absolute temperature estimations. Currently, MRTI methods are most often used to measure changes in temperature and not absolute temperature. Absolute temperature estimation is an established method in NMR experiments. For instance, in a sample tube, the shift between ethyl ($-CH_2-CH_3$) or methyl ($-CH_3$) protons to the hydroxyl ($-OH$) protons is commonly used in the NMR setting. For MR, the goal is to quantify water, lipid and/or metabolite peak locations and their relative differences between water between them to make absolute temperature measurements. There have been studies where N-acetylaspartate and water was used to measure temperature in the brain with low spatial and temporal resolution (80, 81). However, there are many factors that can affect the distribution of the metabolite, lipid and water chemical shifts including intravoxel temperature variations, pH, magnetic ion concentration, blood-oxygen level dependent (BOLD) effect, *J*-coupling effects and susceptibility (37). According to a recent review of MRTI, the "feasibility of absolute temperature imaging has not yet been established; further detailed investigations will be required for that" (37). This is a highly-desired diagnostic imaging capability to detect highly metabolic or inflamed lesions which can be at a higher temperature compared to the baseline temperature.

2.2.6.3 Complex Phase Difference Techniques for Measuring the PRF

A fast CPD method (38) has been the preferred method to estimate the PRF shift indirectly. To estimate the temperature change in a voxel, the difference between the current phase image, Φ, and the reference image, Φ_{ref}, can be related to the TSC described as

$$\Delta T = \frac{\Phi - \Phi_{ref}}{2\pi \cdot \alpha \cdot \gamma \cdot B_0 \cdot TE} \qquad (2.11)$$

where α is the TSC (ppm/°C) and TE is the echo-time (ms).

In CPD techniques with sufficient SNR (≥ 5), the uncertainty in the CPD image, $\sigma_{\Delta\phi}$, can be expressed as

$$\sigma_{\Delta\phi} \cong \frac{\sigma}{A}\sqrt{2} = \frac{\sqrt{2}}{SNR_A} \qquad (2.12)$$

where A is the magnitude signal, σ is the noise of the magnitude signal, which is assumed to be approximately Gaussian distributed, and SNR_A is the signal-to-noise ratio of the magnitude image (82). A contrast-to-noise ratio in the phase difference image, $CNR_{\Delta\phi}$, can then be defined by

$$CNR_{\Delta\varphi} \propto \Delta\varphi \cdot SNR_A \propto TE \cdot e^{-TE/T2^*} \cdot \sin(\theta) \cdot \frac{1 - e^{-TR/T1}}{1 - e^{-TR/T1} \cdot \cos(\theta)} \qquad (2.13)$$

assuming a spoiled gradient-echo acquisition. Note that this is essentially the product of the TE (which is proportional to $\Delta\varphi$) and the SNR. The dependence of TE on the phase

difference constrains the $CNR_{\Delta\phi}$ to be optimal at $TE=T_2^*$, which can be shown by differentiation of equation 2.13 (82).

A major advantage of the CPD technique for PRF-based thermometry is its high spatial and temporal resolution (~1.5x1.5x4 mm^3, $\leq$5 sec (39)). Typically, fast temperature imaging can be achieved with GRE acquisitions (38) or EPI (83). As stated above, the optimal TE for CNR in CPD is at the T_2^* of the tissue. As a result, standard GRE acquisitions have a relatively long TR which lowers spatial and temporal resolution. If higher resolutions are needed, echo shifts are applied with TR<TE at an expense of SNR (41). Alternatively, the use of EPI allows for longer TEs without sacrificing resolution or SNR. Techniques using balanced steady-state free-precession (bSSFP) have also been studied for PRF-based temperature mapping. This is accomplished by measuring a linear fit along several TEs acquired. However, the phase behavior was found to be highly nonlinear with this technique so simple phase to frequency mapping is not feasible (48).

Although CPD techniques are advantageous when high spatial and temporal resolution is required, there are several well-known limitations of this technique. Intravoxel lipid contamination (40, 41), inter- and intra-scan motion (42), tissue susceptibility changes (43) and static magnetic field drifts (44) all cause artifacts that are commonly encountered with CPD techniques.

It is important to remember that the PRF shift is a function of temperature due primarily to changes in the hydrogen bonds between water molecules. These hydrogen

bonds are absent for protons in lipid molecules, which are covalently bonded. Therefore, the temperature sensitivity of lipid tissue is a stronger function of the macroscopic susceptibility. The presence of lipid can alter the phase in CPD acquisitions which, in turn, can affect temperature estimates. Common practice to address this is to simply suppress the lipid signal (40, 41). Although lipid signal is suppressed, however, it does not correct susceptibility effects that lipid can have on the nearby water molecules. The effect of a mixed water and lipid environment cannot be handled completely with suppression because lipid is still physically present in the tissue and can have an effect on temperature estimation in the voxel via susceptibility effects.

As with most imaging techniques, intra-scan and inter-scan motion is another common issue that must be addressed with CPD approaches. Intra-scan motion is motion during the acquisition which results in view to view k-space errors seen as image blurring and ghosting. Imaging times can be decreased to reduce intra-scan motion but at an expense of SNR. Inter-scan motion is a more difficult problem to handle since images are subtracted to obtain temperature estimates. It is important to note that motion not only effects the spatial registration between scans but also the magnetic field which changes the phase leading to errors in temperature estimation (33). Multiple strategies have been developed in an effort to overcome artifacts from inter-scan motion. For respiratory motion, gating with mechanical respiration has been successful but this, of course, is invasive (84). Gating with free-breathing has been used but it is challenging when there is irregular breathing (85). The use of navigator echoes has also been studied

26

as well as referenceless thermometry which estimates the background phase in the treated area by fitting a polynomial extrapolated from unheated regions (86). These studies have had limited success but according to a recent review of MRTI, "motion is the most prevalent problem for temperature monitoring with PRF phase mapping (CPD) and the main reason that has impeded its acceptance for clinical applications in areas that are subject to motion" (33).

Macroscopic susceptibility changes in tissue can also affect the accuracy of temperature estimates with the CPD technique (43). Susceptibility does change with temperature, but when compared to the PRF as a function of temperature, this effect is four to five times smaller in magnitude. It has been approximated as being linear with 0.0026 ppm/°C for pure water and 0.0016 ppm/°C in muscle (43). It has been found though that the temperature dependence of the susceptibility is tissue-dependent (87) as well as the orientation and geometry of the heating source (76). One possible method to correct for susceptibility effects is to measure the PRF response to temperature in a chemical specimen that is not sensitive to temperature changes. Lipid is such a specimen. It is expected that lipid will experience susceptibility effects in the voxel. Therefore, using lipid, or any covalently-bonded proton, as an internal reference to correct for susceptibility is a possible means to improve temperature measurements (37).

Field drift is yet another effect that must be considered when the PRF is used for MRTI. Temporal drifts in the local magnetic field due to increased gradient duty cycles and eddy currents can change the PRF (88). Simple corrections are often possible by

27

using a reference phantom at a fixed temperature (44). More elaborate corrections are also possible using multiple reference phantoms to estimate the linear shifts across the image (89). A method that calculates the apparent diffusion coefficient (ADC) and PRF has also been proposed to correct for field drift (90). As with susceptibility, lipid or another internal covalently-bonded proton reference can be used to aid in correcting for field drifts (37).

2.2.6.4 Chemical Shift Imaging Techniques for Measuring the PRF

An alternative to the indirect CPD method is a direct method of measuring PRF shift via chemical shift imaging (CSI) techniques (45-48). CSI has several advantages over CPD techniques. One is that the water proton resonant frequency is measured separately from other resonances whereas CPD measures the mixture of frequency components in each voxel resulting in a variable response. This immediately relieves the problem of intravoxel lipid contamination seen in CPD. Also, the lipid signal can be used as an internal reference to account for field drifts, susceptibility and motion since it is relatively insensitive to temperature (37). Therefore, CSI would be particularly useful in areas with high lipid content, such as bone marrow, breast, and head and neck lesions (45). In addition, it may be useful in patients with fatty-liver for minimally-invasive treatments of liver lesions (91). It is also important to note that areas with little or no lipid can also benefit from CSI-based temperature imaging since directly measuring the water PRF can potentially result in higher sensitivity given appropriate SNR with adequate spectral analysis techniques (45, 53). Therefore, researchers have worked to

develop CSI techniques that increase the sensitivity and spatiotemporal resolution while maintaining the ability to reduce artifacts seen in CPD. However, as mentioned in the previous chapter, these studies have limitations for multiple reasons.

Magnetic resonance spectroscopic imaging (MRSI) was proposed for MRTI before the CPD technique was introduced (46). However, the acquisition time needed for the desired spectral resolution (with or without suppression) was deemed impracticable for MRTI. For example, MRSI measurements using a small 32 x 32 matrix with a spectral bandwidth of 10 ppm at 1.5T and a spectral resolution of 0.01 ppm (1 °C) required 26 minutes per acquisition.

One approach to overcoming some of the time limitations of the MRSI approach is to use echo planar spectroscopic imaging (EPSI) techniques. These techniques have been proposed for temperature monitoring and prior studies have demonstrated that temperature changes can successfully be monitored, lipid can be used as an internal reference when present, and artifacts due to motion can be reduced (47). Although this method was demonstrated to be considerably faster than conventional MRSI, initial EPSI acquisitions still required 3 minutes to acquire a low spatial resolution temperature image (5 x 5 mm^2) on a 3.0T system. This is because the technique used 4 interleaved shots of 16 echoes (5.2 ms echo-spacing, total of 64 echoes) to achieve an effective echo-spacing of 1.3 ms to avoid aliasing of the lipid signal due to a narrow spectral bandwidth. Data interleaving resulted in a spectral bandwidth of 769 Hz (12.04 ppm) with a spectral resolution of 12.0 Hz (0.188 ppm). In addition, spectra from the EPSI technique can be

degraded by instability in the magnetic field and motion during the phase-encoding process of the acquisition (37).

McDannold, et al. applied a line scan EPSI (LSEPSI) technique (92) to address limitations to previous CSI-based MRTI techniques (45, 93). LSEPSI is a combination of EPSI with a voxel-selective technique for column scanning (92). This method substantially improved the spatial and temporal resolution. Specifically, in an *in vivo* breast scan at 1.5T, a 32 x 32 cm^2 FOV was acquired in 4.2 seconds with a spatial resolution of 5 x 5 x 5 mm^3. However, this spatial resolution is still considered quite poor compared to CPD methods (39). Thirty two echoes where acquired with a high receiver bandwidth of ±64 kHz, which limited the SNR.

As stated in chapter 1, major contributors to the low spatiotemporal resolution in these studies include interleaved echo trains and high receiver bandwidths to decrease the echo-spacing to avoid aliasing of the lipid peak. In addition, high ETLs were used in Fourier-based approaches to calculate the PRF. The high ETL degrades the spatiotemporal resolution. In the next chapter, we present an approach that will allow spectral aliasing of lipid peaks to negate the need of interleaving echo trains and allow reduced bandwidths for higher SNR. To further aid in increasing spatiotemporal resolution and sensitivity, a model-based approach to calculate the PRF using undersampled data will be presented. The combination of these acquisition and post-processing techniques will be used to test our hypothesis.

Chapter 3: Theoretical Background for Dynamic Chemical Shift Imaging

3.1 Introduction

In this chapter, the theory and background of the acquisition strategy, spectral processing, and mapping are presented. First, gradient-echo imaging will be introduced along with details of the acquisition implementation for rapid CSI. Next, spectral processing of CSI data will be overviewed. In this context, the detailed theory of autoregressive moving average (ARMA) modeling will be presented. Finally, details will be outlined on how these spectral parameters, specifically the PRF for temperature imaging, are mapped to images using a k-means clustering algorithm.

3.2 Rapid CSI from a Multi-Gradient Echo Acquisition: From Theory to Implementation

Fundamentally, several conditions must be met in order to image the spatial distribution of hydrogen protons for MRTI. A strong magnetic field, B_0, is needed in order to align a small majority of protons with the field. Radiofrequency (RF) pulses at the resonance frequency, ω, are used to tip the spin population. As the population relaxes back to equilibrium with the magnetic field, a small voltage is measured in an RF-tuned receiver coil which is perpendicular to B_0.

In the laboratory frame of reference in the absence of gradients and relaxation effects, the signal from a 3D spin system, $\rho(x,y,z)$, in a given volume, V, can be described as

$$S(t) \propto \iiint_V \rho(x, y, z) e^{-i\omega(x,y,z)t} dV \tag{3.1}$$

To spatially localize the signal, gradients are used that spatially vary the magnetic field over the sample.

For an acquisition in the axial plane, the z-direction is assigned as the slice-selection direction. A gradient is applied in this direction in conjunction with the bandwidth-limited RF excitation pulse. This creates a planar distribution of spins described by

$$I(x, y, t) = \int_{z_0 - \Delta z/2}^{z_0 + \Delta z/2} \rho(x, y, z) e^{-i\omega(x,y,z)t} dz \tag{3.2}$$

where z_0 is the center of the slice and Δz is the slice thickness. The z-dependence in ω can be related to the magnetic field, B_0, and the slice encoding gradient, G_z, where

$$\omega_z = \gamma(B_0 + G_z z) \tag{3.3}$$

After the RF pulse, the spins in I can be localized spatially using gradients and encoded in k-space. The relationship between a location in k-space at time, t, and the gradients in the x and y directions is given by

$$k(t) = \gamma \int_0^t G(\tau) d\tau \tag{3.4}$$

In the collection of data in *k*-space, a phase encoding gradient moves collection of data to one line in *k*-space. This is followed by a frequency encoding gradient that is applied during the signal readout.

Mathematically, the signal at a location in *k*-space, $S(k_x,k_y)$ can be given by

$$S(k_x, k_y) \propto \iint \rho(x, y) e^{-ix2\pi k_x} e^{-iy2\pi k_y} \, dy \, dx \qquad \textbf{(3.5)}$$

It is important to note that this equation gives the spatial frequency domain of the spin distribution and a 2D Fourier transform can be used to represent the data in the spatial domain (74).

Figure 3-1 displays the pulse sequence diagram for a fast gradient echo acquisition typically used for standard CPD MRTI. A small flip angle RF pulse is used during encoding of the slice selection gradient, G_z. The polarity of G_z is then switched to account for de-phasing of the transverse magnetization. The frequency encoding gradient, G_x, is turned on to move across *k*-space. G_y is then applied for the phase encoding before the positive gradient of G_x encodes the signal. A G_z gradient is then applied to dephase residual transverse magnetization.
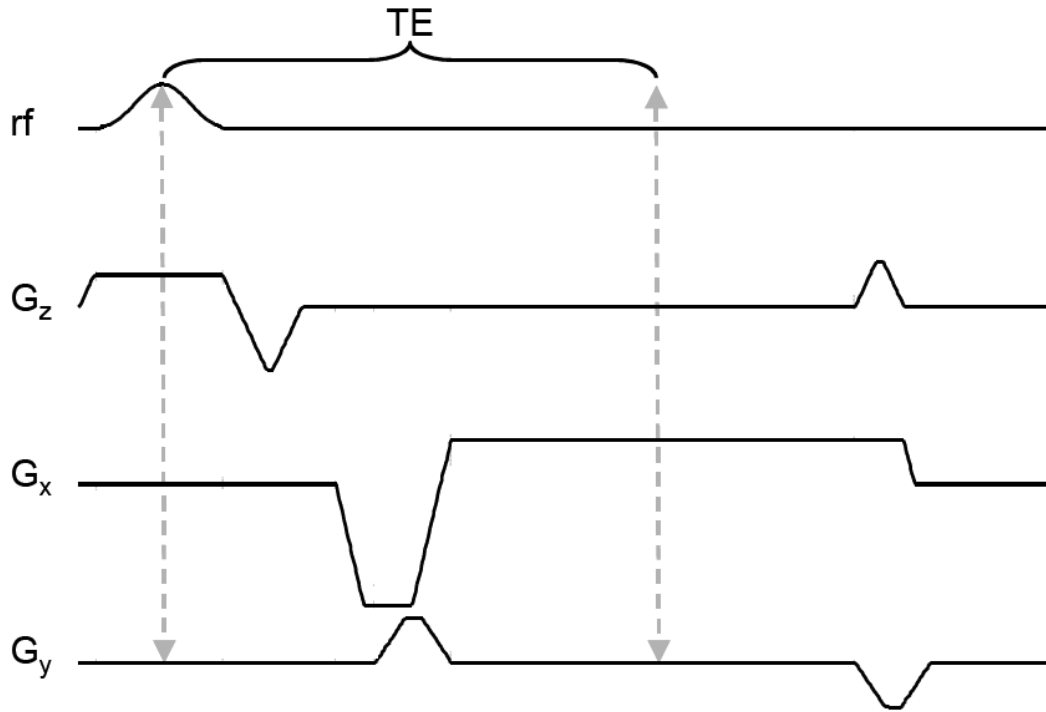
Figure 3-1 Pulse sequence diagram for a fast gradient-recalled echo (FGRE) acquisition

This represents a balanced pulse and gradient schematic for a high spatiotemporal CPD acquisition. Note that one echo is collected per TR.

In this research, the fast gradient-recalled echo (FGRE) acquisition was modified to provide multiple echoes per TR for encoding the chemical shift (Fig. 3-2). As with FGRE, the sequence is compatible with parallel acquisition techniques, such as SENSE, to increase the speed of acquisition (94) and can acquire images in interleaved slice acquisition mode or in a sequential slice acquisition mode with RF spoiling to cancel out any residual transverse magnetization before the next TR period by modulating the phase between successive RF pulses. Note that the TR is kept constant so there is no loss in

34

spatiotemporal resolution compared to CPD from a FGRE acquisition. The ETL and ESP are set in order to collect the selected number of echoes within the TR.
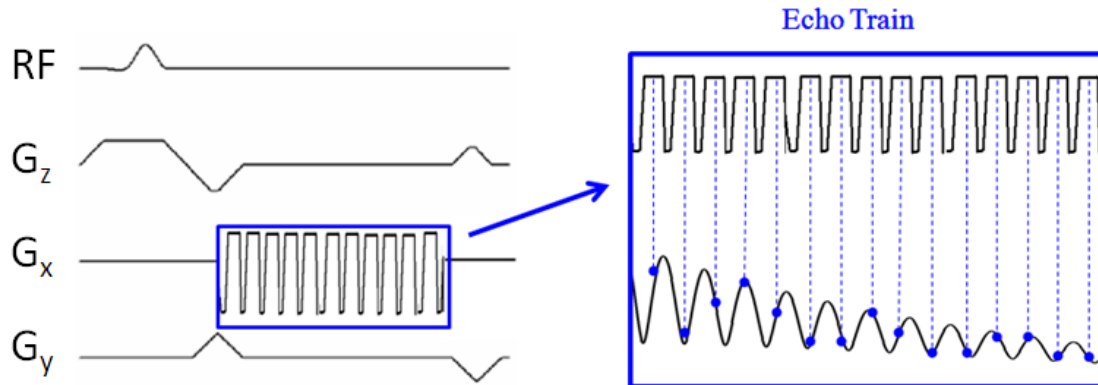
Figure 3-2 Pulse sequence diagram of a 2D unipolar MGE acquisition

The phase encoding gradient only pulses once per echo train. The frequency-encoding gradient can be implemented in bipolar or unipolar mode. In the unipolar sequence shown above, when each echo is acquired in a positive gradient readout, the free induction decay (FID) is sampled.

The sequence can be run using unipolar readout gradients with time-optimized rewinder (i.e. flyback) gradients as shown in Figure 3-2 or using bipolar readout gradients. In bipolar gradient mode, negative polarity readout data is time reversed in *k*-space prior to image reconstruction by Fourier transformation. Also in bipolar gradient mode, N/2 spectral ghosting caused by timing errors between the positive and negative readouts can be corrected by applying a calculated linear phase shift to the images reconstructed from every other echo time (95). The moments of the signal are calculated

in *k*-space. The phase shift is measured by the differences in the moment between odd and even echoes in the bipolar readout (Figue 3-3).
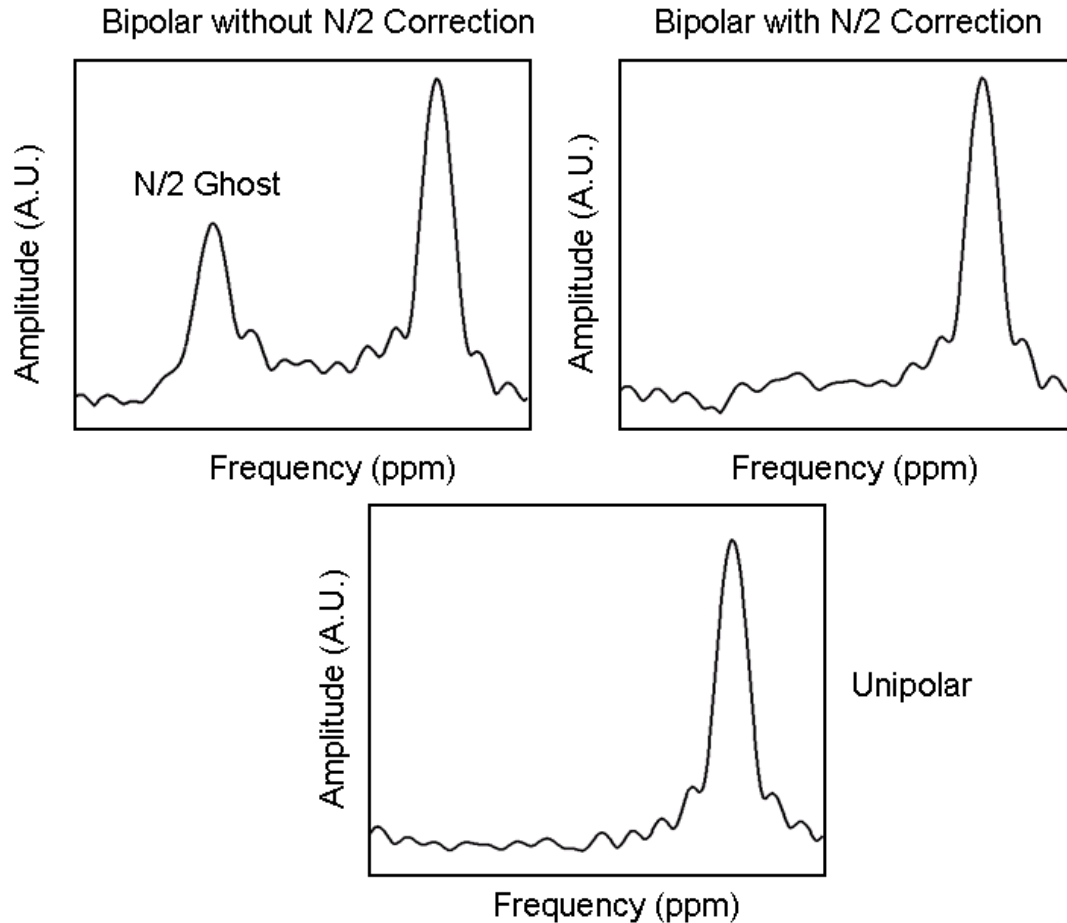
Figure 3-3 Differences between bipolar and unipolar readout gradients with N/2 correction

Bipolar and unipolar readout acquisitions were performed on an agar phantom. Due to timing errors between odd and even echoes, the bipolar readout gradient is susceptible to N/2 ghosts (top left). These timing errors can be corrected by calculating the phase change in *k*-space (top right). Unipolar readout gradients are immune to these errors but using unipolar gradients comes at an expense of larger ESP and lower SNR (96).

We made two fundamental changes in the conventional acquisition strategy for fast CSI acquisitions. First, the echo-spacing (ESP) parameter was increased in order to facilitate use of lower readout bandwidths to provide higher SNR. In the case of previous 3.0T CSI acquisitions, restraints on the ESP have usually resulted in the use of multiple interleaved echo-trains in order to avoid aliasing (47). Because of the relaxed ESP associated with this technique we can acquire multiple echoes within one TR acquisition thus increasing the spatial and temporal resolution compared to previous CSI acquisitions for MRTI. This causes aliasing of the lipid peak. However, in MRTI we are only interested in the change in the lipid PRF and not the absolute position when measuring temperature changes.

The second modification was to collect only the number of echoes that would fit into the TR period of our standard CPD MRTI sequence. The artifacts associated with this undersampling required innovative processing in order to resolve the lipid signal as outlined in the following section.

To increase sensitivity, uncertainties in the PRF as a function of acquisition parameters need to be determined. It is important to note that in PRF mapping, the frequency difference, which is directly proportional to temperature, is not constrained to TE=T_2*, in contrast to CPD. For an homogenous voxel,

$$\mathrm{CNR}_{\Delta f} \propto \Delta f \cdot SNR_A \propto e^{-TE/T2^*} \cdot \sin(\theta) \cdot \frac{1-e^{-TR/T1}}{1-e^{-TR/T1} \cdot \cos(\theta)} \qquad \textbf{(3.6)}$$

which means that the sensitivity of measuring frequency changes is directly proportional to the SNR of the source image from a gradient echo acquisition. This gives an image metric where the sensitivity of the frequency changes can be measured and verified using the spectral analysis technique as described in the next section.

3.3 Spectral Processing of CSI Data

In many 2D, high spectral resolution, low spatiotemporal resolution CSI techniques, several chemical shifts including water, lipid, and metabolites such as choline and N-acetyl aspartate (NAA) are mapped by adding a spectral dimension to the *k*-space data to encode chemical shifts. For example, EPI gradients allow signal readouts which encodes one spatial dimension and the spectral dimension at the same time. In 1983, Sir Peter Mansfield, Nobel Laureate in Medicine for the development of MR, proposed EPI for 2D CSI with a hybrid projection reconstruction method to bypass Fourier transforms, which were slower computationally at that time (97).

Several studies have been done to build on what was proposed by Mansfield. Initial implementations suffered from poor gradient performance and artifacts arose from the convolution of spectral and spatial information. Posse et al. improved this by improving the orthogonalization of the spectral and spatial information to reduce artifacts seen in 2D CSI (98). Rapid acquisition and relaxation enhancement (RARE) (92, 99, 100) and LSEPSI (101) have also been investigated to improve the spatial, temporal and spectral resolution for spectroscopic inquiry. Parallel imaging (102, 103) and compressed sensing (104, 105) techniques have also been implemented to improve the

38

spatiotemporal resolution of these otherwise low spatiotemporal, high spectral resolution CSI techniques.

There are several methods to quantify spectra in various domains, including the frequency domain, time domain and *z*-domain. Originally, MR signals were calculated using continuous wave (CW) spectroscopy. These spectra were recorded by scanning the frequency axis, which measured the intensity of the signal as a function of frequency (106). Currently, MR spectra are obtained in the time domain with post-processing typically by deconvolution of the resonance frequencies into the frequency domain via Fourier transformation. The time-domain acquisition reduces scan time and increases SNR compared to CW spectroscopy (107).

The Fourier transform (FT) is the most common method to measure MR spectra by transforming the MR signal from the time domain to the frequency domain. Generally, the transform can be represented as

$$F(\omega) = \int\limits_{-\infty}^{\infty} f(t)e^{-2\pi i \omega t} dt \qquad\qquad (3.7)$$

where ω is the frequency, *t* is time, and *f(t)* is the time-domain function. The FT is bijective and invertible meaning that the signal can be measured in one domain and transformed to another. Although the FT is commonly used, assumptions in Fourier analysis impose restrictions on the quality of the spectra. In a discrete signal, the FT can be represented as

$$A_n = \sum_{k=0}^{N-1} a_k e^{-\left(\frac{i2\pi nk}{N}\right)}$$

$$(3.8)$$

where A_n is the discrete representation of the spectra from the time domain signal a_k. As seen in this equation, the spectra is dependent on the number of samples N. The spectral resolution is inversely proportional to N (108). In rapid CSI for temperature imaging, N needs to be relatively small to maintain high spatial and temporal resolutions. By using the FT, this comes at a cost of degraded spectral resolution to measure changes in the PRF (Fig. 3-3). In addition, if the data in the time domain has non-zero values at the end of the acquisition, this causes apodization of the spectra, which can degrade peaks, especially secondary peaks such as lipid.

$$A_n = \sum_{k=0}^{N-1} a_k e^{-\left(\frac{i2\pi nk}{N}\right)}$$
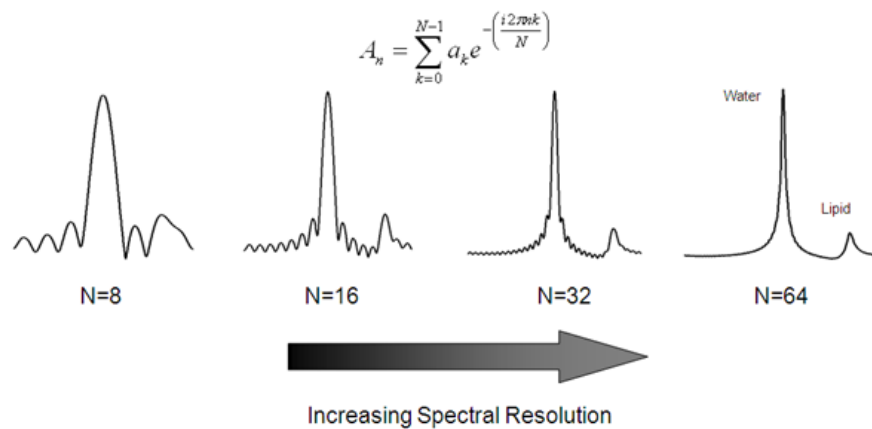
Figure 3-4 The effects of the number of samples on spectra using FFT

The spectral resolution is directly proportional to the number of samples in the signal. In this case, the lipid peak is more difficult to discern with a lower number of samples. Spectral resolution can be improved by collecting more samples. This typically comes at a tradeoff of decreasing spatiotemporal resolution.

It is important to note that the FT doesn't make assumptions in the model that describes the data (see equation 3.6). The only constraints on the signal is that the integral of $|f(t)|$ from -∞ to ∞ exists and that any discontinuities in *f(t)* are finite (108). Although this makes FT useful for a variety of applications, it has a disadvantage of not incorporating prior knowledge of the signal. In addition, the FT is assumed as a single sum, where in practice the signal has signal and noise components (50).

Several time-domain methods have been developed to analyze spectra. The main goal of these methods is to minimize the differences between the measured data and the signal model through a non-linear least squares problem. This depends on the particular algorithm being able to find a global minimum in the data and avoid errors from finding local minima. Generally, the risk of not finding the optimal solution using these methods

41

increases when initial conditions are away from what is acquired in the signal. This often requires heavy user interaction in order to manually obtain starting values for these algorithms (109). Interactive algorithms such as variable projection (VARPRO) (110) and the advanced method for accurate, robust and efficient spectral fitting (AMARES) (111) are common MR quantification tools. VARPRO uses the Levenberg-Marquadt (LM) algorithm (112), which was later replaced by AMARES when reviewers cited greater flexibility. Baseline errors can also be handled with time-domain methods with user interaction (109).

Visualization of spectra and fitting results are best shown in the frequency domain (113). Compared to time-domain methods, frequency-domain methods have fewer model parameters that need to be fitted. In this domain, methods can be separated as non-iterative and iterative methods. The most widely used quantitative method in this domain is frequency-selective area under the peaks. However, with this method it is difficult to discern overlapping peaks and high baseline signals. Additionally, low SNR can degrade the ability for quantification (113). Singular value decomposition (SVD) methods have also been developed, where only regions along a specific frequency are used for analysis, resulting in faster processing times (114). In iterative processes, non-linear least squares techniques via algorithms such as the LM algorithm (112) have been used. Specifically, with the LM algorithm deGraaf and Bovee used the algorithm to obtain *in vivo* proton spectra in the brain using prior knowledge of metabolites from *in vitro* metabolite solutions (115). In addition, mixed Lorrentzian-Gaussian (or Voight)

models were developed to fit the signal in the frequency domain. In both time and frequency domain, algorithms are shown to be computationally expensive and/or requires *a priori* knowledge of the spectra (116).

There are also "black-box" techniques where little interaction is needed from the user which makes it attractive for rapid temperature imaging (50). These methods use the *z*-transform where

$$\sum_{k=0}^{N} f(k)\delta(t-k) \overset{Z}{\leftrightarrow} \sum_{k=0}^{N} f(k)z^{-k} \tag{3.9}$$

and δ is the Kronecker delta function. Although these methods are commonly characterized as time-domain methods, it is important to note that analysis is performed in the *z*-domain where the frequency-domain is a subspace where $|Z\{f(t)\}| = 1$. Theoretically, in a MR signal containing water and lipid, *x(t)*, can be represented discretely as a sum of damped complex exponentials convoluted with a comb function, that is,

$$x(t) = \left[C_W e^{-\left(2\pi i f_W + 1/T2_W^*\right)t} + C_L e^{-\left(2\pi i f_L + 1/T2_L^*\right)t} \right] * \sum_{m=TE\min}^{n \cdot TE} \delta(t-m) \tag{3.10}$$

where $C_{W,L}$ is the complex amplitude for water (W) and lipid (L), respectfully, $f_{W,L}$ is PRF, $T2_{W,L}^*$ is the apparent spin-spin relaxation time, TE is the echo time and *n* is the number of echoes. By taking the z-transform, equation 3.10 can be represented as

$$X(z) = Z(x(t)) = \sum_{t=TE\min}^{n \cdot TE} C_W e^{-\left(2\pi i f_W + 1/T 2_W^*\right)t} z^{-t} + \sum_{t=TE\min}^{n \cdot TE} C_L e^{-\left(2\pi i f_L + 1/T 2_L^*\right)t} z^{-t}$$

$$\text{(3.11)}$$

Equation 3.11 can be rewritten as

$$X(z) = \sum_{t=TE\min}^{n \cdot TE} C_w \left(e^{-\left(2\pi i f_W + 1/T 2_W^*\right)} z^{-1} \right)^t + \sum_{t=TE\min}^{n \cdot TE} C_L \left(e^{-\left(2\pi i f_L + 1/T 2_L^*\right)} z^{-1} \right)^t \qquad \text{(3.12)}$$

Note that this can also be represented as a geometric series where

$$X(z) = \frac{C_W}{1 - e^{-\left(2\pi i f_W + 1/T 2_W^*\right)} z^{-1}} + \frac{C_L}{1 - e^{-\left(2\pi i f_L + 1/T 2_L^*\right)} z^{-1}} \qquad \text{(3.13)}$$

(49). Therefore, the poles of $X(z)$ can provide the frequency and T_2^* information for water and lipid. The complex amplitude of each exponential can be calculated using the residue evaluated at each pole (51, 52). In general, equation 3.13 in the presence of noise can be expressed as an autoregressive moving average (ARMA) process described as

$$H(z) = \frac{B(z)}{A(z)} = \frac{\sum_{n=0}^{N-1} \beta_n z^{-n}}{1 + \sum_{n=1}^{N} \alpha_n z^{-n}} \qquad \text{(3.14)}$$

Finding the coefficients, α_n and β_n, involves solving a set of overdetermined equations. One method to approximate the coefficients was proposed by Belkic using the Pade' approximant (PA) based on a technique originally developed by Henri Pade' (51, 117, 118). While the PA is able to process low TE signals and expand to non-Lorentzian spectra, it has limitations at low SNR. In addition, the PA demonstrates low performance

44

with a low number of poles and zeros, especially if it less than the number of samples (119).

Another analysis method is to use an iterative method which will potentially converge to a more accurate and precise solution compared to analytical methods (120). Thus, we propose a hybrid approach using Prony's method (120) and the iterative Steiglitz-McBride (SM) algorithm (121). Both algorithms are used in applications such as digital filter design and communications and a detailed treatment of both algorithms can be found in (120). The reasoning to use these algorithms include the minimal interaction required by the user (50), relatively rapid processing time compared to non-linear least squares methods (53), and performance in the presence of noise (121, 122). Here the algorithms will be explained to show how these can be used to calculate the coefficients and provide frequency, T_2* and amplitude content for water and lipid.

Equation 3.14 can be represented as

$$b(t) = h(t) * a(t) \tag{3.15}$$

since, as in Fourier theory, the convolution in the time-domain is a product in the z-domain. In matrix form, equation 3.15 is

$$
\begin{bmatrix} \beta_0 \\ \beta_1 \\ \beta_2 \\ \vdots \\ \beta_{N-1} \\ 0 \\ 0 \\ 0 \end{bmatrix} = \begin{bmatrix} x_0 & 0 & 0 & \cdots & 0 \\ x_1 & x_0 & 0 & & \\ x_2 & x_1 & x_0 & & \\ \vdots & \vdots & \vdots & & \vdots \\ x_{N-1} & & & & \\ \vdots & & & & \\ \vdots & & & & \\ x_K & & \cdots & & x_{K-N} \end{bmatrix} \begin{bmatrix} 1 \\ \alpha_1 \\ \alpha_2 \\ \vdots \\ \alpha_N \end{bmatrix}
\qquad (3.16)
$$

where N is number of chemical species and K is the number of echoes, and x_n are the samples in the time-domain. In Prony's method, $h(t)$ is partitioned and an error term, e, is added where

$$
\begin{bmatrix} \beta \\ e \end{bmatrix} = \begin{bmatrix} H_1 \\ H_2 \quad | \quad H_3 \end{bmatrix} \begin{bmatrix} 1 \\ \alpha^* \end{bmatrix}
\qquad (3.17)
$$

H_1 contains N-1 rows, H_2 is a column vector with K-N-1 terms, H_3 is the remaining (K-N-1) x N matrix and α^* is simply a column vector of the denominator coefficients. This separates the interdependence of α and β terms in order to find the solution. First, the α terms are found by taking the pseudo-inverse to minimize e, that is,

$$
\alpha^* = -\left(H_3^t H_3 \right)^{-1} \left(H_3^t H_2 \right) = -H_3^{\#} H_2
\qquad (3.18)
$$

where t is the transpose operator and # denotes the pseudo-inverse operation. Once α^* is calculated, β can be simply calculated by

$$
\beta = H_1 \alpha
\qquad (3.19)
$$

46

Unlike Prony's method, which works by minimizing the error in the overdetermined set of equations, the SM algorithm seeks to iteratively minimize the error between a model estimate (x_d) and the measured signal (x). The algorithm uses an initial estimate (from Prony's method) and quickly iterates to a solution. Briefly, the algorithm takes the first N columns of the matrix

$$H_{\alpha i} = H \cdot \alpha \qquad (3.20)$$

where H is the K x K-N+1 matrix as described in equation 3.16 and α is the initial estimate. This partitioned matrix is denoted as H'_{α}. Knowing that

$$x_d = x + e = H_{\alpha i} H \alpha_{i+1} = H'_{\alpha i} \beta + e \qquad (3.21)$$

As in equation 3.18 the error term, e, can be minimized where

$$\alpha_{i+1} = \left(H_{\alpha i} H \right)^{\#} H'_{\alpha i} \beta \qquad (3.22)$$

and

$$\beta = \left(H'_{\alpha} \right)^{\#} x_d \qquad (3.23)$$

Therefore, combining equations 3.22 and 3.23 gives

$$\alpha_{i+1} = \left(H_{\alpha i} H \right)^{\#} H'_{\alpha i} \left(H'_{\alpha i} \right)^{\#} x_d \qquad (3.24)$$

which provides an iterative solution. Once α is known, β can be calculated again by using equation 3.19.

Once coefficients, α and β, are known, the poles can be calculated as roots of the denominator in equation 3.14. If ρ_1 and ρ_2 denote the poles for water and lipid, respectively, then the PRF of water or lipid (in ppm) can be expressed as

$$f_{W,L} = -\frac{\text{Im}\left[\ln(\rho_{1,2})\right]}{2\pi \cdot \Delta t \cdot \gamma B_0} \tag{3.25}$$

where Δt is the time between echoes, γ is the gyromagnetic ratio and B_0 is the applied magnetic flux density. In addition, the T_2^* value of water or lipid can be expressed as

$$T_{2,W,L}^* = -\frac{\Delta t}{\text{Re}\left[\ln(\rho_{1,2})\right]} \tag{3.26}$$

Finally, the complex amplitude of water and lipid can be computed separately using where

$$C_{W,L} = \frac{B(\rho_{1,2})}{A'(\rho_{1,2})} \tag{3.27}$$

and

$$A'(z^{-1}) = \frac{dA(z^{-1})}{dz^{-1}} \tag{3.28}$$

3.4 CSI Mapping using the k-means Algorithm

An important area of research in MR currently is the mapping of MR-detectable nuclei with different chemical shifts. The techniques for accomplishing this range from mapping multiple metabolites which is commonly used in various sites including brain, prostate and breast (123) to several techniques that are used to separate lipid-based chemical shifts from images to avoid obscuring underlying pathologies. This is a multi-faceted problem that involves not only separation of chemical shifts spectrally but also accurately mapping these parameters into images. The accurate mapping of chemical shifts is necessary in MRTI so appropriate temperature sensitivity coefficients can be applied to measure temperature (i.e. water must correctly be identified in order to measure temperature changes and lipid must be indentified accurately to use as an internal reference).

Essentially clinical CSI data for metabolic inquiry are currently processed by 3D FFT with filtering and/or zero-filling of the k-space data or by spectral modeling. For example, one method used exponential line broadening, Fermi filtering in the spatial domains to reduce truncation, and water suppression through low-pass filtering of the spectra in the time-domain (98). In addition to the processing of the spectral data, special consideration is needed for mapping the chemical shifts spatially. For instance, corrections are needed for field inhomogeneities and gradient eddy currents. Typically, data with unsuppressed water signal is acquired in order to calculate the field map to

correct for field inhomogeneities. The water signal can also be used to scale the relative concentration of other chemical shifts.

In CSI techniques for lipid and water separation, acquisitions and mapping strategies are different since a limited number of chemical shifts are known *a priori.* The motivation to separate the chemical shifts in lipid-water imaging is that the low T_1 of lipid makes it bright on many clinical imaging protocols. This can hide underlying processes such as contrast-enhancement of tumors, edema, and inflammation. There is also interest in knowing the lipid content in organs such as liver as well as using lipid images to distinguish certain tumors such as lipomas. There are multiple techniques to either remove lipid from the images or create "water-only" or "lipid-only" images.

One of the first techniques introduced to remove lipid from images is a chemical shift selective (CHESS) acquisition (124). In these acquisitions, a saturation pulse is centered at the dominant lipid peak frequency and the pulse flips the lipid protons 90° into the transverse plane. The RF pulse is immediately followed by a crusher gradient to spoil the transverse magnetization of lipid. The imaging acquisition is then acquired leaving little time for lipid to recover longitudinal magnetization thus suppressing the lipid signal in the image. However, this technique is sensitive to inhomogeneities in the static magnetic field and in the RF pulse (B_1), which can either leave lipid unsuppressed or suppress water.

Another method is to selectively excite the water instead of suppressing the water peak. These methods can excite protons in a particular spatial or spectral region. The

50

basic mechanism for these methods is to use RF pulses at specific intervals where lipid magnetization is flipped onto the longitudinal axis while signal is collected from the flipped water protons. As in CHESS sequences, these acquisitions are sensitive to field inhomogeneities. The use of multiple pulses can also require longer TRs which will increase imaging time. Unlike CHESS, it is relatively insensitive to inhomogeneities in B_1 (125).

Short TI inversion recovery (STIR) (126) is yet another method to suppress lipid to visualize underlying pathologies. This method takes advantage that non-enhancing tissue containing water has a longer T_1 than lipid. An inversion pulse is implemented followed by a time interval (TI) allowing the lipid magnetization to relax to the transverse plane. Then an imaging acquisition is implemented, albeit with lower water SNR. An advantage is that it is insensitive to field inhomogeneities and therefore it can be used in large or off-centered FOV situations.

Instead of selectively suppressing or exciting chemical shifts, there is a class of techniques based on the phase behavior between water and lipid. An early approach to phase-sensitive lipid-water separation was developed by Dixon (127) and thereby the techniques are commonly termed "Dixon Methods." By assuming a constant PRF difference between water and lipid, Dixon proposed that collecting images at two specific TEs can create images where lipid and water are in-phase and out-of-phase. By adding or subtracting these images, "water-only" or "lipid-only" images could be created. This is called a "two-point Dixon method." However, this method is sensitive to B_0

51

inhomogeneities. To address this, Glover (128) modified Dixon's method to obtain three echoes at specific TEs where the phase shifts between lipid and water were 0, π, and $-\pi$. By using phase-unwrapping algorithms, field inhomogeneities can be removed. Both methods, by Dixon and Glover, are insensitive to B_1 inhomogeneities and can be used in a variety of sequences including fast spin echo (FSE), GRE, and steady-state free precession (SSFP) (129).

Several methods have also been developed to improve on these early Dixon methods. It was noted that three-echo Dixon techniques were redundant and that methods are available to acquire field mapping with two echoes (130, 131). It was also shown that lipid suppression is possible with one echo at variable TEs (132). One method by Xiang used a region-growing algorithm instead of phase-unwrapping in conjunction with an asymmetric TE acquisition with an analytical solution for water and amplitudes (133). In addition, Ma et al. introduced a FSE method with phase-sensitive partial Fourier reconstruction in addition to a rapid two-point FSE acquisition using interleaved images (134). Ma also created a phase correction, region-growing algorithm that relies on the spatial gradient of the phase (135). In this algorithm, the direction of the phase is calculated by the magnitude and phase of surrounding voxels. Recently, Dixon methods were used in conjunction with diffusion-weighted imaging for whole-body detection of cancer metastasis (136). Iterative decomposition of water and lipid with echo asymmetry and least squares estimation (IDEAL) is another phase-sensitive lipid-water separation technique that uses a least-squares approach of the multi-echo data

to calculate the amplitudes of water and lipid (137). By assuming equivalency of the water and lipid T_2^*, T_2^* estimates have been made with IDEAL (138). In addition, multiple peaks of lipid have been mapped given the *a priori* information of the PRFs and amplitudes via calibration (139).

In each of these CSI techniques, certain assumptions are made in order to constrain the model to approximate a certain parameter. For example, the chemical shift between water and lipid in these methods are assumed to be relatively constant. In the presence of temperature changes, this is not the case. This assumption is made in order to accurately approximate another parameter which is most often the relative magnitude of each chemical shift.

As shown above, the PRF, T_2^* and amplitude of multiple peaks are calculated without making assumptions such as a constant PRF shift between water and lipid or equivalent T_2^* in water and lipid. Here we present a *k*-means clustering algorithm to identify these peaks and reconstruct these parameters into images with water-only and lipid-only field maps, T_2^* maps and T_1-W imaging. *K*-means clustering and other clustering algorithms such as the fuzzy *c*-means algorithm are powerful techniques that have been used to segment MR data typically from standard imaging techniques such as apparent diffusion coefficient (ADC), T_1, T_2, and PD-weighted images as well as functional MR data (140-143). In this work, we investigate how this algorithm can take the multi-parametric data to segment and map different chemical shifts such as lipid and water without relying on assumptions made in many CSI techniques. With proper

53

mapping, temperature changes can be accurately measured along with providing multi-parametric visualization of the spectral data.

The *k*-means algorithm is an automated and computationally rapid clustering algorithm that was first proposed by Lloyd in 1957 although he did not publish his work until 1982 (144). The term "*k*-means" was first coined by MacQueen in 1967 (145). It has a variety of applications in machine learning and statistics to partition data based on defined variables.

Given a set of measurements $(x_1, x_2, …, x_n)$ where each measurement is a *D*-dimensional real vector, the *k*-means algorithm partitions the *n* observations into *k* clusters given that *k<n* by minimizing an objective function, *S*, where

$$S = \sum_{j=1}^{k} \sum_{i=1}^{n} \left\| x_i - c_j \right\|^2 \qquad\qquad \textbf{(3.29)}$$

and $\left\| x_i - c_j \right\|$ is the Euclidean distance between data point, x_i, and it's cluster centroid, c_j.

First, random *k* clusters are assigned to all *n* observations and centroids are calculated for each cluster. Data points are then assigned to the nearest centroid. Every data point assigned to a certain centroid is assigned to the same cluster. Then, new centroids are calculated from the new clusters. This process continues iteratively until the centroid calculation converges for each centroid such that $c_j = c_{j-1}$. Figure 3-4 shows graphically in two dimensions the functions of the algorithm. All spectral processing and mapping was implemented using MATLAB (MathWorks, Natick, MA).

54
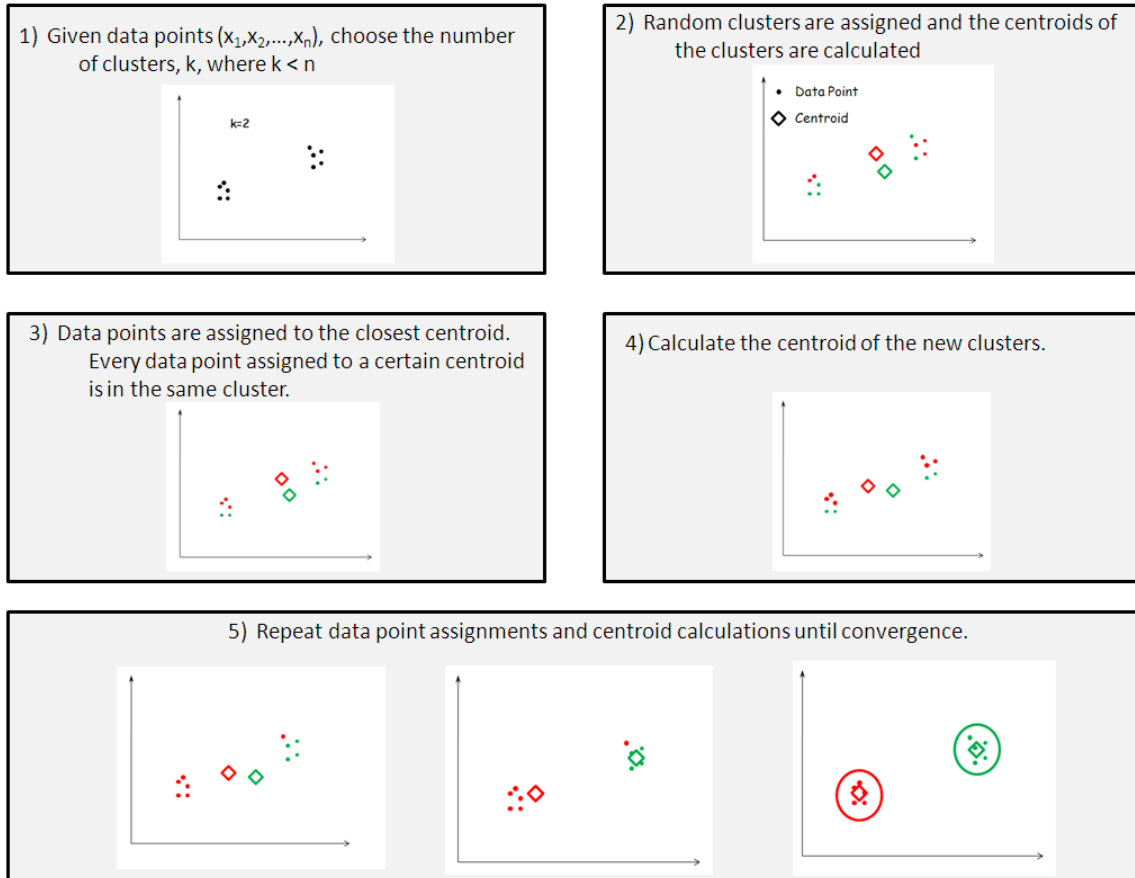
Figure 3-5 Schematic of the K-means algorithm

The algorithm assigns random clusters from the observations and centroids are calculated for each k cluster. Observations are then assigned to the nearest centroid. Then, new centroids are calculated from the new clusters. This process continues iteratively until the centroid calculation converges by for each centroid.

Chapter 4: Spectral Parameter Estimation and Acquisition Parameter Analysis from a Rapid Multi-Gradient Echo Acquisition

4.1 Introduction

This chapter thoroughly reports the results on the spectral processing and acquisition parameters that are needed for accurate and precise temperature imaging. First, spectral processing via a filtered Fourier method will be tested, which will outline limitations in Fourier-based techniques for measuring spectra with a low number of samples. Next, results from experiments testing the ARMA model as described in section 3.3 will be presented (specific aim 1). The measurements from the ARMA model will be used to find suitable acquisition parameters for accurate and precise temperature imaging (specific aim 2). At the end of this chapter, there is a discussion to place these results in context for temperature imaging.

4.2 Spectral Analysis using Fourier Windowing

4.2.1 MATERIALS AND METHODS

We investigated the assumption that, with careful selection of spectral filters, a windowed FFT technique could possibly provide accurate water and aliased lipid peak locations. A simulated signal containing water and lipid at physiologically relevant frequencies was generated. The amplitude of the lipid component was set to be one-tenth the amplitude of water. For temperature monitoring using lipid, it was assumed that the optimal location of the aliased lipid peak would be equidistant from the resonant water peak and its N/2 spectral ghost to minimize contamination of the lipid peak from water

sidelobes. The relation between the echo-spacing and the frequency difference between water and lipid was analytically determined.

In addition, we used the Lorentz-Gauss transform which increases spectral SNR and resolution by combining a Gaussian window and a positive exponential filter (146). The Gaussian window, *g(n),* is defined as

$$g(n) = e^{-\frac{1}{2}\left(\frac{n-1-N/2}{\sigma N/2}\right)^2} \tag{4.1}$$

where N is the total number of samples and σ is the ratio of the length between the two points of inflection on the Gaussian to the length of the entire window. To find a suitable σ for this window, the frequencies and amplitudes of the lipid and water peaks as well as the sidelobes were measured at different σ values. The optimal setting would be a standard deviation that produces the lowest error in water and lipid frequency estimation in simulation.

To increase spectral SNR for the FFT approach, a positive exponential filter, $\exp(n/T_2^*)$, was used where the apparent spin-spin relaxation (T_2^*) can be quickly estimated. Using simulation, the frequencies and magnitudes of the peaks were recorded with and without this filter using the T_2^* of water-only, lipid-only and a calculated T_2^* of the signal.

The product of both windows and the signal was zero-filled and Fourier transformed to create the simulated spectrum. The location of the maximum value of

each peak was calculated along with a moment calculation around each peak. These values were compared to a Gaussian fit of the peaks as done by McDannold et al (45) and also to frequency estimates from the Steightliz-McBride (SM) algorithm which is described in the following section. The time to calculate each spectrum using the windowed Fourier method as well as the SM algorithm and Gaussian fitting of the peaks were also recorded.

4.2.2 RESULTS

The relative distance of the lipid peak from the water peak and the N/2 ghosts at physiologically relevant frequency differences were simulated to help determine the best echo-spacing (ESP) for the acquisition prior to obtaining experimental data. By assuming that the lipid peak needs to be equidistant from the water and N/2 peaks at different frequencies, the optimal *ESP* was determined to be:

$$ESP = \frac{3}{4\delta_{w-l}\gamma B_0} \tag{4.2}$$

where δ_{w-l} is the frequency difference of the water and aliased lipid peak (in ppm), γ is the gyromagnetic ratio of hydrogen protons (42.58 MHz/T), and B_0 is the static magnetic field strength (in Tesla).

Simulations also demonstrated that the windowed Fourier spectral analysis using the Gaussian window would be able to suppress spectral sidelobes while maintaining water and lipid signal. The lipid peak with a physiologically relevant magnitude (10% of

water) becomes more pronounced than the water sidelobes at a standard deviation of 0.73 and the sidelobe to lipid ratio continues to decrease below this value. The uncertainties in δ_{w-l} from 3.3-3.7 ppm decrease as σ approaches 0.4 then the uncertainties increase as σ increases. Therefore, $\sigma = 0.4$ was used in the experiments involving the windowed Fourier method.

Effects of the exponential window in simulation are shown in Table 4-1. The lowest relative lipid and water peak magnitudes are seen when the T_2^* of lipid is used for the window. However, the uncertainty in δ_{w-l} was smallest (0.00144 ppm) when this value was used. No matter which of the three T_2^* values were used, the exponential window decreased the uncertainty in δ_{w-l}.

Table 4-1 Effects of the exponential window on CSI spectra (53)

	Relative Lipid Magnitude	Relative Water Magnitude	Lipid/Water Magnitude Ratio	Error in $\delta_{\text{W-L}}$ (ppm)
No Window	0.181	0.154	0.225	0.00554
Water T2*	0.404	0.373	0.207	0.00159
Lipid T2*	1.000	1.000	0.191	0.00144
Calculated T2*	0.248	0.218	0.217	0.00198

The effects of the exponential window at different T_2^* values at a frequency difference between lipid and water of 3.5 ppm. If the lipid T_2^* can be determined, it introduces the largest signal as well as the lowest error in frequency estimation using a fast moment calculation.

Table 4-2 shows the uncertainty of δ_{w-l} using a moment calculation with various values of spectral zero-filling, using the maximum value of each peak in a 1024-point spectrum, the SM algorithm's calculation, and in the Gaussian fits. The error shown is the root-mean-squared error over a simulated δ_{w-l} of 3.3-3.8 ppm. The time to calculate

one spectrum was also recorded to reflect the relative speed of each technique, which is variable depending on the processing speed of the computer system being used. The SM algorithm produced the lowest uncertainty of δ_{w-l}, with only a small increase in processing time relative to Fourier-based processing. This time also was less than the time required for fitting a Gaussian to each spectrum. The moment calculation demonstrated the trade-off between accuracy and processing time. In the experiments with short acquisition times, a moment calculation using 1024 points was used in the windowed Fourier calculations since only a small improvement in resolution (0.7×10^{-4} ppm) was seen with a greater processing time (1.5 ms/spectrum) at 2048 points. Processing was on a 4Gflop CPU processor.

Table 4-2 Processing computing performance in simulation (53)

Processing Method	Uncertainty in δ_{W-L} (10^{-4}ppm)	Processing Time (msec/voxel)
Moment		
512	23.0	10.8
1024	20.1	11.1
2048	19.4	12.6
Peak Maximum	23.6	10.6
Steiglitz-McBride	0.02	16.6
Gaussian Fit	15.8	59.2

The uncertainty for various processing methods with processing times in msec/voxel in these calculations. The processing times are to demonstrate the relative speed of each method. In this study, images were masked where only voxels with high signal relative to noise are processed.
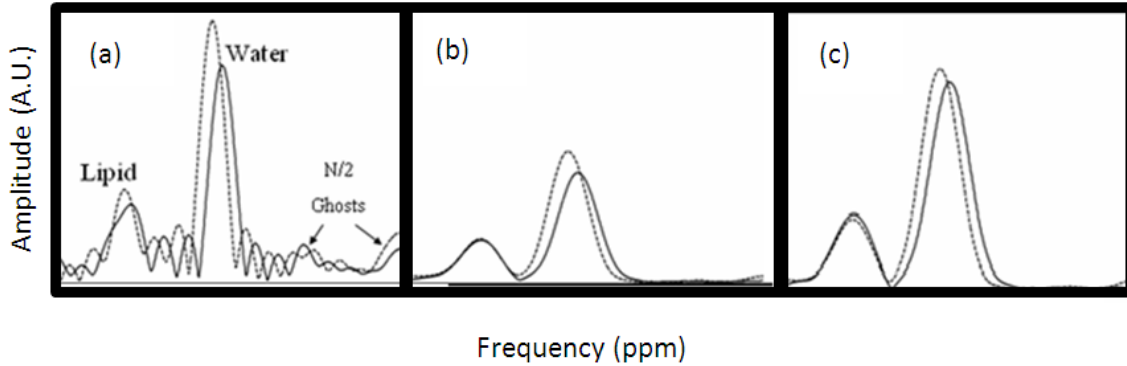
Figure 4-1 The effects of the Lorentz-Gauss transform on MFGRE-CSI spectra

(a) Unfiltered FFT in the phantom calibration ROI at 23.5 °C (dashed line) and 37.8 °C (solid line) with the presence of N/2 ghosts and sidelobes. (b) FFT spectrum with N/2 correction and Gaussian window ($\sigma=0.4$) applied resulting in minimization of sidelobes and N/2 ghosts with a mean reduction of peak magnitude of 50.5%. (c) FFT spectrum with the same N/2 correction and Gaussian window with an addition to the exponential window ($e^{TE/30.9ms}$) which increases both lipid and water peak magnitudes to 84.8% of the unfiltered peak magnitudes. Reprinted with permission from the American Association of Physicists in Medicine, (53).

4.3 Frequency, T_2* and Amplitude Estimation with ARMA Modeling

4.3.1 MATERIALS AND METHODS

The SM algorithm was tested, using Prony's method as an initial estimate, on simulated signals for one- and two-peak systems. In the one-peak system, acquisition parameters included spin lattice relaxation time (T_1), which was set at 500 ms, and T_2*=60 ms. The TR was fixed at 70 ms to maintain consistent temporal resolution. The minimum TE was set to 2 ms, with an echo-spacing of 3.3 ms. The two-peak system added a lipid signal that had 25% of the amplitude of the water peak. For the lipid peak, T_1=300 ms and T_2*=30 ms (74). A flip angle of 37° (the Ernst angle for lipid signal (74) was used. All other parameters were the same as those in the one-peak system. To

61

simulate noise in both systems, Gaussian noise was added to real and imaginary channels of the complex time domain signal. The SNR was defined as the amplitude of each spectral component divided by the standard deviation of the magnitude noise. Using ten samples at SNR=2 and ETL=4, the standard deviation of the water PRF was 0.6174 ppm. If we want 95% confidence that the mean is off by at most 0.01 ppm, then the number of samples needed is

$$n = \left(\frac{t_{9,\alpha/2}\sigma}{e} \right)^2 = \left(\frac{2.262 \cdot 0.6174}{0.01} \right)^2 = 19504 \qquad \textbf{(4.3)}$$

Therefore, to obtain the measurement uncertainty, we performed 20,000 random trials at each SNR value (147). Accuracies and uncertainties of the spectral parameters (chemical shift, T_2* and complex amplitude) were calculated using the SM algorithm for an ETL of up to 16 echoes to determine, as a function of SNR, how the number of acquired echoes at a fixed ESP affected the accuracy and precision of the measured spectral parameters.

The Cramer-Rao lower bound (CRLB) was used to provide a comparative theoretical basis of the uncertainty independent of the spectral processing technique. This was used to test the performance of the algorithm in terms of precision. The CRLB is defined as the minimum achievable variance for an estimator (148, 149). The CRLB for this model (the sum of complex damped exponentials) has been analytically defined in a one peak system and can be numerically determined for a multi-peak system as described by Kumaresan and Tufts (54). Detailed background and theory on the CRLB can be found in appendix A.

If an MR signal with only one peak is present, then the minimum uncertainty in the PRF, given by the CRLB, can be defined as

$$\sigma_{f,CRLB} = \frac{1}{2\pi \cdot SNR_A} \sqrt{\frac{p_0}{p_0 p_2 - p_1^2}} \qquad (4.4)$$

where

$$p_j = \sum_{k=0}^{N-1} (ESP \cdot k)^j \cdot e^{-2 \cdot ESP \cdot k / T_2^*} \qquad (4.5)$$

and SNR_A is the SNR of the first echo (54).

The uncertainties of the amplitudes, chemical shifts, and T_2^* values using the SM algorithm were compared to the CRLBs to ascertain the precision of the algorithm in the presence of noise. Correlation coefficients between simulation values and the CRLBs were calculated for each parameter in both the one- and two-peak systems.

The effects of ESP and T_2^* were simulated in the one-peak system with ETL=16. The uncertainty values for the chemical shift, T_2^*, and amplitude from 20,000 measurements were determined as a function of ESP and T_2^* and represented on surface maps.

We also performed simulations to measure the sensitivity of detecting secondary peaks in noise. In these simulations, the signal parameters were the same as those in a two peak system with an ETL=16, but the amplitude of water was changed to correspond to SNR for water of 10-50. Measurements of sensitivity were made at different

secondary peak SNR levels to determine at which SNR the secondary signal could be detected. This enabled the effects from water SNR, lipid SNR, and lipid/water ratios to be analyzed.

4.3.2 RESULTS

Precision of the SM algorithm on simulated data demonstrated a high correlation between the uncertainties in chemical shift and amplitude and the CRLB values for SNR$\geq$5 and ETL$\geq$4. When uncertainties approached the CRLB, the algorithm performed near optimum at the theoretical lower bound of the uncertainty for the given model. Figure 4-2 displays the uncertainties in the signal-peak model using the SM algorithm for the chemical shift, T_2^*, and amplitude estimates as a function on of SNR for ETL of 4-16 echoes. Solid lines represent the CRLBs for each simulation. As expected, he uncertainty of the estimates decreased as the SNR and number of echoes increased. T_2^* measurements generally showed lower correlation (slightly higher uncertainty than the CRLBs), primarily at lower SNR values, than other spectral parameters. This effect was expectedly exacerbated when using truncated ETLs (<8) which yield a reduced TE_{max}. For example, the uncertainty of measured T_2^* from simulations began to exceed the CRLBs at SNR<10 for ETL=8 and SNR<30 for ETL=4 (Figure 4-2). Table 4-3 shows the correlation coefficients between the simulated data and the CRLBs. In agreement with Figure 4-2, the chemical shift and amplitude showed very high correlation coefficients (Pearson's R^2>0.9990), with the correlation of the T_2^* measurements between simulation and the CRLBs decreasing as the number of echoes decreased.

64
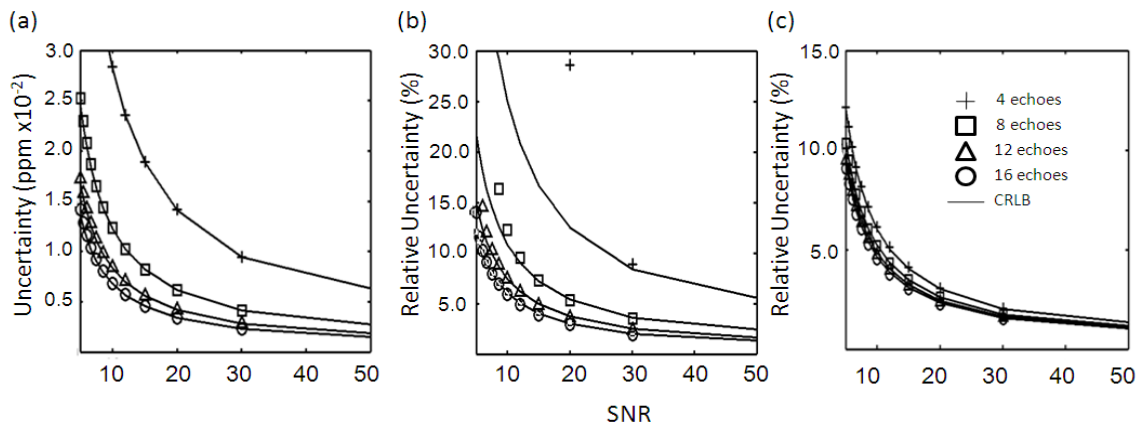
Figure 4-2 Single-peak simulation and CRLB results

Simulation and CRLB results for 4 (crosses), 8 (squares), 12 (triangles), and 16 (circles) echoes. This simulation used 20,000 trials. Estimates for chemical shift achieved an uncertainty at the CRLB for SNR≥5 for each ETL (4–16 echoes) (a). The uncertainties in T_2^* for ETL=16 achieved the CRLB for all SNRs >5 (b). As the ETL decreases, the uncertainty diverges from the CRLB. For instance, at ETL=8, the uncertainty is higher than the CRLB at SNR<10.Compared with the chemical shift (a) and T_2^* (b), the uncertainties of the amplitudes in the simulation and their CRLBs are less dependent on the number of echoes (c). Reprinted with permission from the American Association of Physicists in Medicine, (150).

Table 4-3 Correlation coefficients between simulation and the CRLB in an one-peak signal

Number of Echoes	Chemical Shift	T2*	Amplitude
4	0.9997	0.7919	0.9996
8	0.9997	0.8886	0.9998
12	0.9996	0.9944	0.9999
16	0.9994	0.9996	0.9999

Correlation coefficients between simulation and the CRLB in a water-only signal over multiple echo-train lengths. The uncertainties in chemical shift and amplitude have a very high correlation with the CRLB, as does the uncertainty in T_2^* at ETL=16. However, correlation between the uncertainties in T_2^* and the CRLB decreases as the number of echoes decreases. Reprinted with permission from the American Association of Physicists in Medicine, (150).

65

The measured uncertainty of the chemical shift and T_2^* estimates demonstrated an inverse proportionality to the ETL, as expected from the derivation of the CRLBs (54). For SNR = 20, the dependence of the chemical shift and T_2^* on the number of echoes had a relationship of $N^{1.01}$ (Pearson's R^2 = 0.990) and $N^{1.02}$ (Pearson's R^2 = 0.980), respectfully, where N is the number of echoes. The amplitude estimates exhibited less dependence on the number of echoes with a $N^{0.22}$ relationship (Pearson's R^2 = 0.982).

Simulations also showed agreement between the spectral parameter uncertainties and the CRLBs in a two peak model representing water and lipid. Figure 4-3 is a plot of the uncertainties and corresponding CRLBs for a simulated two-peak model of water and lipid for ETL=16. Corresponding correlation coefficients are shown in Table 4-4. Uncertainties in the chemical shifts of both water and lipid signals approached the CRLBs and maintained high correlation coefficients. As observed in the one-peak simulation of water, T_2^* values diverged more from the CRLBs than did other spectral parameters. Uncertainties in the lipid chemical shift and T_2^* values were demonstrably higher, even for the same SNR. Uncertainty in the amplitudes showed little difference between water and lipid. This result was consistent in a range of water and lipid concentrations. Further, as seen in the one-peak model, the uncertainty of each peak's spectral parameters increased as the number of echoes decreased.
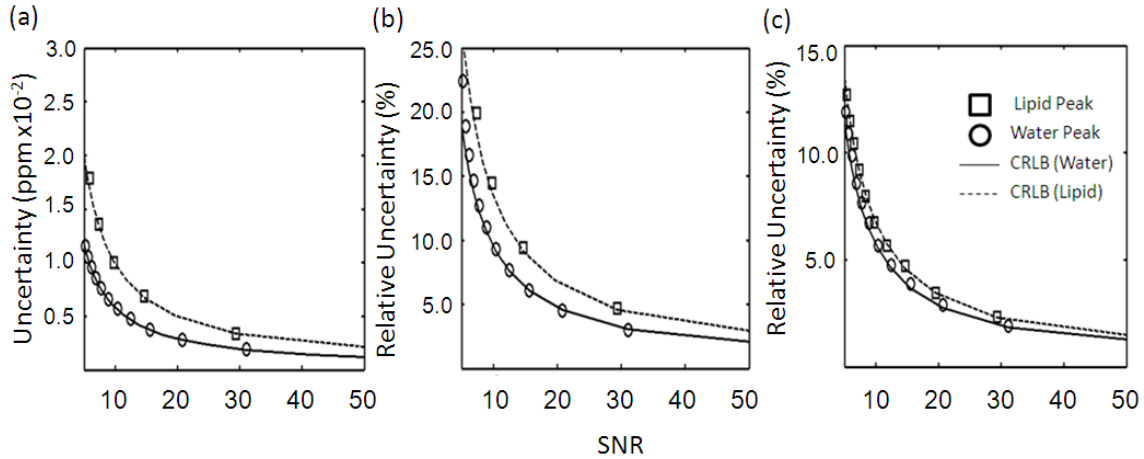
Figure 4-3 Simulation and CRLB results for a two-peak signal of water and lipid

This simulation used 20,000 trials. Estimates for the chemical shift of both water and lipid achieved an uncertainty at the CRLB (a). The uncertainties in T_2* for both peaks reached their CRLBs. The T_2* of lipid (30 ms) was set to half of that of water (60 ms) (b). The CRLB for the amplitudes of both water and lipid were similar when represented as relative uncertainties (c). The uncertainties provided by the algorithm had a similar result. Reprinted with permission from the American Association of Physicists in Medicine, (150).

Table 4-4 Correlation coefficients between simulation and the CRLB in a two-peak signal

Number of Echoes	Water			Fat		
	PRF	T2*	Amplitude	PRF	T2*	Amplitude
4	0.9753	0.5813	0.9997	0.9530	0.4811	0.9968
8	0.9758	0.6667	0.9999	0.9566	0.5495	0.9984
12	0.9810	0.7294	0.9999	0.9721	0.6811	0.9994
16	0.9886	0.9638	0.9999	0.9551	0.8435	0.9999

Correlation coefficients between simulation and the CRLB in a lipid-water signal over multiple echo-train lengths. As with the one-peak (water only) signal, the uncertainties in chemical shift and amplitude have a high correlation with the CRLB for both water and lipid. The uncertainties in T_2* correlate less with the CRLB as the number of echoes decreases. Reprinted with permission from the American Association of Physicists in Medicine, (150).

Surface maps illustrated the impact of T_2^* and ESP on a one-peak model with ETL=16 (Figure 4-4). Generally, the uncertainties were lower as T_2^* increased and the ESP decreased. Areas below the black line in Figure 4-4 (a-c) indicate areas where the TE of the last echo (TE_{max}) was larger than the simulated T_2^*. As expected, if collected echoes had TE values greater than the value of T_2^*, then the uncertainty of that estimate increased.
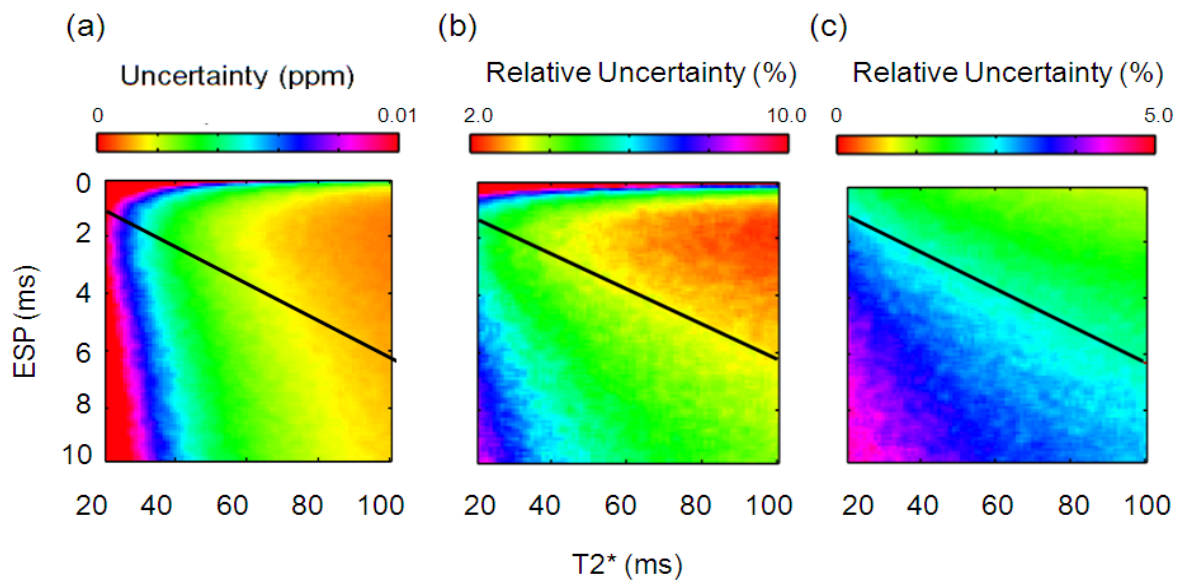
Figure 4-4 ESP and T_2^* effects on the uncertainty

Surface maps demonstrate the effects ESP and T_2^* (for a single-peak signal at SNR=20) have on the uncertainties for chemical shift (a), T_2^* (b), and amplitude (c). Areas below the black line represent where the ETL $TE_{max}>T_2^*$. This causes an increase in uncertainty, which is more evident on (b) and (c). ESP>1.0 ms can provide low uncertainties as long as the ESP is short enough not to sample above the T_2^* of the tissue. Reprinted with permission from the American Association of Physicists in Medicine, (150).

In addition to precision, we also used simulations to test the accuracy of the SM algorithm. Table 4-5 summarizes the measured accuracy of the estimates provided by the SM algorithm in a simulated water signal at SNR=20. These estimates are presented as the root-mean squared error (RMSE). The algorithm maintains high accuracy for the chemical shifts (<0.01 ppm) and amplitudes (<1.0%) for an ETL of 4-16. This was consistent down to SNR=5. T_2* values also maintained high accuracy but increased to $\geq$1% (0.6 ms) for ETL$\leq$5 at SNR=20. For each parameter, the accuracy decreased with decreasing ETL and SNR, as expected. Accuracies in the two-peak signals for the lipid-water simulation are summarized in Table 4-6. The RMSE values were higher for the water parameters in the lipid-water signal than those for the parameters of water in the water-only signal. However, accuracy was high for both chemical shift and amplitude, $\leq$0.01 ppm and $\leq$1%, respectfully, for ETLs of 4-16. At ETL$\leq$6, the RMSE of T_2* was $\geq$ 6% for the longer T_2* peak (water). As expected, T_2* measurements required a larger ETL to lower the bias when the ESP was fixed.

The sensitivity of second peak detection in noise was also investigated using simulations. Using lipid as a model for the second peak, it was observed that the sensitivity of locating the secondary peak depended on the relative SNR between the peaks as well as the individual SNR of each peak. In a model with a simulated water signal and SNRs of 10-50, the simulated lipid peak was consistently detectable down to an SNR of 2.64 ± 0.48 for lipid/water amplitude ratios of $\geq$0.05.

Table 4-5 Parameter accuracies in a water signal at a SNR of 20

Number of Echoes	Water PRF (ppm)	Water T2* (% Error)	Water Amplitude (% Error)
4	0.000185	5.65	0.0402
5	0.000136	1.03	0.0402
6	0.000105	0.493	0.0382
7	0.0000844	0.246	0.0364
8	0.0000724	0.194	0.0347
12	0.0000429	0.107	0.0301
16	0.0000316	0.0760	0.0282

Accuracies (root-mean squared error) determined through simulation of 20,000 independent trials with a water signal at a SNR of 20. High accuracy is achieved for the chemical shifts and amplitudes from four to sixteen echoes. T_2* values also has high accuracy but increases to > 1% (0.6 ms) at $\leq$5 echoes. Reprinted with permission from the American Association of Physicists in Medicine, (150).

Table 4-6 Parameter accuracies in a water/lipid signal at a SNR of 20

Number of Echoes	Water PRF (ppm)	Water T2* (% Error)	Water Amplitude (% Error)	Lipid PRF (ppm)	Lipid T2* (% Error)	Lipid Amplitude (% Error)
4	0.0083	42.1	0.425	0.0077	16.6	0.932
5	0.0067	38.4	0.322	0.0066	0.426	0.785
6	0.0047	6.52	0.227	0.0047	0.347	0.478
7	0.0027	0.474	0.136	0.0027	0.302	0.281
8	0.0021	0.225	0.106	0.0021	0.263	0.219
12	0.00047	0.113	0.0395	0.00048	0.166	0.0887
16	0.00018	0.0802	0.0293	0.00021	0.131	0.00715

Accuracies (root-mean squared error) determined through simulation of 20,000 independent trials with a water/lipid signal at a water SNR of 20. The accuracy of chemical shift is within 0.01 ppm and that of amplitude is within 1% RMSE for ETLs of 4–16. At ETL$\leq$6, the RMSE for both T_2* values is high, especially for the longer T_2* peak (water). Reprinted with permission from the American Association of Physicists in Medicine, (150).

4.4   Analysis of Acquisition Parameters

4.4.1   FLIP ANGLE
4.4.1.1 Materials and Methods

It is expected that for a homogenous voxel, the lowest $\sigma_{\Delta f}$ should occur at the Ernst

angle defined by

$$\theta = \cos^{-1}\left(e^{-TR/T1}\right) \qquad\qquad \textbf{(4.6)}$$

since SNR$_A$ is highest at this angle in a gradient echo acquisition. To validate this, an agarose phantom (1.5 % w/v) was made with distilled, de-ionized water to minimize variation in the metal ion content of the water, which can lower relaxation times and affect SNR measurements. Another phantom (agarose 1.5 % w/v) was made with 90% lemon juice and 10% mayonnaise to create homogenous lipid-water spectra throughout the phantom. A plastic vial of vegetable oil was also scanned on the 1.5T clinical scanner. The phantoms were stored in the MR scanner room overnight so their temperature would be equalized to that of the room. The T_1 and T_2* values were estimated in a 3 x 3 voxel ROI in each phantom. An MGE acquisition was performed (ETL=16 echoes; minimum TE (TE$_0$)=2.0 ms; ESP=3.3 ms; TR=69 ms; rBW=244 Hz/pixel; acquisition matrix=128x128; voxel volume=1.6x1.6x4.0 mm^3; 5 sec/image; parallel imaging acceleration factor=2). The flip angle was varied from 5° to 90° in 5° increments. Assuming a one-peak model for the pure water and lipid phantoms, frequency maps were made and $\sigma_{\Delta f}$ as well as SNR$_A$ were measured in the same ROI where the T_1 and T_2* measurements were made. The SNR$_A$ measures as a function of flip angle were compared to theory using the T_1 and T_2* measurements in both water and oil phantoms (SNR of a spoiled gradient echo acquisition, SNR$_A$). In addition, the uncertainty in ppm was plotted against 1/SNR$_A$. The slopes were compared where 1/SNR$_A$ is the variable and the slope is the proportionality which is a product of all the constants in the equations 4.4 and 4.5. In the SNR$_A$ and uncertainty plots, measurements

71

and theory were compared using a Student's t-test assuming equal variances (F-test verified). A two-peak model was used in the lipid-water phantom with separate field maps created for water and lipid and $\sigma_{\Delta f}$ of each field map was measured. For each phantom, the uncertainty of the T_2* and amplitude maps were measured as well.

4.4.1.2 Results

Figure 4-5 displays the uncertainties in the PRF (ppm), T_2* (ms), and amplitude (CoV) as a function of flip angle in the pure water agarose phantom. The Ernst angle was calculated to be $31.8 \pm 0.3°$ ($T_1 = 409.5$ ms) in the ROI where the uncertainty measurements were made. Generally, as SNR_A increased, the uncertainty of each spectral parameter decreases, as expected. Figure 4-6 contains the measurements from the vegetable oil, which had a measured Ernst angle of $74.2 \pm 0.4°$ (T_1=52.2 ms).

Figure 4-5 Flip angle dependence on uncertainty and SNR_A measurements in an agarose phantom

Uncertainties in the PRF (ppm), T_2^* (ms), and amplitude (CoV) were measured as a function of the flip angle. SNR_A was also measured at flip angles between 5 - 90° at 5° increments. Generally as SNR_A increased, the uncertainty in each parameter decreased. The Ernst angle was measured as $31.8 \pm 0.3°$.

Figure 4-6 Flip angle dependence on uncertainty and SNR$_A$ measurements in a vegetable oil

Uncertainties in the PRF (ppm), T_2* (ms), and amplitude (CoV) were measured as a function of the flip angle. SNR$_A$ was also measured at flip angles between 5 - 90° at 5° increments. As with the agarose phantom, as SNR$_A$ increased, the uncertainty in each parameter decreased. The Ernst angle was measured as $74.2 \pm 0.4°$, which is expectedly higher than what was measured in the agarose phantom due to a shorter T_1 (52.2 ms).

Figure 4-7 displays the SNR of water and oil as a function of flip angle in addition to the SNR dependence in the uncertainty. Using the calculated T_1s and T_2*s (409.5 ms and 63.4 ms for water, 52.2 ms and 25.4 ms for oil), the calculated SNR matched the measured values ($p=0.14$ and $p=0.43$ for water and oil, respectively). The bottom plots measures the uncertainty in ppm as a function of 1/SNR which is shown in equation 4.23.

74

Using ESP=3.3 ms, ETL=16, and measured T_2*, the constant from equation 4.4 was compared to the slope of the measured data. Again, there were no statistical differences showing that the uncertainty follows what is predicted by CRLB analysis (p=0.24 and p=0.09 for water and oil, respectively).
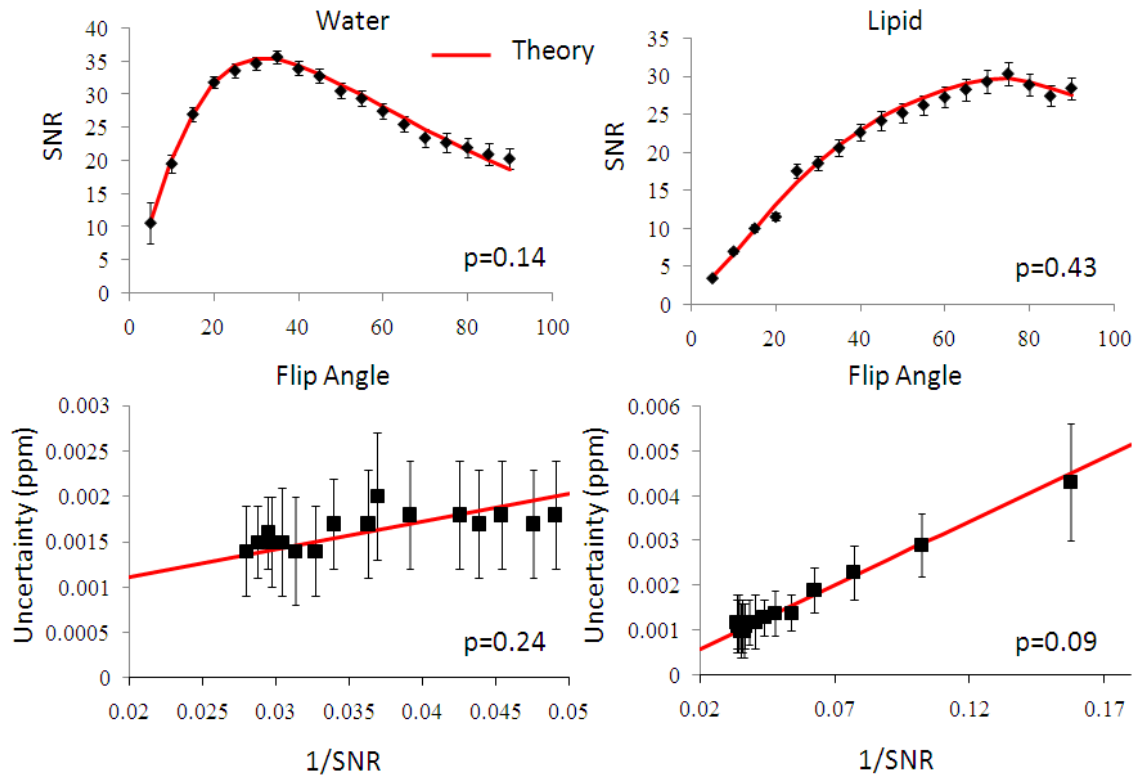
Figure 4-7 SNR and uncertainty measurements in phantom with comparison to CRLB theory

Top: Using the calculated T_1 and T_2* values, the calculated SNR matched the measured values (p=0.14 and p=0.43 for water and oil, respectively). Bottom: The bottom plots measures the uncertainty in ppm as a function of 1/SNR which is shown in equation 4.4. Using controlled acquisition parameters and T_2* measurements, there were no differences between the measurements and CRLB analysis.

Figure 4-8 displays the parameter uncertainties in the lipid-water (mayonnaise-lemon juice) phantom. At flip angles of 30° and above, the uncertainties of each parameter stayed relatively constant.
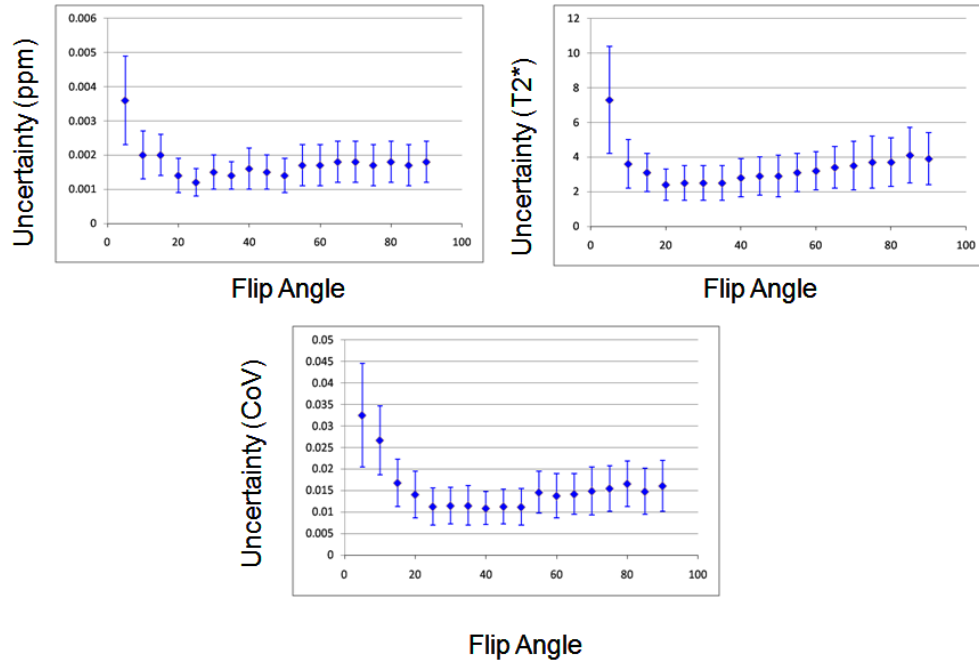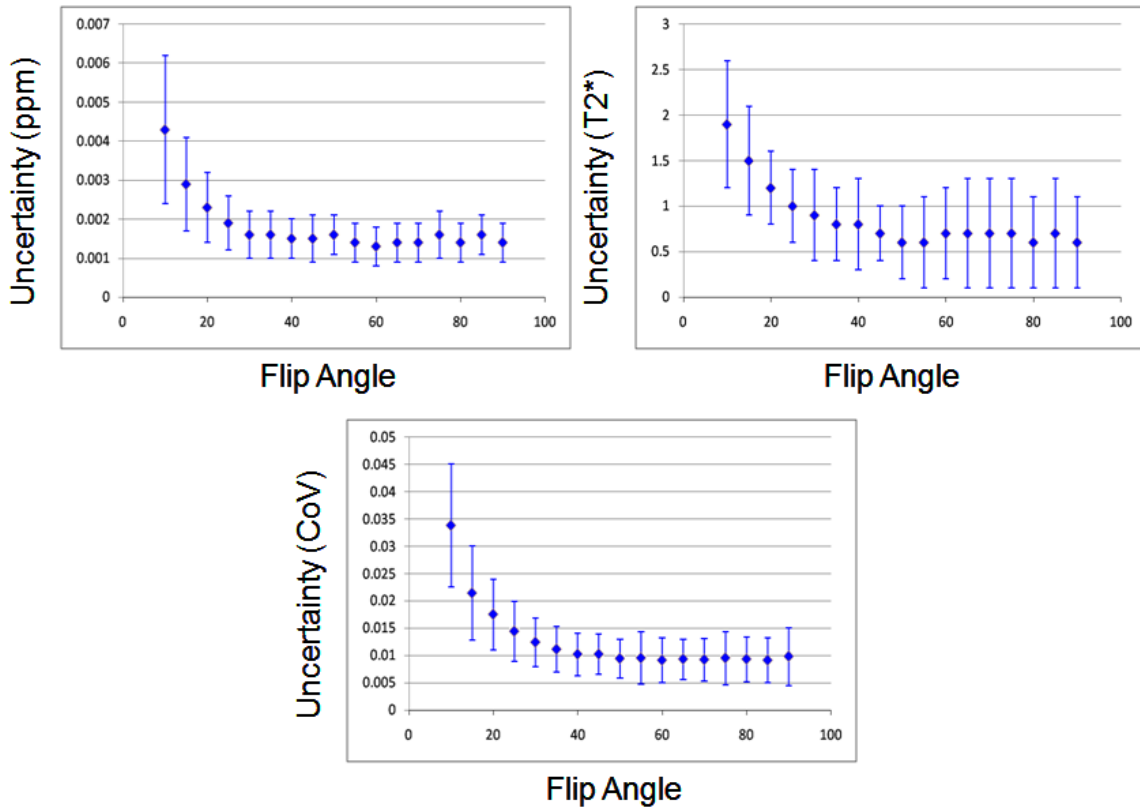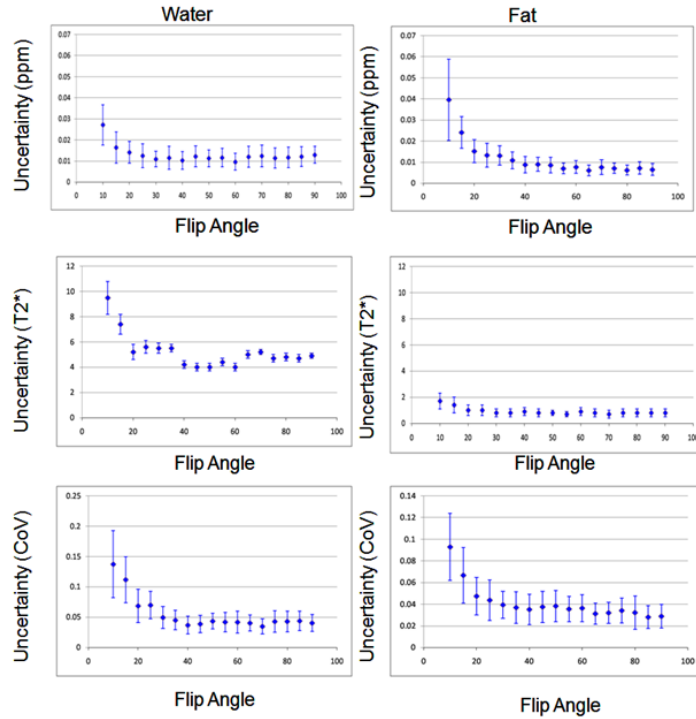

Figure 4-8 Flip angle dependence on uncertainty and SNR$_A$ measurements in a lipid-water phantom

Uncertainties in the PRF (ppm), T_2^* (ms), and amplitude (CoV) were measured as a function of the flip angle. Generally, uncertainties were lowest at higher flip angles. This data suggests that higher flip angles are needed when lipid and water are both present in the voxel.

4.4.2 ECHO-SPACING

4.4.2.1 Materials and Methods

In the Fourier approach, large spectral leakage, manifested as sidelobes, made the echo spacing become confined to a small range so peaks do not overlap. The ARMA modeling approach may allow more flexibility in the echo spacing allowing even lower bandwidths and, therefore, higher SNR. Experiments were performed to determine the ESP that reduces the uncertainty without peak overlapping. To test this, the lipid-water phantom (1.5% w/v) was scanned on a 1.5T clinical scanner with the echo-spacing varying from 3.3 to 4.3 ms (ETL=16 echoes; minimum TE (TE_0)=2.0 ms; TR=69 ms; FA=30°; rBW=244 Hz/pixel; acquisition matrix=128x128; voxel volume=1.6x1.6x4.0 mm^3; 5 sec/image; parallel imaging acceleration factor=2) at room temperature. $\sigma_{\Delta f}$ values of water and lipid were recorded as a function of ESP in a 3x3 ROI. Data analysis determined the low values of $\sigma_{\Delta f}$ in both water and lipid while discerning ESP values to avoid due to peak overlapping.

Simulations were also performed to ascertain the effects of SNR on the precision when the peaks are close together due to increasing ESP. Using the same simulation protocol as in the SM algorithm simulation study, the ESP was varied from 3.4 to 4.2 ms as a function of SNR. The uncertainties in the water and lipid PRF were determined.

4.4.2.2 Results

The uncertainties in temperature (using -0.0097 ppm/°C for water and -0.0088 ppm/°C for the difference PRF) are shown at various ESP values (Figure 4-9). The

uncertainties remain under 1.0 °C for water and 2.0 °C for when lipid is used as a reference at ESP of 3.3 to 3.8 ms. At 3.9 ms and above, uncertainties increase largely due to the inability to precisely ascertain the lipid peak. Note that the uncertainty in the water peak does not go above 1.0 °C except at 4.0 ms where the value is 2.1 °C. At 4.1 ms, the uncertainty in the water peak PRF goes to 0.9 °C although the lipid PRF uncertainty is relatively high at 7.5 °C.

Figure 4-10 shows the uncertainties in the T_2* and amplitude for each peak. As with the PRF, the peak overlaps affect the secondary peak (in this case lipid) more compared to the dominant peak (in this case water).
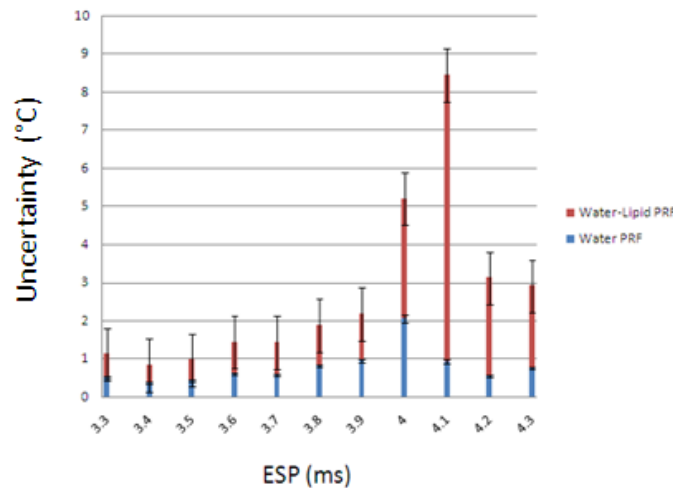
Figure 4-9 Influence of ESP on the precision of temperature estimates

Uncertainties in temperature are shown as a function of ESP. The water PRF relatively maintains precision indicating that the dominant peak can still be detected precisely even when peaks overlap. The precision of the secondary peak, which is lipid in this case, loses precision. From this plot, the uncertainty of the lipid PRF becomes quite high when the ESP is 3.9 to 4.3 ms. Error bars represent the standard deviation of the measurements.
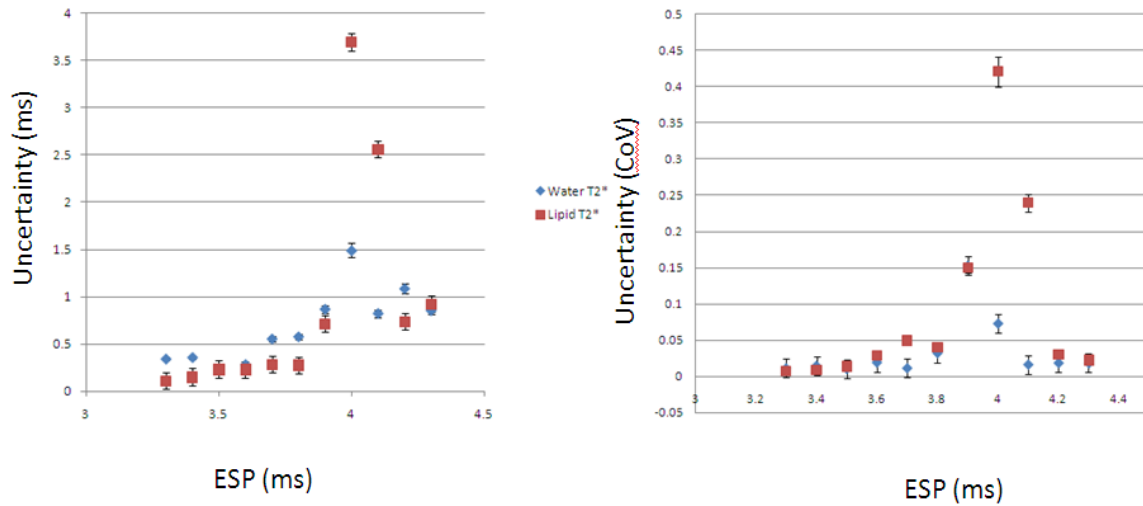
Figure 4-10 Influence of ESP on the precision of T$_2$* and amplitude estimates

Uncertainties in T$_2$* (left) and amplitude (right) are shown as a function of ESP. As with temperature, the water relatively maintains precision. The precision of the secondary peak, lipid, loses precision. From these plots, the uncertainty of the lipid parameters becomes high when the ESP is 3.9 to 4.3 ms and, thus, should be avoided if precise lipid estimation is needed in areas where water is dominant (such as the liver). Error bars represent the standard deviation of the measurements.

Figure 4-11 shows the influence of the ESP and SNR on the PRF uncertainty. As SNR increases, the ability to ascertain the water and lipid PRF increases even if the peaks are close together. Therefore, if two peaks are close together due to the actual physical properties of the signal or an ESP where lipid aliases over water, higher SNR can distinguish the two peaks.
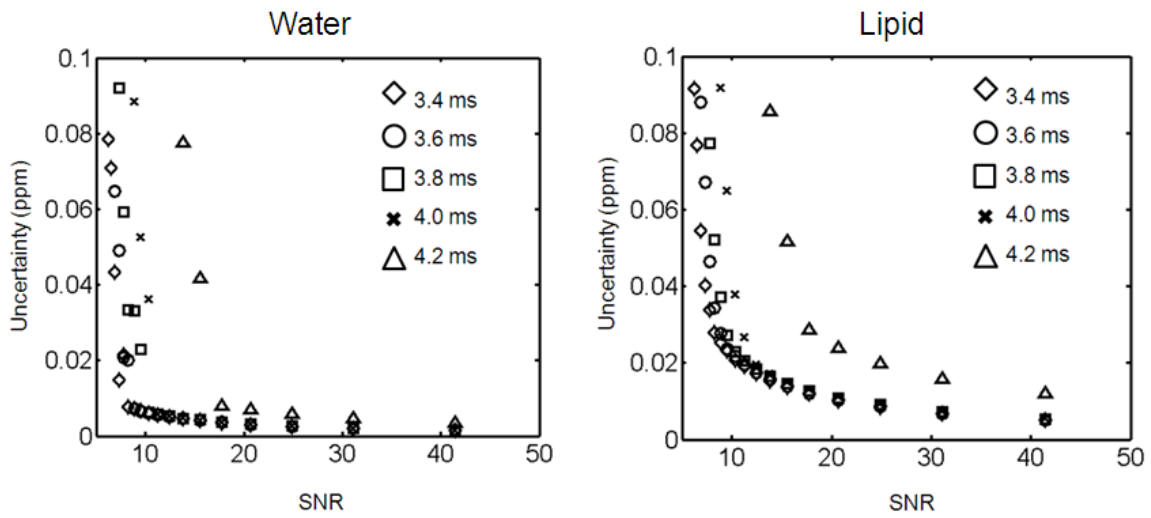
Figure 4-11 PRF precision as a function of SNR over variable ESP

As SNR increases, the precision of the PRF estimates increases. Even at an ESP where the lipid aliases into the lipid peak (4.2 ms), the water PRF can be measured with high precision. Therefore, if ESP values are chosen that may cause the lipid to alias to the water, higher SNR is needed to precisely measure the primary peak PRF.

4.4.3 ECHO TRAIN LENGTH

4.4.3.1 Materials and Methods

When SNR is high, then the ability to reduce the ETL is possible to either increase spatiotemporal resolution or increase the number of imaging planes. To test this, the agar water and lipid-water phantoms were scanned on a 1.5T clinical scanner (minimum TE (TE_0)=2.0 ms; ESP=3.3 ms; TR=69 ms; FA=30°; rBW=244 Hz/pixel, acquisition matrix=128x128; voxel volume=1.6x1.6x4.0 mm^3; 5 sec/image; parallel imaging acceleration factor=2) with ETL values of 4, 8, 12, and 16.

In addition, a second series of scans were obtained with the agar phantom using similar acquisition parameters except that the TR was adjusted where it would be the minimally allowed TR for a given ESP and ETL. The TR values chosen for ETL values of 4, 8, 12, and 16 were 14.1, 28.0, 41.0, and 54.0 ms, respectively. These resulted in acquisition times of 0.9, 1.8, 2.6, and 3.5 seconds, respectively. The uncertainties of the PRF, T_2* and amplitude were measured as a function of ETL.

4.4.3.2 Results

At a constant TR, the uncertainty in the measurement of each spectral parameter was found to be inversely proportional to the ETL (Figure 4-12). This is expected since the more samples obtained, the more likely the ARMA model can approximate the signal. Interestingly, even at an ETL of 4, the uncertainty was less than 0.01 ppm which is consistent what was seen in simulation (see Table 4-5). As long as the T_2* extends the longest TE (see Figure 4-4), the precision of the T_2* measurements increases with ETL

81

much as what is expected with exponential fitting of magnitude data. Also note that the dependence in the amplitudes is comparably less dependent on ETL in regards to PRF and T_2*. This is also consistent to what was seen in simulation (see section 4.3.2).
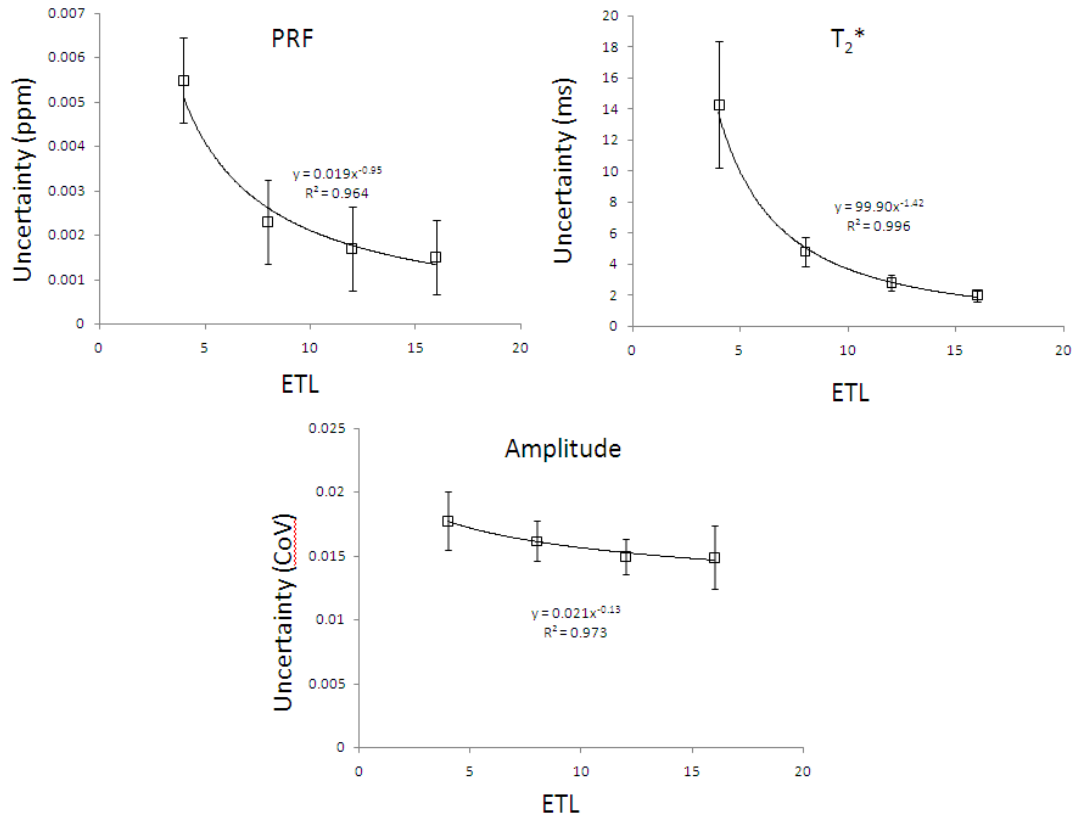
Figure 4-12 Influence of ETL on the precision of spectral estimates in a water phantom

Uncertainties in PRF (top left), T_2* (top right) and amplitude (bottom) are shown as a function of ETL. At a constant TR, the uncertainty in the measurement of each spectral parameter was found to be inversely proportional to the ETL. This is consistent with the simulations (150).

In the presence of lipid, the precision of each parameter stayed relatively constant at ETL values of 8, 12, and 16. When 4 echoes were used, the uncertainty of each

parameter increased. For temperature imaging, it appears that 8 echoes or more could possibly be used in planes where lipid and water are present in the same voxels.
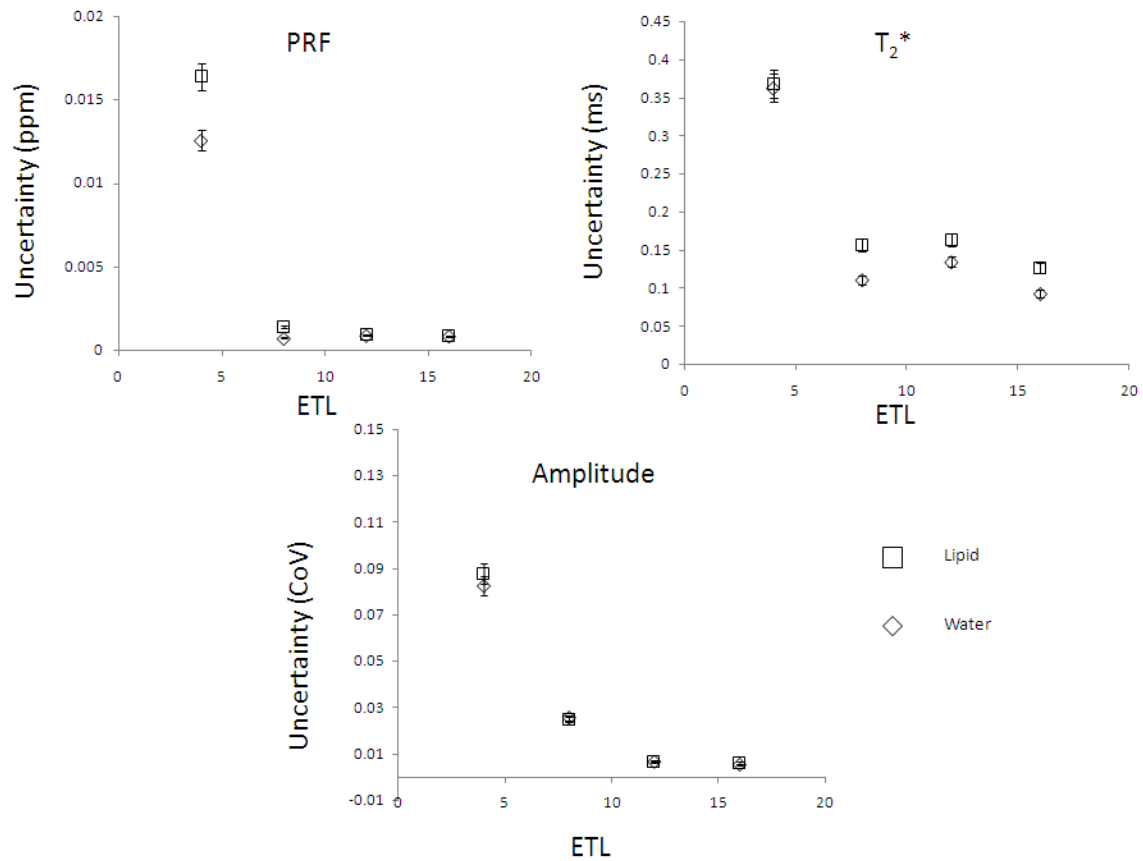
Figure 4-13 Influence of ETL on the precision of spectral estimates in a lipid-water phantom

Uncertainties in PRF (top left), T_2* (top right) and amplitude (bottom) are shown as a function of ETL in a lipid-water phantom. The uncertainty in the PRF is relatively constant from 8-16 echoes which suggest that 8 echoes could possibly be used in voxels with lipid and water for temperature imaging. There is higher uncertainty, however, in the amplitude estimates at 8 echoes.

Figure 4-14 shows the uncertainty in the spectral parameters when a shortened TR is used to increase the temporal resolution and maintain spatial resolution. Compared to the constant TR, the uncertainties were higher due to lower SNR. The uncertainties in the PRF at ETLs of 4 and 8 were statistically different ($p<0.01$ ppm and $p=0.02$, respectfully). When compared to the same ETL, all the T_2* and amplitude uncertainties where statistically different ($p<0.01$). As an illustrative example of how SNR plays a factor in the uncertainty, Figure 4-15 shows the constant TR case compared to the shorter TR acquisition where SNR losses due to the change the TR are accounted for.
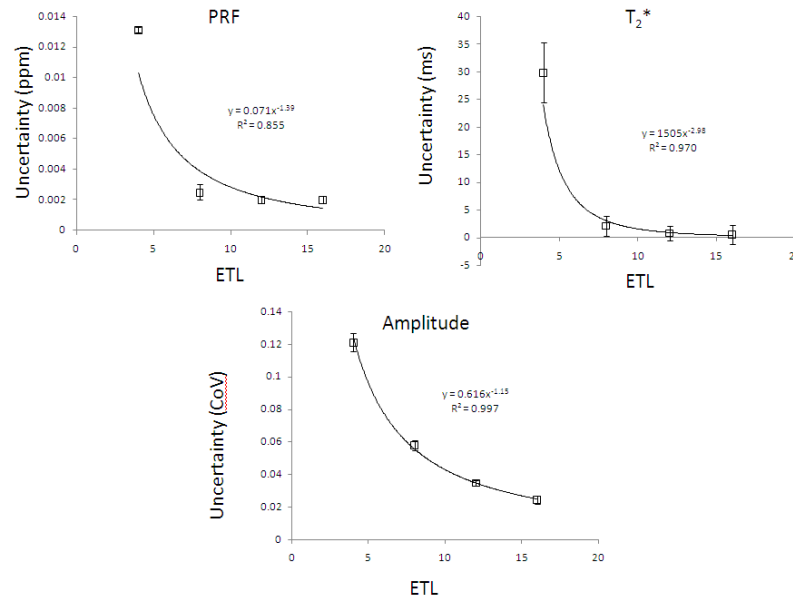
Figure 4-14 Influence of ETL on the precision of PRF, T_2*, and amplitude estimates

Uncertainties in PRF (top left), T_2* (top right) and amplitude (bottom) are shown as a function of ETL. At the shortest TR for the given ETL, the uncertainty in the measurement of each spectral parameter was found to be inversely proportional to the ETL. This dependence is higher than when a constant TR was used. The T_2* of the phantom was 63.4 ms.
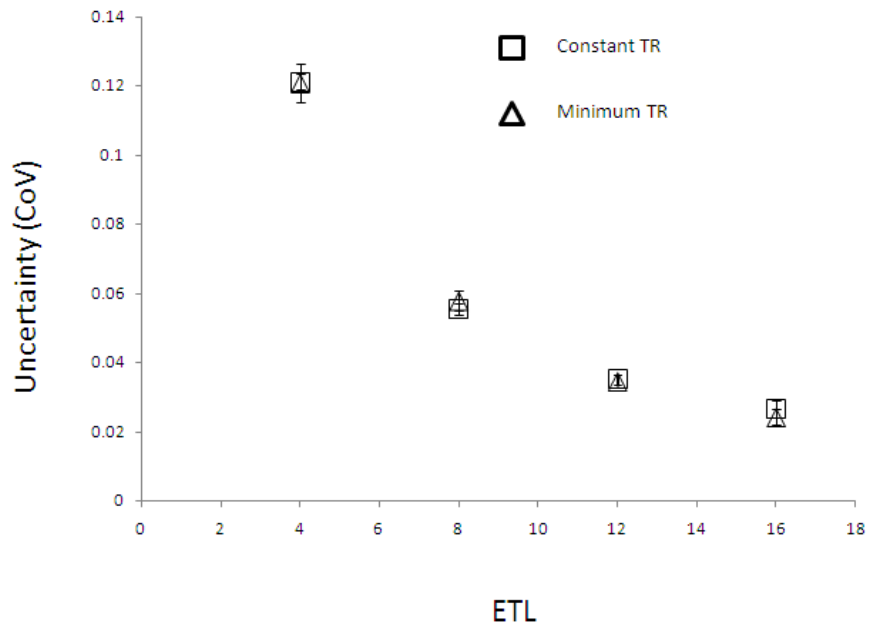
Figure 4-15 Uncertainties in the amplitudes with SNR compensation

At a shorter TR, the SNR of the acquisition will be lower. If the SNR of the constant TR acquisitions are decreased by compensating for the difference in TR, then it matches what was measured in the lower TR acquisitions. In other words, the lower TR acquisition suffers an SNR loss and this directly increases the uncertainty, as expected. In the amplitude estimate, the uncertainty in the lower TR scans are due purely from a difference in SNR.

4.4.4 PERFORMANCE OVER VARIABLE T_2*

4.4.4.1 Materials and Methods

To test the precision of the temperature estimates over a range of T_2* values, seven agar phantoms were created with varying concentrations of superparamagnetic iron oxides (SPIOs) which effectively changes the T_2* of phantom (151). The T_2* of each phantom was determined via exponential fitting using a standard SPGR sequence with varying TE. Using the determined acquisition parameters and spectral processing algorithms, field maps were made from all seven phantoms scanned (ETL:4-16; minimum TE (TE_0)=2.1 ms; ESP=3.3 ms; TR=69 ms; FA=30°; rBW=244 Hz/pixel, acquisition matrix=128x128; voxel volume=1.6x1.6x4.0 mm^3; 5 sec/image; parallel imaging acceleration factor=2). $\sigma_{\Delta f}$ SNR_A was measured in a 3 x 3 voxel ROI in each phantom. $\sigma_{\Delta \phi}$ was be measured in each ROI as well at each echo. Both $\sigma_{\Delta f}$ and $\sigma_{\Delta \phi}$ will be divided by the TSC to represent the uncertainty in temperature. A Student's t-test with equal variances (F-test tested) was employed to test for differences in the two precision values. If $\sigma_{\Delta f} < \sigma_{\Delta \phi}$ for each ROI , then the proposed technique will show increased sensitivity at that T_2* value. Using the SNR of the first echo and the measured T_2*, the CRLB was also calculated.

4.4.4.2 Results

Table 4-7 displays the uncertainty in the CSI and CPD measurements (the lowest over all the echoes) in each phantom. The CSI technique at least matched the CPD technique in terms of uncertainty and actually performed better at 6.4 and 21.2 ms

(*p*<0.05).   In every case, the CSI measurements matched the CRLB at the 95% confidence interval. Note that the CPD measurement was at the echo of least uncertainty. As will be discussed in the next chapter, the T_2* changes with temperature so the TE chosen for CPD methods may not be optimal over the entire course of treatment.   In the CSI method, we measured high precision without constraining to specific TE values (see equations 2-13 and 3-6).0   This data also supports published data obtained in *ex vivo* kidney tissue (53), which investigated the noise characteristics between CPD and this CSI technique.

Table 4-7 Noise characteristics of CSI and CPD over a range of T_2* values

T_2*	CRLB (°C)	Unc. CSI (°C)	Unc. CPD (°C)	p-value
6.4	1.52	1.21 ± 0.39	2.13 ± 0.74	0.03
12.9	0.21	0.20 ± .02	0.24 ± 0.07	0.24
14.6	0.17	0.18 ± .02	0.23 ± 0.09	0.21
21.2	0.11	0.11 ± 0.02	0.20 ± 0.06	0.02
47.1	0.07	0.07 ± 0.01	0.10 ± 0.05	0.18
51.6	0.07	0.06 ± 0.02	0.09 ± 0.04	0.25
63.4	0.07	0.07 ± 0.01	0.09 ± 0.03	0.38

The CSI technique at least matched the CPD technique in terms of uncertainty. At 6.4 and 21.2 ms, the uncertainty with the CSI technique was lower when compared to CPD. Each CSI noise measurement encompassed the CRLB at the 95% confidence interval while this was not always the case with CPD.

4.5 Discussion

What makes this work different from previously published work (37, 45-48, 152) is not the sequence itself, but rather the approach taken in setting acquisition parameters, the efficient use of the imaging time and data generated, and the approach to post-processing of the low resolution, aliased spectral data.

Our simulations and results from phantom studies demonstrate that processing algorithms discussed in this study can measure these frequency shifts with a high degree of accuracy even when the lipid peak is aliased, and that the SM algorithm is useful in overcoming the limitations of conventional windowed Fourier-based methods. The relaxation of the ESP constraint gave us the ability to use lower receiver bandwidths allowing higher SNR. Also, while only a few echoes were used, the relaxed ESP helped maintain reasonable spectral resolution. Additionally, the frequency difference between water and lipid is well known in the range of temperatures used for thermal therapy, so the ESP can be determined and ued to avoid problems with N/2 ghosts associated with bipolar readout gradients and aliasing the lipid peak too close to the water peak.

Another assumption we made was that we could accurately monitor peak shifts using only 16 echoes. While this could be accomplished using windowed Fourier techniques and peak finding routines, we applied a non-Fourier technique based on ARMA analysis of the data in order to provide a more robust method for finding peaks, as well as estimating the T_2^* and amplitude for each peak. This is in contrast to well-

known lipid-water separation techniques where peak amplitude quantification is of primary concern (128, 135, 137).

We observed robust performance of the SM algorithm in accuracy, uncertainty, and secondary peak detection across a range of SNR values for a very low number of echoes. The use of minimal samples represented as a rational polynomial in the *z*-domain, which has been shown to converge exponentially as the number of echoes increases (118), is important because this allows the acquisition either to run faster with less computational overhead or to facilitate the acquisition of multiple slices within the same TR period. For example, using the minimum TR possible with an ETL=8 and ESP=3.3 at 1.5T, acquisitions could be performed in less than two seconds. Three slices could be encoded in less than six seconds.

In addition to choosing a low number of echoes, the choice of other acquisition parameters, such as the ESP, can affect the accuracy and precision of the measurements. We have shown that choosing ESPs that extend TE_{max} past the T_2* of the tissue increases the uncertainty in the measurements (Figure 4-4). In low T_2* tissues or where there is low SNR in the later echoes, those echoes should be dropped since an increase in uncertainty has been observed. For instance, in a signal with a T_2*=10 ms, TE_{max}=51.2 ms and SNR=20, sampling 16 echoes gave an uncertainty of 0.0154 ppm whereas sampling 8 echoes reduces the uncertainty to 0.0044 ppm. Therefore, for signals with low SNR (<5) at the later echoes, it is better to exclude those echoes and proceed with a lower ETL than to include them.

Theoretical calculation of the CRLB demonstrates that the uncertainty is inversely proportional to the SNR, a relationship corroborated by simulation and phantom measurements. Therefore, MR acquisition parameters, such as the flip angle, should be chosen to increase the SNR of the peak of interest. For instance, in a one-peak system, the flip angle that provides maximum SNR is the Ernst angle. For two-peak systems in which information from both peaks is desired, acquisition parameters should be tailored to help increase the SNR of the secondary peak, which was assumed here to be the smaller of the two. If TR is fixed for optimal timing, the flip angle could be used to provide optimal modulation of the secondary peak signal.

Given adequate SNR, the acquisition used in this work could provide T_2^* maps of 8-10 slices in a single breathhold ($\leq$20 s) using ETL=8, while also providing inherent lipid suppression. A recent study in liver constrained the solution of the estimated tissue-based T_2^* for water by assuming equivalent T_2^* values for water and lipid, owing to a heavy iron overload (138). The authors concluded that this assumption may not be reasonable. The technique investigated here could potentially be used to separate these T_2^* values directly, without any assumptions on the chemical shift or T_2^* equivalency, thereby allowing identification of separate T_2^* values for water and lipid. Another potential application is quantitating the distribution of superparamagnetic iron oxides (SPIOs) (153). These particles have been suggested for use in thermal therapy, and such therapies could potentially benefit from the temperature imaging capabilities of our

technique as well (154).   Our data shows that precision can be maintained through a wide range of SPIO concentrations.

Our simulations and phantom experiments also show that for the same imaging time and parameters, this technique is more precise than current CPD techniques over a wide range of SNR values because it maintains better accuracy and precision across a variety of T_2^* values and thus improves sensitivity of temperature imaging (Fig. 4-16). Therefore, our data supports the hypothesis for increased accuracy and precision compared to CPD.
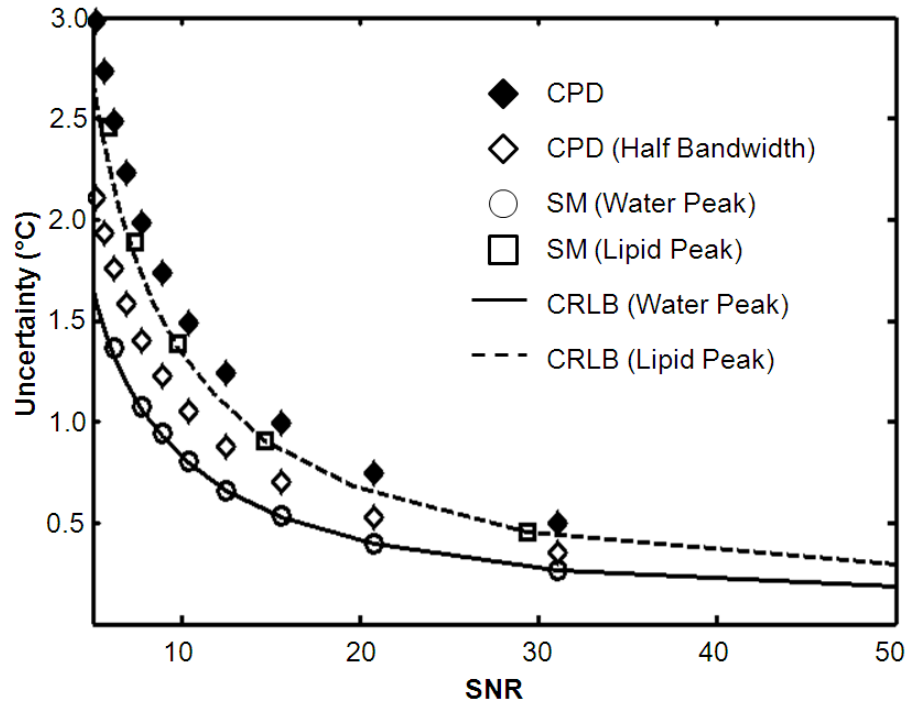
Figure 4-16 The uncertainty in temperature versus imaging SNR for a signal containing 25% lipid

The simulation (n = 20,000 samples) for evaluating the uncertainty in the signal for water using the SM algorithm (circles) is compared with CRLB results (solid line). Note that our algorithm stays close to the CRLB over a wide range of SNRs. For reference, the CPD results are shown for an optimal TE (TE=T_2*) at the same bandwidth as the 16-echo sequence (black diamonds) and at one half this bandwidth (white diamonds) as would more likely be used. This case also assumes that the CPD can perfectly remove the influence of the lipid signal, which is unlikely; thus, it stands as a "best case" scenario for CPD against our technique. As can be seen, in addition to providing lipid-water separation, the fast CSI approach easily outperforms the CPD approach across a large range of imaging SNR values for the same imaging time. Reprinted with permission from the American Association of Physicists in Medicine, (150).

Chapter 5: Fast CSI Temperature Measurements in Phantom and *Ex Vivo* Tissues

5.1 Introduction

The MR acquisition strategies and spectral processing algorithms discussed in chapter 4 were applied to thermal therapies in phantom and *ex vivo* tissues. The overall goal in this chapter is to show the increased accuracy and precision compared to calculating the complex phase difference (CPD) as well as to show the advantages of this technique for multi-parametric monitoring. First, calibrations of the PRF shift with temperature change in a lipid-water phantom as well as *ex vivo* canine bone marrow, brain, prostate, kidney and liver tissues were performed. These calibrations will be reported and discussed with emphasis on how the presence of lipid can affect the water PRF shift. Next, the temperature responses of R_2* and signal amplitude are measured in these tissues. These parameters, which are simultaneously measured with temperature, are investigated for their usefulness in thermal therapy monitoring.

5.2 PRF Calibration in Phantom

5.2.1 MATERIALS AND METHODS

A phantom containing 50% lemon juice and 50% mayonnaise (by volume) (45) was used in order to test the temperature monitoring capabilities of the MGE acquisition and SM algorithm in voxels containing homogenous lipid and water signals. The mixture was contained in a 50 ml plastic vial and placed in a calorimeter consisting of two insulated cups. A fluoroptic temperature monitoring fiber (M3300, Luxtron, Santa

Clara, CA) was placed in the phantom and the entire apparatus was placed in an 8-channel high resolution brain array (MRI Devices, Waukesha, WI) for imaging on a 1.5T clinical MR scanner (Excite HD, GE Healthcare, Waukesha, WI). The fluoroptic fiber was localized using T_1-W images. For this calibration experiment, the acquisition time was slowed to 10 seconds per acquisition to reduce the number of images acquired during the entire 15 minutes of continuous scanning. The MGE acquisition used a parallel imaging acquisition (SENSE) with an acceleration factor of 2. The minimum TE was set to 2.6 ms with an ESP of 3.3 ms (303 Hz spectral bandwidth) for the 16 acquired echoes. The TR was 140 ms and the acquired voxel volume was 0.78 x 1.6 x 3.0 mm. The flip angle was set to 60° to increase the lipid signal. The receiver bandwidth to achieve the desired ESP was ±41.7 kHz (325 Hz/pixel) with a matrix size of 128 (phase encodes) x 256 (frequency encodes). After acquisition of 3 baseline scans, 300 ml of 90°C water was poured through a tube into the calorimeter. The imaging plane was chosen so that the flowing water in the image was in the frequency encode direction to avoid artifacts in the phase-encode direction associated with the aliasing from the SENSE-parallel imaging acquisition. In addition, the volume of water used was limited to keep the water signal from appearing in the coronal slice we were monitoring.

A 2x2-voxel region of interest (ROI) was selected at the point in the image at the end of the fluoroptic probe. The SM algorithm was also employed to estimate the water and bulk methylene PRF shifts. Peak shifts estimated by the technique were plotted against the temperature measured by the fluoroptic probe in order to calculate the

temperature sensitivity coefficient in ppm/°C. Linear fits were calculated for the plot using least-squares regression.

Maps were created using the CPD method at the echo time close to the lipid T_2* (TE = 32.6 ms). A Student's *t*-test was used to find statistical significance between the temperature readings from these three methods and the fluoroptic fiber's measurements.

5.2.2 RESULTS

Temperature calibration curves for the lipid-water phantom experiment using the SM algorithm are shown in Figure 5-1. The temperature sensitivity coefficients calculated for each curve were -0.0096 ± 0.0003 ppm/°C (Pearson's R^2 = 0.995) and -0.0007 ± 0.0005 ppm/°C (Pearson's R^2 = 0.436) for water and lipid, respectively. The temperature sensitivity coefficient based on the difference between the lipid and water peaks was -0.0088 ± 0.0005 ppm/°C (Pearson's R^2 = 0.994) and this value is similar to published data when the water PRF accounted or corrected for susceptibility (37, 43, 45).
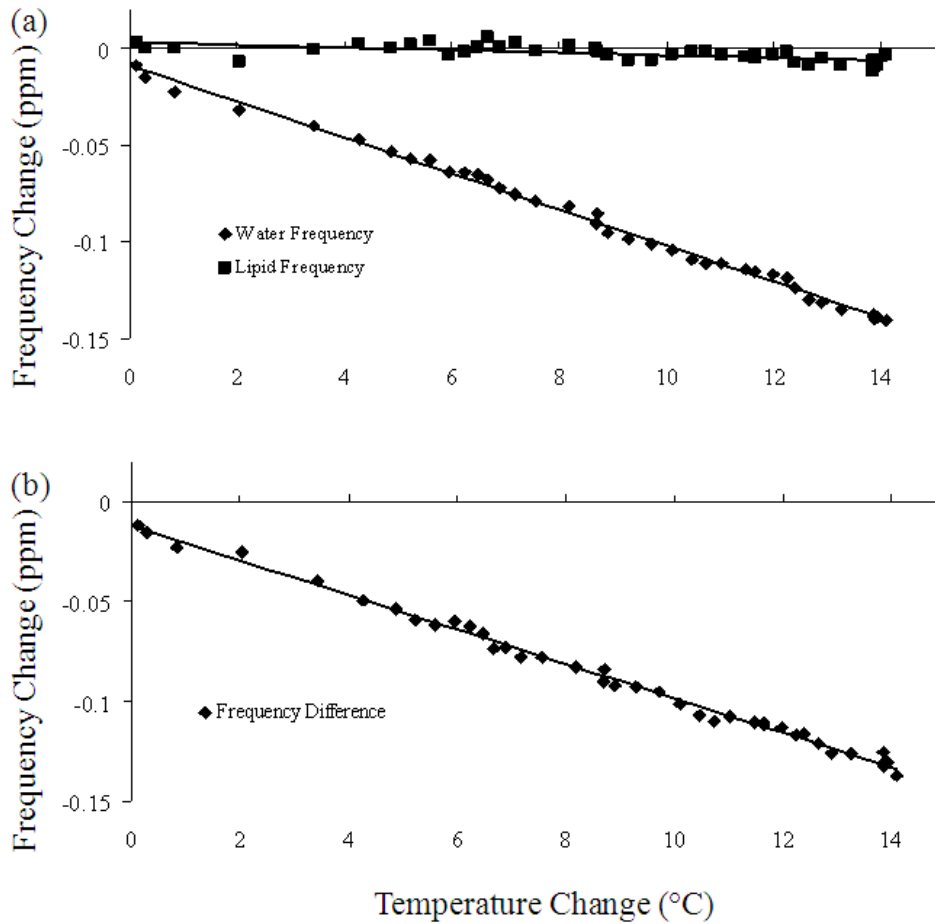
Figure 5-1 The temperature calibration curves of the lipid-water phantom

The lipid and water curves are shown in (a) and the difference between the two peaks, δ_{w-l}, in (b). A strong linear dependence can be seen in the water peak and the difference between the peaks." The temperature sensitivity coefficients calculated for each curve were -0.0096 ± 0.0003 ppm/°C (Pearson's R^2 = 0.995), -0.0007 ± 0.0005 ppm/°C (Pearson's R^2 = 0.436) and -0.0088 ± 0.0005 ppm/°C (Pearson's R^2 = 0.994) for water, lipid and the difference in the PRF values, respectively. Reprinted with permission from the American Association of Physicists in Medicine, (53).

Temperature measurements with and without using a lipid reference as well as the CPD measurements were obtained (Fig. 5-2). The calculations were performed using the same ROI where the calibration data was measured. During the calibration, the hot water poured into the calorimeter caused a large shift in the mixture's water and lipid resonance frequencies. This caused the RMSE for the CPD and water CSI temperature readings to be 21.3 °C and 20.3 °C, respectfully. These two measurements were significantly different when compared to the fluoroptic fiber measurements ($p<0.0001$). However, when lipid was used as an internal reference the temperature remained accurate when compared to the fluoroptic fiber measurements. The RMSE between the lipid-referenced CSI and the fluoroptic fiber was 0.44 ± 0.34 °C. There was no statistically significant difference between the CSI using lipid as a reference and the fluoroptic fiber measurements over all the time points.
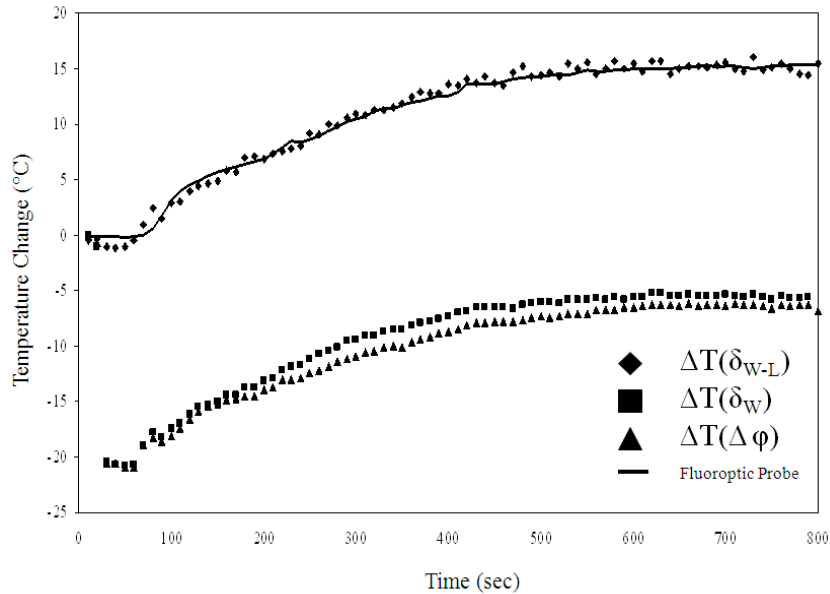
Figure 5-2 The measured change in temperature in the lipid-water phantom over time

Field shifts from the pouring water causes the CPD ($\Delta T(\Delta\varphi)$) and CSI (water frequency only, $\Delta T(\delta_W)$) to be 21.3 °C and 20.3 °C, respectfully. The CSI using lipid ($\Delta T(\delta_{W-L})$) as a reference corrects this error. Reprinted with permission from the American Association of Physicists in Medicine, (53).

5.3 PRF Calibration in Ex Vivo Tissue

5.3.1 MATERIALS AND METHODS

Canine bone marrow, brain, kidney, liver and prostate tissue were treated with a water-cooled applicator housing a 980-nm laser fiber with a 1-cm diffusing tip powered by a 15 W diode laser source (BioTex Inc., Houston, TX) on a clinical MR scanners at 1.5T (Excite HD, GE Healthcare, Waukesha, WI) and 3T (TwinSpeed Excite HD, GE Healthcare, Waukesha, WI). A fluoroptic temperature probe (M3300, Luxtron, Santa

98

Clara, CA) was inserted in order to provide an absolute measurement of temperature. In each ablation, the multi-gradient echo (MGE) acquisition was used (1.5T: ETL=16 echoes; minimum TE (TE_0)=2.0 ms; ESP=3.2 ms; TR=69 ms; FA=30-40°; rBW=244 Hz/pixel, acquisition matrix=128x128; voxel volume=1.6x1.6x4.0 mm^3; 5 sec/image; parallel imaging acceleration factor=2. 3T: TE_0=2.1 ms; ESP=1.8 ms; rBW=325 Hz/pixel). Echoes were acquired with identical polarity gradients separated by flyback rewinder gradients.

A 2 x 2-voxel ROI adjacent to the sensitive region of the fluoroptic probe was chosen and the PRFs were measured as a function of temperature to calculate the temperature sensitivity coefficient (TSC). The water PRF was measured for all tissues. For bone marrow, water and bulk methylene proton resonances were measured at 1.5T while terminal methylene and methyl peaks were included in studies at 3.0T. Slope, intercept, and correlation coefficient measurements were calculated for each temperature sensitivity calibration using linear least-squares regression analysis. The temperature estimates using the calculated TSC were correlated to the fluoroptic probe measurements. Estimates were also compared to CPD-measured water PRF calibration using a paired two-tailed Student's *t*-test. Estimated uncertainties (noise) from each calculated parameter in bone marrow were measured as the standard deviation and compared with the calculated CRLB for the acquisition, which represents the theoretical lower bound of the uncertainty (54, 150). Temperature uncertainties calculated from the measured TSC

and PRF uncertainties were compared to temperature uncertainties from the complex-phase difference using the echo from the MGE acquisition with the least uncertainty.

5.3.2 *RESULTS*

In bone marrow, water, bulk methylene, terminal methylene and methyl peaks were resolvable at 1.5T and 3.0T. Figure 5-3 demonstrates representative modeled spectra from *ex vivo* bone marrow observed using the spectral parameters derived from the SM algorithm at 1.5T (a) versus the unfiltered FFT spectrum (with 1024 zero padded interpolation) and the modeled spectra at 3.0T (b). The SM algorithm rapidly and accurately located water and lipid chemical shifts despite the low spectral resolution of the acquisition, which caused large sidelobe contamination in the Fourier analysis. Although spectral apodization techniques could be employed with the FFT technique, the tradeoff is one of spectral resolution versus sidelobe interference. In (b), as temperature rises, the water peak shows a notable shift in the PRF compared to the three lipid peaks. Spectra obtained from a point resolved spectroscopy (PRESS) (TE/TR: 144/2000) acquisition show the unaliased lipid peaks and the water peak (c).
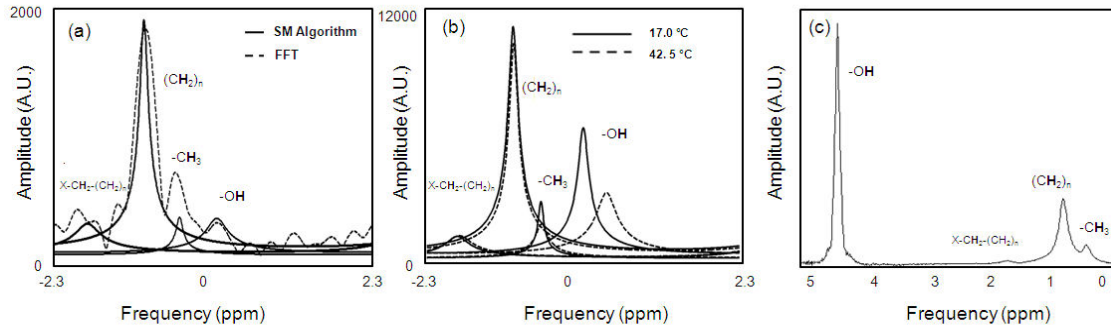
Figure 5-3 Representative measured bone marrow spectra from 16-echo MGE and PRESS

At 1.5T (a) a 4-peak ARMA modeling (solid) versus unfiltered FFT (1024 point interpolation) (dashed). As previously confirmed (17), ARMA peak locations do not suffer from truncation artifacts. At 3.0T (b) four-peak model at 17.0°C (solid) and 42.5°C (dashed) demonstrates temperature dependent water PRF and temperature independence of lipid peak PRFs. For comparison, a spectrum from a PRESS acquisition is shown in (c).

As expected, excellent correlation with fluoroptic temperature measurements were observed in the water PRF but not in the lipid PRF. The data in Table 5-1 quantifies temperature relationships observed during calibrations at 1.5T over the temperature range of 17.2 to 57.0 °C. Figure 5-4 demonstrates the change in the water (squares) and bulk methylene (diamonds) PRF as a function of fluoroptic temperature measurement at 1.5T. The TSC of the difference between the water and lipid PRF values in both calibrations were found to be statistically equivalent ($-0.87 \times 10^{-2} \pm 2.7 \times 10^{-6}$ ppm/°C ($R^2 = 0.942$), $-0.87 \times 10^{-2} \pm 4.6 \times 10^{-4}$ ppm/°C ($R^2 = 0.961$) and $-0.85 \times 10^{-2} \pm 3.2 \times 10^{-4}$ ($R^2 = 0.920$), $0.17 < p < 0.99$). Using these TSC values, the RMSE between the temperature estimates and the fluoroptic probe was 0.39 ±0.21°C (Range: -0.29 – 0.90 °C) for calibration 1, 0.96 ± 0.25°C (Range: -0.54 – 1.13 °C) for calibration 2 and 0.54 ± 0.13 °C (Range: -0.84 – 0.93 °C) for calibration 3. If the temperature measurements were

made using water PRF without lipid correction along with the TSC of the water PRF only, the RMSE values were 1.03 ±0.12 °C (Range: -1.36 – 1.69 °C), 2.11 ± 0.24 °C (Range: -1.41 – 2.69 °C) and 1.31 ± 0.31°C (Range: -1.22 – 2.91 °C) for calibrations 1, 2 and 3, respectively. The CPD RMSE was 2.34 ± 0.25 °C, which was statistically different from the CSI measurements (p<0.001).

Table 5-1 Measured PRF temperature sensitivity coefficients from three bone marrow calibrations at 1.5T

Chemical Shift	Temperature Sensitivity Coefficient [ppm/°C] (R^2)		
Water	$-1.07 \times 10^{-2} \pm 1.0 \times 10^{-4}$ (0.981)	$-1.11 \times 10^{-2} \pm 2.4 \times 10^{-4}$ (0.974)	$-0.98 \times 10^{-2} \pm 1.3 \times 10^{-4}$ (0.969)
Bulk Methylene	$-0.20 \times 10^{-2} \pm 1.0 \times 10^{-4}$ (0.438)	$-0.24 \times 10^{-2} \pm 1.5 \times 10^{-4}$ (0.738)	$-0.12 \times 10^{-2} \pm 1.1 \times 10^{-4}$ (0.440)
Difference	$-0.87 \times 10^{-2} \pm 2.7 \times 10^{-4}$ (0.942)	$-0.87 \times 10^{-2} \pm 4.0 \times 10^{-4}$ (0.961)	$-0.85 \times 10^{-2} \pm 3.2 \times 10^{-4}$ (0.920)

The difference is between the water and bulk methylene PRFs which is consistent between calibrations and agrees with lipid-water phantom data (45, 53).
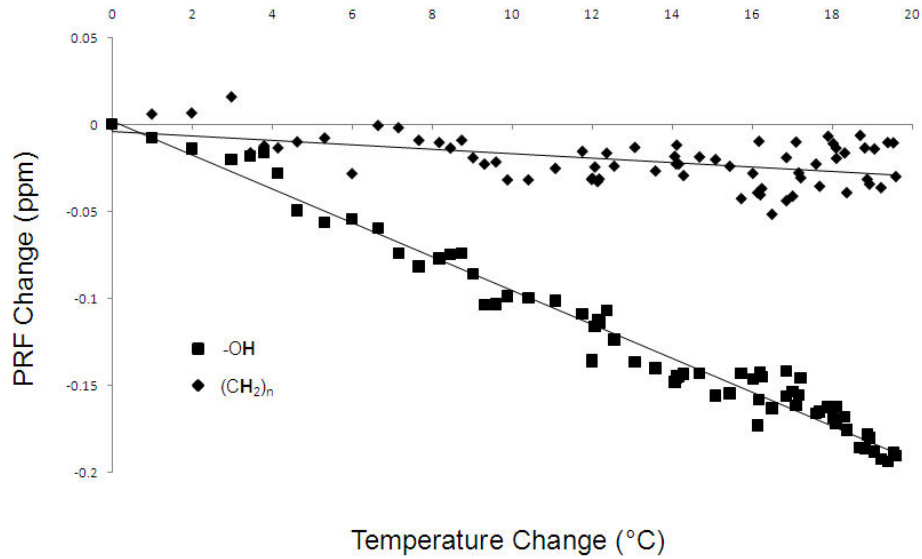
Figure 5-4 Temperature calibration curves for one bone marrow calibration at 1.5T

The temperature sensitivity coefficients (TSCs) of the water (squares) and lipid (diamonds) PRFs were -0.98x10^{-2} ± 1.3x10^{-4} (R^2=0.969) and -0.12x10^{-2} ± 1.1x10^{-4} (R^2=0.440), respectfully. By taking the difference of the two PRFs as a function of temperature, the TSC was -0.85x10^{-2} ± 3.2x10^{-4} (R^2=0.920).

The temperature measurements from the CSI technique compared to the true temperature calculated by the fluoroptic probe in calibration 1 are shown in Figure 5-5. The slopes of the regression lines for the water-bulk methylene temperature readings and the water PRF were 0.999 ± 0.021 ppm/°C (R^2=0.987) and 0.988 ± 0.072 ppm/°C (R^2=0.942) with intercepts at 0.03°C and 1.01°C, respectfully. For comparison, the solid line shown has a slope of unity. If the difference in the water PRF alone was used for temperature monitoring, it would tend to overestimate the temperature ($p<0.001$).
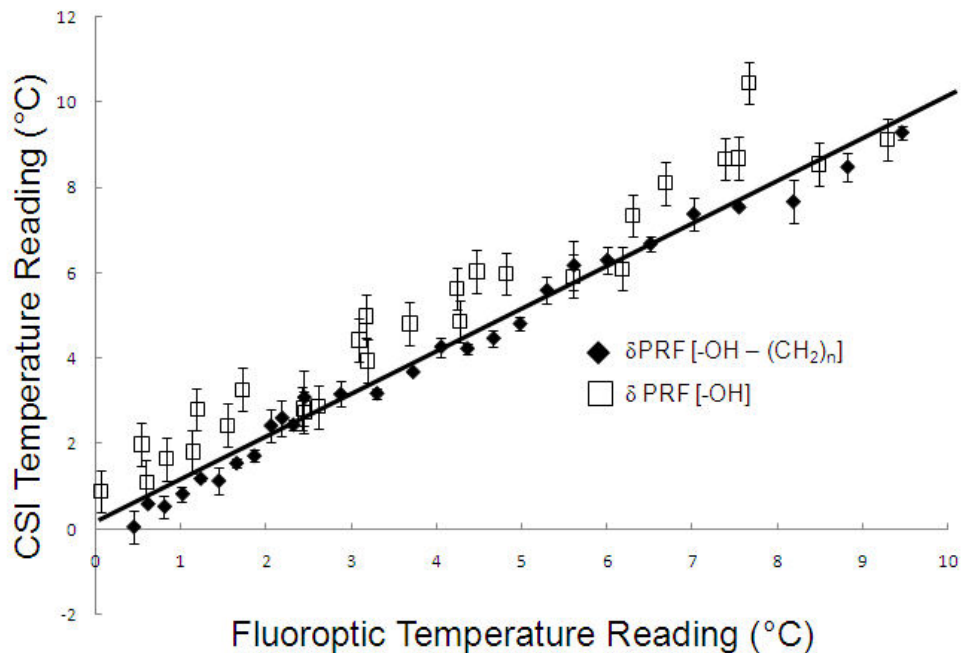
Figure 5-5 Temperature measurements from the CSI technique compared to the true temperature calculated by the fluoroptic probe.

The RMSE for the susceptibility-corrected temperature readings and the water PRF readings were 0.393 °C and 1.031 °C. The slopes of the regression lines for the water-lipid temperature readings and the water PRF were 0.999 (R^2=0.987) and 0.988 (R^2=0.942) with intercepts at 0.030°C and 1.014°C, respectfully. For comparison, the line shown in the figure has a slope of unity.

The measured uncertainties in the spectral parameter estimations made using the 2-peak model at 1.5T are summarized in Table 5-2. Values in parentheses are the calculated theoretical uncertainty for the acquisition provided by the CRLB. The measured uncertainties agree with the CRLB at the 95% confidence interval. Using the calculated TSC values, the temperature uncertainty was calculated as 0.58 ± 0.09 °C when the difference of the water and lipid PRF values was used for temperature

measurements. Comparably, the uncertainty in the CPD was measured as 1.46 ± 0.19°C using the echo from the acquisition with the least uncertainty (TE=14.8 ms) (p<0.01).

Table 5-2 Measured uncertainties in the estimated spectral parameters in bone marrow at 1.5T

Parameter	Water (CRLB)	Bulk Methylene (CRLB)
PRF (ppm)	0.00355 ± 0.00054 (0.004)	0.00191 ± 0.00035 (0.002)
T2* (ms)	2.27 ± 0.51 (2.22)	0.48 ± 0.14 (0.57)
Amplitude (CoV)	0.023 ± 0.009 (0.018)	0.017 ± 0.004 (0.015)

The CRLB is within the 95% confidence interval in each of the parameters.

The mean spectral parameter estimations measured at 3.0T resulting from application of a 4-peak model in bone marrow are also summarized in Table 5-3. The TSCs of these peaks over a temperature range of 18.4 to 57.2 °C are shown in Table 5-4. As with the 1.5T calibrations, the water-bulk methylene TSC was statistically equivalent (p=0.11). Using the temperature sensitivity of the difference in the water and bulk methylene PRF, the RMSE values compared to the fluoroptic probe were 0.19 ±0.06°C and 0.59 ± 0.24°C for the two calibrations. Using CPD with a TE of 9.1 ms, the RMSE was 1.89 ± 0.15°C. This was statistically different from the CSI RMSE (p<0.001). The noise in the temperature estimates using bulk methylene as an internal reference was measured at 0.78 ± 0.08 °C. The noise in the temperature estimates were higher, 2.87 ± 0.05 °C and 3.21 ± 1.12 °C, when using the lower SNR terminal methylene and methyl protons, respectively, as internal references. Using the mean of all three lipid peaks as a reference, the uncertainty was lower at 1.00 ± 0.02 °C. Using the water peak only with its measured TSC, uncertainty was 0.91 ± 0.38 °C. Uncertainty in the CPD was measured as

1.93 ± 0.70°C using the echo with the least uncertainty (TE=9.1 ms) ($p<0.01$ when compared to CSI with lipid as a reference).

Table 5-3 Measured PRF, T_2^* and amplitude values with associated uncertainties for water, bulk methylene, terminal methylene and methyl protons using a four-peak model at 19 °C

Chemical Shift	PRF (ppm)	T_2^* (ms)	Amplitude (Normalized)
Water	4.6856 ± 0.0091	56.2 ± 8.9	0.575 ± 0.054
Bulk Methylene	1.1856 ± 0.0074	9.5 ± 0.2	1.000 ± 0.014
Terminal Methylene	2.0285 ± 0.0044	3.6± 0.4	0.297 ± 0.014
Methyl	0.8631 ± 0.0153	18.1 ± 0.7	0.369 ± 0.062

Peaks were identified in the expected locations (155). The water T_2^* is within range of previous T_2 measurements in bone marrow (156).

Table 5-4 Measured PRF temperature sensitivity coefficients from multiple protons at 3.0T

Chemical Shift	TSC [ppm/°C] (R^2)	
Water	$-1.03 \times 10^{-2} \pm 1.4 \times 10^{-4}$ (0.978)	$-1.28 \times 10^{-2} \pm 2.3 \times 10^{-4}$ (0.981)
Bulk Methylene	$-0.15 \times 10^{-2} \pm 0.9 \times 10^{-4}$ (0.904)	$-0.42 \times 10^{-2} \pm 3.1 \times 10^{-4}$ (0.972)
Terminal Methylene	$-0.19 \times 10^{-2} \pm 2.7 \times 10^{-4}$ (0.211)	$-0.44 \times 10^{-2} \pm 4.4 \times 10^{-4}$ (0.487)
Methyl	$-0.70 \times 10^{-2} \pm 3.1 \times 10^{-4}$ (0.618)	$-0.84 \times 10^{-2} \pm 4.7 \times 10^{-4}$ (0.816)
Water – B. Methylene	$-0.88 \times 10^{-2} \pm 3.0 \times 10^{-4}$ (0.917)	$-0.86 \times 10^{-2} \pm 2.3 \times 10^{-4}$ (0.964)

As with the 1.5T calibrations, the difference between the water and bulk methylene PRFs are consistent to literature (45, 53). Temperature sensitivities of terminal methylene and methyl protons are also listed.

Table 5-5 displays the TSC of each of the tissues along with the temperature range measured in the calibration. All TSC are within the 95% confidence interval of what has been measured in soft tissue (-0.0097 ppm/°C with an exception of -0.0098 ppm/°C for brain (157)). In calibrations, where the temperature exceeded the break point for thermal damage, there were no shifts in linearity.

106

Table 5-5 Temperature sensitivity coefficients in various non-fatty tissues

Tissue Type	Temp. Range (°C)	Temp. Sensitivity (ppm/°C) (R^2)
Brain	25-59	-0.0102 ± 0.0005 (0.998)
Prostate	32-59	-0.0099 ± 0.0004 (0.995)
Kidney	35-54	-0.0103 ± 0.0006 (0.994)
Liver	35-51	-0.0098 ± 0.0002 (0.984)

TSC values were within the expected values in soft tissues. There were no shifts in linearity in the PRF.

Table 5-6 displays the RMSE and uncertainty of each tissue using CSI and CPD. CSI had lower RMSE and uncertainty compared to CPD which supports our hypothesis of greater precision and accuracy using the CSI technique.

Table 5-6 Temperature accuracy and precision in various non-fatty tissues

Tissue Type	CSI RMSE (°C)	CPD RMSE (°C)	p-value	CSI Unc. (°C)	CPD Unc. (°C)	p-value
Brain	0.96 ± 0.14	1.69 ± 0.24	0.01	0.23 ± 0.11	0.56 ± 0.14	0.03
Prostate	0.24 ± 0.09	1.09 ± 0.40	0.02	0.20 ± 0.09	0.66 ± 0.10	0.02
Kidney	0.29 ± 0.05	2.03 ± 0.67	0.01	0.28 ± 0.24	0.86 ± 0.17	0.02
Liver	0.58 ± 0.16	1.25 ± 0.10	<0.01	0.32 ± 0.08	0.88 ± 0.11	<0.01

In support of our hypothesis, the accuracy and precision in temperature measurements in non-fatty tissues were statistically higher with CSI compared to CPD.

5.3.3 DISCUSSION

In calibration experiments at 1.5T and 3.0T in tissues containing lipid, PRF TSC values consistent with previous studies (43, 45) were observed when the difference between the water and bulk methylene PRFs are used for temperature estimation. In fatty tissue, De Poorter et al. (43) measured an overall TSC of -0.0097 ppm/°C with a susceptibility constant of -0.0013 ppm/°C giving a corrected field shift of -0.0088 ppm/°C, which is consistent with results reported here.   McDannold et al. (45) measured

similar TSC values in a mayonnaise-lemon juice phantom which was designed similarly to our phantom study. As expected, using water PRF shift alone did not result in consistent temperature sensitivities due to varying degrees of susceptibility and drift between experiments. For example, at 3.0T in bone marrow the water PRF was highly linear with temperature (R^2=0.981). However, its TSC was approximately 15-19% higher in one calibration than what was seen at 1.5T. When the difference between the water and bulk methylene was taken to effect to correct for susceptibility, the TSC was measured as -0.0086 ± 0.0002 ppm/°C, within the 95% confidence interval of the measurements taken at 1.5T. Using the measured TSC by taking the difference between water and bulk methylene protons, we measured accurate temperature readings in each experiment (0.44 °C in phantom; 0.96 °C, 0.39 °C, and 0.54 °C in bone marrow at 1.5T; 0.19 °C and 0.59 °C in bone marrow at 3.0T). It is very important to note that this susceptibility effect on the temperature sensitivity of lipid-containing tissue is independent of whether or not lipids are suppressed. In addition, although the RMSE and uncertainty were lower compared to single-echo CPD, one could reduce the acquisition time and/or bandwidth (to increase SNR) to improve accuracy and precision with CPD techniques. This would not, however, account for susceptibility or field drift effects that were seen in the water PRF measurements.

The phantom and bone marrow study exemplifies the advantage of having a lipid peak as a reference when relatively large susceptibility or field shifts occur. There was no large susceptibility shifts seen in the non-fatty tissue in brain, prostate, kidney and

liver compared to the bone marrow. This may be due to the interfaces in the cortical bone and the added susceptibility from the high lipid content in the marrow. From these measurements, there appears to be an increased susceptibility effect from the presence of lipid which makes measurements difficult with CPD.

To our knowledge, no MR thermometry study has investigated the temperature sensitivity of multiple lipid peaks simultaneously with this level of spatiotemporal resolution. It was found that although the terminal methylene peaks and methyl peaks could be resolved in bone marrow at 1.5T, the uncertainty was on the order of 0.03-0.08 ppm making calibrations difficult to ascertain with confidence. At 3.0T, each of the four peaks had sufficient SNR and spectral resolution for precise measurements so that the temperature dependence of each component of the lipid peak could be analyzed. When using lipid for an internal, temperature independent, reference, highest accuracy and precision was demonstrated with bulk methylene for PRF-based reference thermometry. This was primarily due to a smaller uncertainty in the measurement and is likely due to the higher SNR of bulk methylene compared to the other lipid protons.

In many lesions in fatty tissue, the primary component will be water, especially in the center of the lesion. If no lipid is present, we expect high precision with temperature measurements as seen in our simulation outlined in chapter 4. However, toward the borders of the lesion voxels may contain lipid. It is important that lipid is taken account for in order to accurately measure the temperature, identify the borders of the ablative region, and verify if the entire lesion received an adequate thermal dose. Also,

109

extrapolating the lipid field map into the lesion, much like what has been done with referenceless thermometry (158), could possibly be performed to improve temperature estimates in bone lesions and warrants investigation.

As in our simulations, our phantom and *ex vivo* data support our hypothesis that this CSI technique provides higher precision and accuracy compared to the CPD measurements. However, as seen in the bone study, it is important to identify the peaks correctly in order to apply the appropriate TSC. The next chapter will address this by evaluating an algorithm which identifies water and lipid peaks and maps their spectral parameters to aid in improving temperature imaging.

5.4 Multi-Parametric Analysis in Ex Vivo Tissue

5.4.1 MATERIALS AND METHODS

Canine bone marrow, brain, kidney, liver and prostate tissue were treated with a water-cooled applicator housing a 980-nm laser fiber with a 1-cm diffusing tip powered by a 15 W diode laser source (BioTex Inc., Houston, TX) on clinical MR scanners at 1.5T (Excite HD, GE Healthcare, Waukesha, WI) and 3T (TwinSpeed Excite HD, GE Healthcare, Waukesha, WI). A fluoroptic temperature probe (M3300, Luxtron, Santa Clara, CA) was inserted in order to provide an absolute measurement of temperature. In each ablation, the MGE acquisition was used (1.5T: ETL=16 echoes; minimum TE (TE_0)=2.0 ms; ESP=3.2 ms; TR=69 ms; FA=30-40°; rBW=244 Hz/pixel, acquisition matrix=128x128; voxel volume=1.6x1.6x4.0 mm^3; 5 sec/image; parallel imaging

acceleration factor=2. 3T: TE_0=2.1 ms; ESP=1.8 ms; rBW=325 Hz/pixel). Echoes were acquired with unipolar gradients separated by flyback rewinder gradients. ROIs (2 x 2 voxels) were chosen in areas that reached ablative temperatures ($\geq$54 °C) with each pixel processed individually. Using the calculated TSC values from water (and bulk methylene PRF, if present, as an internal reference), the changes in the PRFs were converted to temperature changes and added to the baseline temperature provided by the fluoroptic temperature probe; thereby providing absolute temperature readings.

In at least five ROIs in each tissue type, the water R_2* was measured. As will be shown in the results, each plot of R_2* displayed an inflection point. Blinded by the temperature and thermal dose data, data points were labeled as 0 before the inflection point and 1 after the inflection point with respect to time on the R_2* plot. The inflection point was defined as the point after a local maximum or minimum R_2* with five consecutively decreasing or increasing values after the local maximum or minimum. Next, binomial logit analysis was used to fit the data as a function of thermal dose. The probability, *P,* of the logit curve is defined as

$$P = \frac{1}{1 - e^{\alpha + \beta \Omega}} \qquad \text{(5.1)}$$

where α and β are coefficients determined by the fit.

The dose was calculated from the Arrhenius rate model for thermal damage where

$$\Omega = \int_0^t Ae^{\frac{-E_a}{RT(\tau)}} d\tau \qquad \qquad \textbf{(5.2)}$$

A is the frequency factor, E_a is the activation energy, R is the universal gas constant

$(8.315 \text{ JK}^{-1}\text{mol}^{-1})$ and $T(\tau)$ is the temperature in degrees Celsius as a function of time, τ

(26). A and E_a values were chosen to predict protein denaturation (A: $3.1 \times 10^{98} \text{ s}^{-1}$, E_a:

$6.3 \times 10^5 \text{ J mol}^{-1}$) (25). $\Omega{\geq}1$ signified tissue damage and this threshold has been used in

previous studies (159, 160). The dose was recorded where the probability of the fit

equaled 0.5 (also known as LD50). The fraction of damage cells ($C(\tau)/C(o)$, equation

1.4) was also calculated. The purpose of this measurement was to characterize the signal

change as a function of thermal dose to determine if the changes occurred where damage

was expected to occur. The slopes of lines were measured before and after the inflection

point with respect to temperature and compared using a two-tailed Student's t-test with

equal variances (as determined by an F-Test).

5.4.2 RESULTS

Figure 5-6 displays the logit fits for each of the tissues along with a logit fit for all

the tissues combined. Table 5-7 also shows the LD50 with uncertainty. In each case, an

Ω of 1 was within the 95% confidence interval for LD50. In the formulism by Henriques

(25), this value was used to signify irreversible damage by protein denaturation.
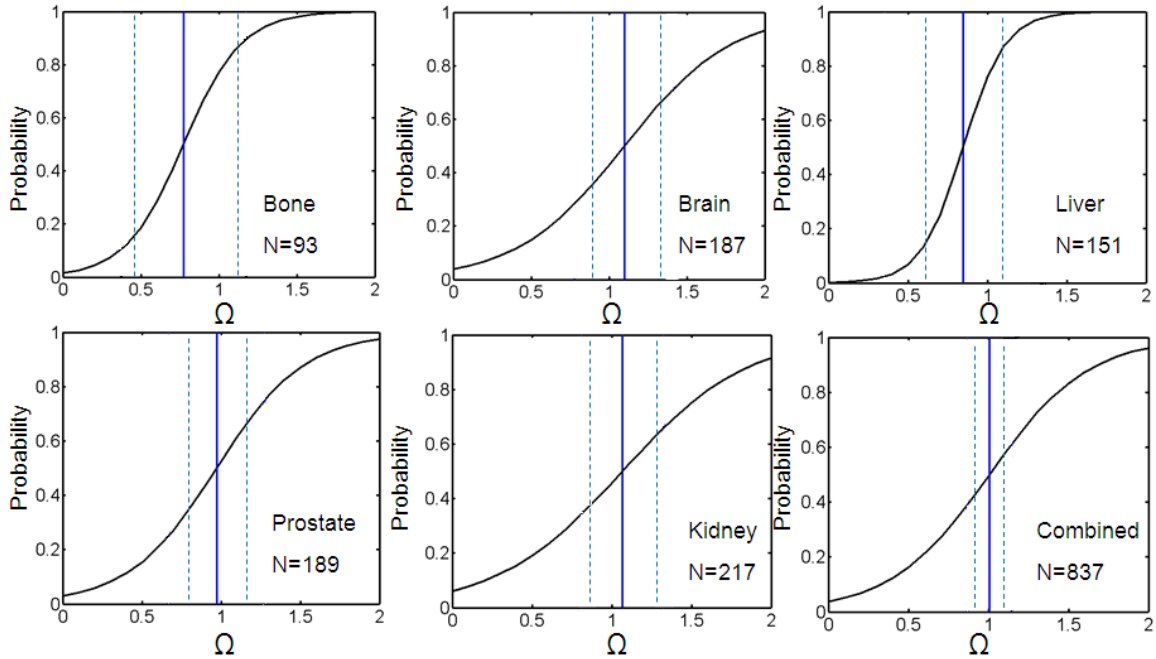
Figure 5-6 Logit fits for bone marrow, brain, liver, prostate and kidney tissue

Using binomial logit analysis, the probability of 0.5 that a R_2* change occurred were at thermal dose values known to cause irreversible damage as shown by Henriques (25). The black line is the logit fit. The blue solid and dashed lines are the LD50 values and the standard error, respectively. The circles are binary data points for the curve fitting. Note that there are several binary points beyond $\Omega=2$ (Range: $0\text{-}1.49\text{x}10^7$). N is the number of binary points. This shows that the R_2* changes are occurring where damage is expected to occur.

Table 5-7 Measured LD50 values for various tissues with associated confidence intervals

Tissue	LD50 (Ω)	95% CI	α (A.U.)	β (A.U.)	$C(\tau)/C(0)$ [1-exp(-Ω_{LD50})]	95% CI	p-value
Bone	0.77	(0.47,1.07)	-4.18 ± 1.09	5.41 ± 2.23	0.54	(0.37,0.66)	0.03
Brain	1.10	(0.92,1.27)	-3.20 ± 0.50	2.91 ± 0.72	0.67	(0.60,0.72)	<0.001
Liver	0.85	(0.62,1.08)	-6.40 ± 1.05	7.56 ± 2.11	0.57	(0.46,0.66)	0.01
Protate	0.97	(0.83,1.11)	-3.50 ± 0.60	3.61 ± 0.95	0.62	(0.56,0.67)	<0.001
Kidney	1.07	(0.92,1.22)	-2.73 ± 0.35	2.55 ± 0.52	0.66	(0.60,0.70)	<0.001
Combined	1.01	(0.94,1.08)	-3.26 ± 0.25	3.24 ± 0.37	0.64	(0.61,0.66)	<0.0001

The dose threshold of $\Omega=1.0$ was within the 95% confidence interval for each tissue. $C(\tau)/C(0)$ represents the fraction of cells that are damaged. The p-values calculated from the logit fit shown that the fits were statistically significant in each case.

113

As an example of the signal change in lipid tissue, the R_2* values and signal amplitudes of water and each lipid in bone marrow were plotted along with the Arrhenius rate estimate for irreversible tissue damage as a function of temperature in Figure 5-7. The slope between 17 °C and 54 °C was 2.8 ± 0.1 %/°C (R^2=0.965). At 54 °C and above, the slope was -1.6 ± 0.2 %/°C (R^2=0.917). Each of these slopes were statistically different from one another (p<0.0001). For bulk and terminal methylene there is an asymptotic decrease in R_2* until Ω approached unity. There was also a change in the methyl R_2* slope as Ω approached unity. In the amplitude measurements, a shift in the slope can be observed in the water peak. At temperatures where Ω <1, the slope was 0.4 ± 0.1 %/°C (R^2=0.824). At temperatures where Ω ≥1, the slope was -1.0 ± 0.2 %/°C (R^2=0.905). In the lipid peaks, the temperature response reduced in the bulk methylene, terminal methylene and methyl peaks by 75%, 88% and 80%, respectively, at the same temperature region.
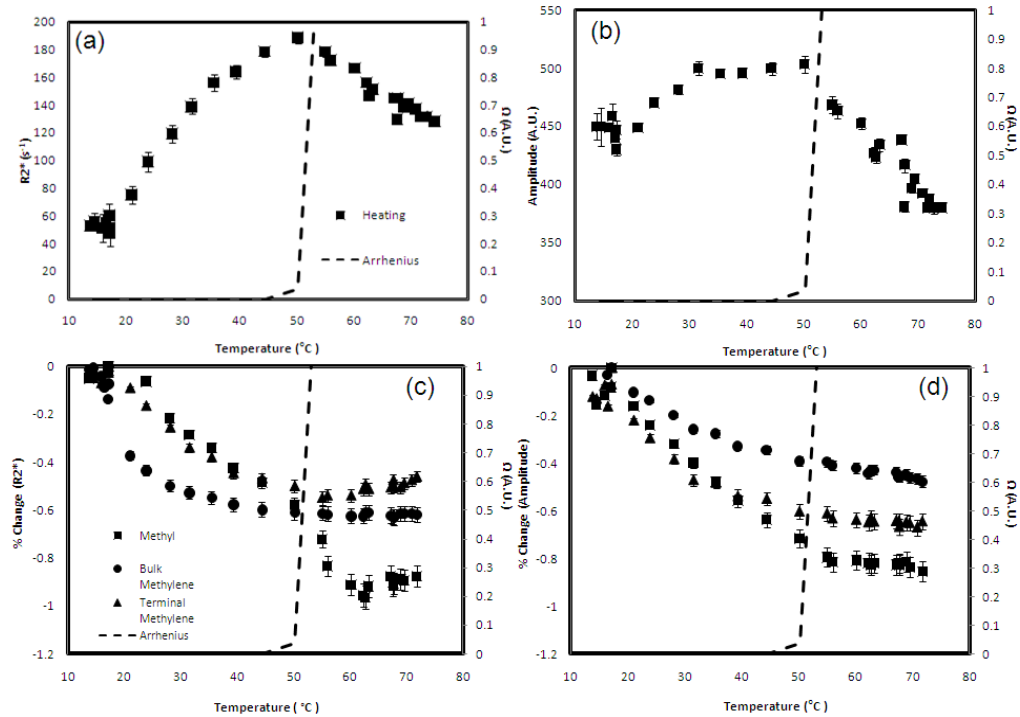
Figure 5-7 Temperature response water R_2* (a) and amplitude (b) as well as the lipid R_2* (c) and amplitude (d) of bone marrow at 3.0T

The dashed line in each plot represents the Arrhenius dose model calculation (A: 3.1 x 10^{98} s^{-1}, E$_a$: 6.3 x 10^5 J mol^{-1}) (25). Changes in the slope can be seen when the Arrhenius dose, Ω, approaches 1.0, which signifies damage to the tissue.

Figure 5-8 demonstrates what was typically seen in non-lipid tissue. This is a case from brain tissue. Table 5-8 lists temperatures where the break points occurred according to Arrhenius rate model analysis along with the slopes between these temperatures. In all tissues except prostate, there was a statistically significant (p<0.0001) change in the R_2* slope when damage is predicted to occur. This was more evident when compared to the amplitude slopes.

115
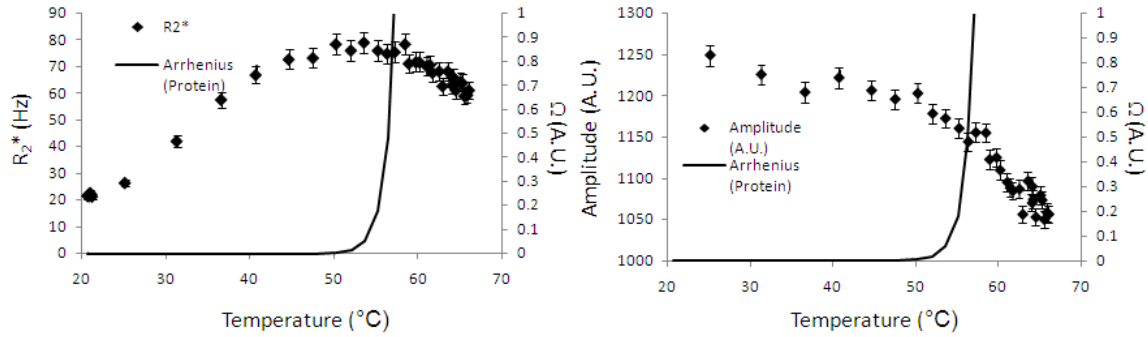
Figure 5-8 The water R_2^* (a) and amplitude (b) temperature response of brain tissue at 3.0T

As with the bone marrow, changes in slope can be seen when Ω approaches 1.0. The break points in the parameters were seen at 57.1 ± 1.2 °C. This corresponds to temperatures where phase changes are seen in the protein state.

Table 5-8 Temperature break points ($\Omega \geq 1$) with linear regression slopes above/below these points.

| Tissue	Temperature at Ω=1	R_2^* Slope (%/°C) 37° to Break Point (BP)	Above BP	Amplitude (%/°C) 37 °C to BP	Above BP
Bone	54.2±1.2	2.8±0.1 %/°C (R2=0.965)	-1.6±0.2 %/°C (R2=0.917)**	0.4±0.1 %/°C (R²=0.824)	-1.0±0.2 %/°C (R2=0.905)**
Brain	57.1±1.2	5.5±0.4 %/°C (R2=0.945)	-4.3±0.6 %/°C (R2=0.792)**	-0.4±0.1 %/°C (R2=0.799)	-1.0±0.2 %/°C (R2=0.803)*
Liver	52.2±0.4	0.7±0.3 %/°C (R2=0.852)	-1.2±0.1 %/°C (R2=0.894)**	-0.8±0.3 %/°C (R2=0.874)	-0.9±0.2 %/°C (R2=0.924)
Prostate	57.0±1.0	0.2±0.1 %/°C (R2=0.872)	0.4±0.1 %/°C (R2=0.565)	-0.4±0.2 %/°C (R2=0.851)	-0.5±0.1 %/°C (R2=0.944)
Kidney	57.0±0.4	2.1±0.5 %/°C (R2=0.625)	-1.0±0.4 %/°C (R2=0.717)**	-0.7±0.3 %/°C (R2=0.823)	-0.7±0.1 %/°C (R2=0.857)

* p<0.05,** p<0.001 compared to slope before the break point

5.4.3 DISCUSSION

With this fast CSI technique, other parameters (peak-specific R_2^* ($1/T_2^*$) and T_1-W amplitude) can also be measured to provide an important opportunity to look at changes as a function of temperature. Estimated spectral parameters were evaluated as a function of the higher temperatures that would be encountered during ablative therapy delivery using the calibrated PRF shift of water-bulk methylene or water alone. It is important to note that we did not see changes in linearity in the PRF at high temperatures (see Figure 5-4), which is consistent to previous studies where high linearity was found

116

up to 80 °C (37). In this analysis, we did see changes in linearity of R_2* and amplitude data during heating (60, 72). We have previously noted significant changes in the temperature dependence of these parameters in the range where the Arrhenius rate model predicts damage (25, 26) thereby demonstrating that it could be a useful dosimetry tool. For example, when the temperature history results in $\Omega \geq 1$, there was a consistent, sharp, measureable change in the slope of the R_2* of water versus temperature.

The molecular mechanisms for these changes are not exactly clear and understanding the relationship between the dynamics and structure of proteins and the surrounding water is a current challenge (161). Possible theories to these changes due to the protein denaturation include the change in the dipolar coupling between water molecules and denatured proteins (162). Additionally, release of water in the hydration layers of the denaturing proteins may explain the decrease in R_2* (161).

Water and lipid R_2*-corrected amplitudes also exhibited similar non-linearities in the same temperature ranges as seen in Figure 5-7 and 5-8. These changes were more evident than measuring changes in the overall T_1-W signal (from the first echo of the acquisition), which has also been shown here and previously to be non-linear with temperature in this range, presumably due to irreversible protein conformation changes (72). It is important to note that these changes in slopes were seen with and without R_2* correction over physiologically relevant temperatures (37 °C and above).

Therefore, it appears that using the multiparametric spectral estimates may return information on physical tissue changes taking place, such as conformational phase

117

transitions of proteins, which directly influence the proton chemical macroenvironment and, thereby, relaxation as observed in R_2^* mapping and T_1-W signal changes. These observations warrant further investigation *in vivo* and in other tissues, particularly in the presence of heat sensitization agents which might be used to lower the therapeutic window as direct validation of protein denaturation and it may be extremely useful in the investigation of thermal approaches to ablation as well as drug delivery or enzyme activation.

Chapter 6:   Spectral Parameter Mapping with the *k*-Means Clustering Algorithm

6.1 Introduction

As seen in the previous chapter, the CSI technique accurately and precisely determines the PRF, T_2* and amplitude of each peak. These parameters can be inputs into the k-means algorithm to help distinguish peaks since each spectral peak will be differentiated by at least the PRF and the other parameters may aid in improving the sensitivity and specificity of peak identification for 2D mapping of temperature for interventions. The algorithm will be explained and parameters will be tested using a highly-controlled mathematical phantom. After suitable parameters are found, they are used in the analysis of data from several *ex vivo* and *in vivo* tissues.

6.2 Processing Strategy

First, the image is partitioned to equal-sized regions (4x4, 16x16, 32x32 voxels, etc.). In each voxel in the regions, the *primary* PRF, T_2* and amplitude values are mapped to a 3D plot where T_2* values and amplitudes are normalized. The centroid of all the points in the plot is then calculated as well as the sum of distances between the points and the centroid.   The same calculations are made again using 2 centroids via the k-means algorithm. If the sum of distances are less with the two centroids and the centroids are at distances apart where water and lipid is expected to be (3.3-3.8 ppm), then the clusters are designated water or lipid (see Figure 6-1). This process continues for each region in the image.

After the entire image is processed, the ranges of water and lipid centroids are recorded. On the frequency axis in the 3D plot, the range of PRFs is expanded by a constant, *g*, to account to regions experiencing slightly higher or lower magnetic flux densities. Each voxel is then recalculated using a 2-peak ARMA model. If both peaks fall within the PRF regions, then the spectral parameters are mapped. Expansions on T_2* and amplitude values were not utilized since these values can vary due to relative concentration of each chemical specimen. Finally, any voxel remaining was calculated with a 1-peak ARMA model with peak identification determined by the PRF and T_2* ranges described above. Figure 6-1 shows a schematic of how the algorithm works on a mathematical phantom, which is described in the next section.
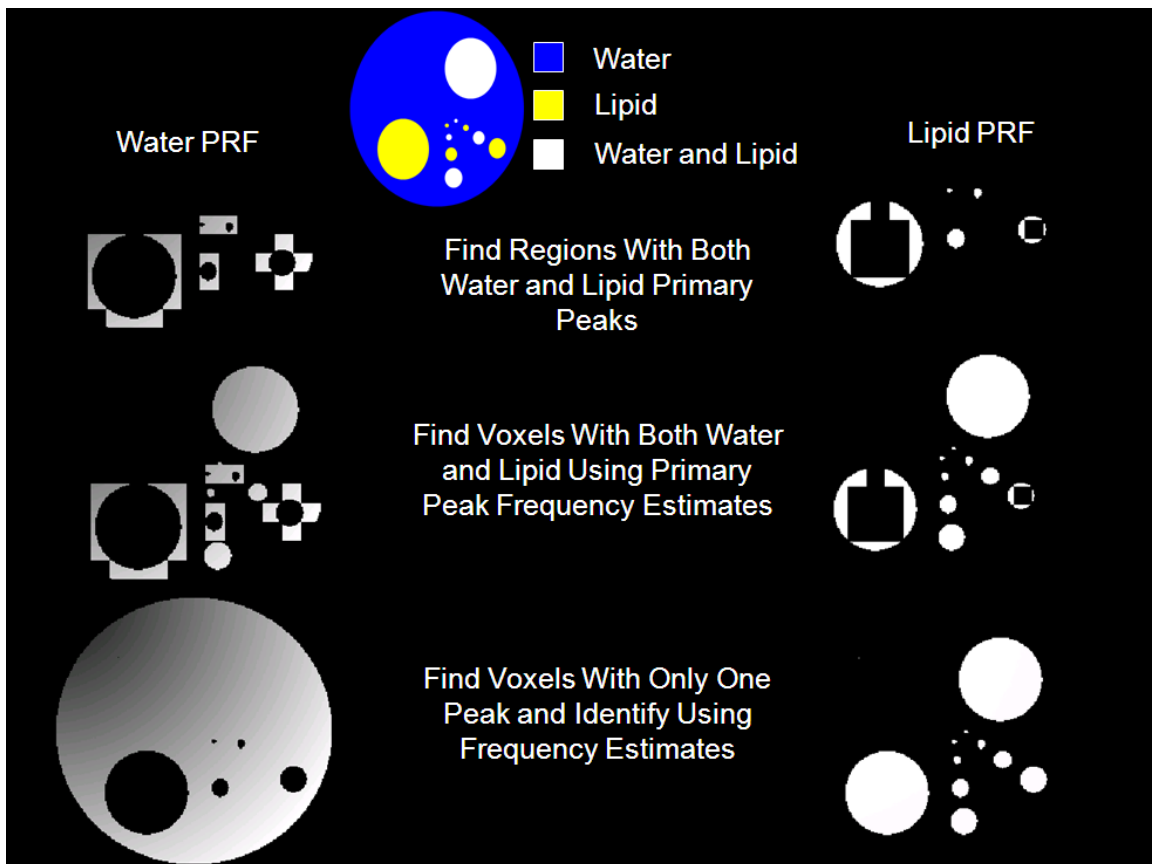
Figure 6-1 Mapping using *k*-means

The image is separated into regions. First, regions that contain both water and lipid are located. The spectral information from those areas is used to train the algorithm to look for primary and secondary peaks to create maps of each chemical specimen.
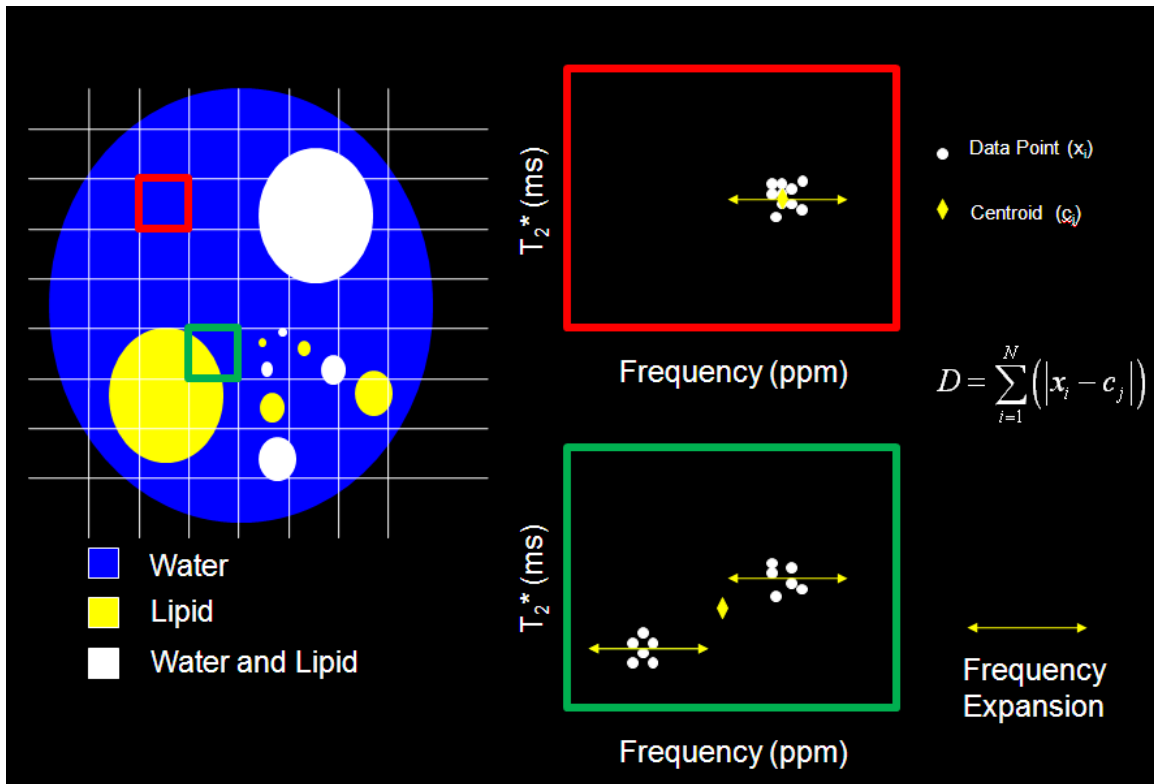
Figure 6-2 Representation of two regions analyzed by the *k*-means algorithm using the mathematical phantom – step 1

The red region represents an area with water only. The green region contains water and lipid. When the centroid is calculated from the primary peaks, the sum of distances between the data points and the centroid can aid in determining if one or two peaks are present. Frequency expansions can be added to increase the range of PRF values the algorithm will seek for primary and secondary peaks.

6.3 Testing of the CSI k-means Clustering Algorithm Using a Mathematical Phantom

6.3.1 MATERIALS AND METHODS

To test the algorithm in highly controlled conditions, a mathematical phantom was developed in MATLAB (MathWorks, Natick, MA) and is shown in Figure 6-3. In the phantom, areas of water, lipid and mixed water/lipid were created within different sized regions. Large areas of each water/lipid combinations were also created to determine how the algorithm handles large areas of only one chemical shift, which is commonly seen *in vivo*.
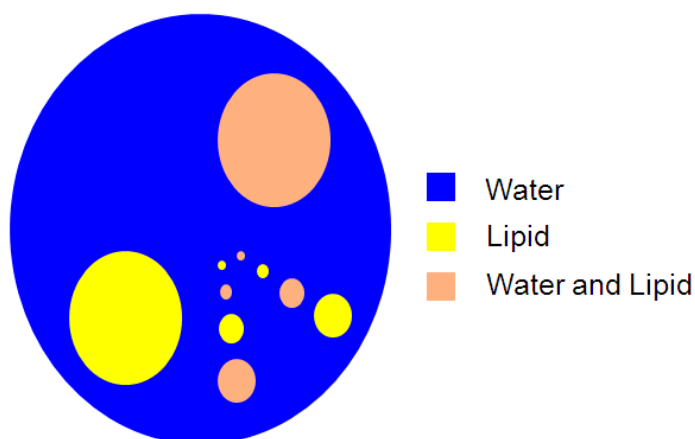
Figure 6-3 Mathematical phantom design

The phantom contains areas of water, lipid and mixed water/lipid voxels under varying sizes. The phantom was designed to work under varying areas of water and lipid.

Three metrics were used to measure the performance of the algorithm. If a peak was identified in the voxel then the voxel is counted as positive. If no peak is identified then the voxel is counted as negative. The sensitivity of identifying the correct peak was

123

defined as the true positive rate (tested positive/ true positive). Specificity was defined as the true negative rate (tested negative/ true negative). The Dice similarity coefficient (DSC) (163) was also used. Given two images, *A* and *B*, where *A* is the true image and *B* is the measured image, the DSC is the metric of how the two images overlap where

$$DSC = \frac{2|A \cap B|}{A + B}$$ (6.1)

The sensitivity, specificity, and DSC were measured as a function of field inhomogeneity across the FOV, size of the regions, expansion in the frequency axis on the 3D plots and SNR. Each mapping experiment went through 5 trials. The field inhomogeneity was incorporated into the phantom spatially by multiplying the signal by a complex exponential that smoothly varied as a function of position on the x-y plane. The field inhomogeneity was measured from 0.2 to 4.0 ppm. Region sizes by powers of 2 (4, 8, 16, 32, 64, 128) were measured at a field inhomogeneity of 1.13 ppm and a frequency expansion of 0.1 ppm. Frequency expansions up to 1.0 ppm were evaluated at the same SNR at a 1.13 ppm field inhomogeneity. When suitable frequency expansions and region sized were determined, the sensitivity, specificity and DSC were measured as a function of SNR.

6.3.2 RESULTS

Figure 6-4 displays the sensitivity, specificity, and DSC as a function of field inhomogeneity across the entire FOV for the water and lipid maps. The specificity and

DSC for water and lipid was greater than 0.999 up to a field inhomogeneity of 1.42 ppm.

Sensitivity measurements for the water and lipid maps were above 0.999 up to 2.83 ppm.
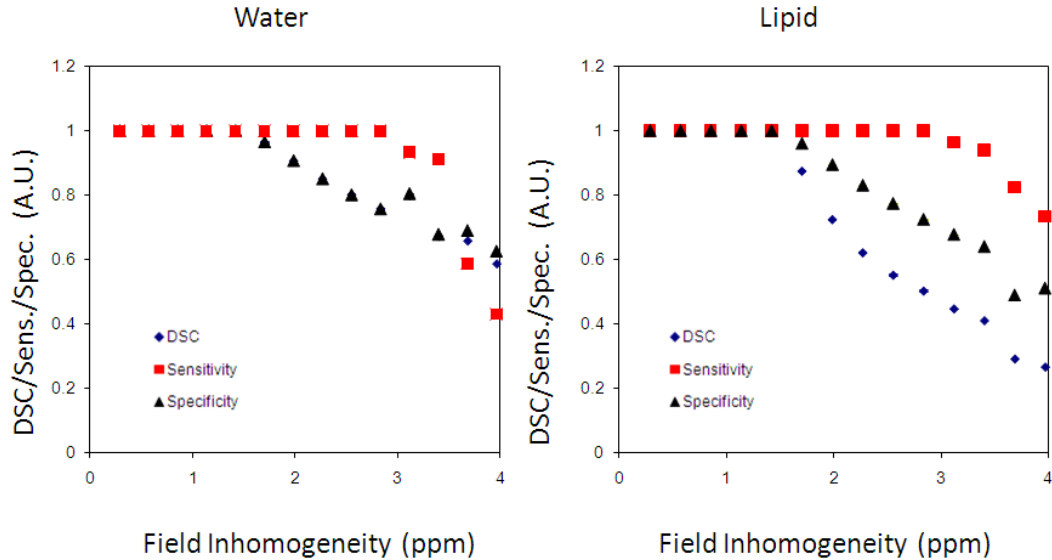
Figure 6-4 Sensitivity, specificity and DSC results as a function of field inhomogeneity

Both water and lipid maps maintained high sensitivity (>0.999) up to a field inhomogeneity in the FOV to 2.83 ppm. Specificity and DSC values for each peak were at the same high values to 1.42 ppm. Each measurement decreased at higher field inhomogeneities. Error bars were on the order of 0.001 so they were not shown on the figure.

The size of the regions used in algorithm appears to have an effect on the sensitivity, specificity and DSC. Figure 6-5 shows the values for water and lipid as a function of region sizes. As seen in this figure, sizes between 8x8 to 16x16 maintained high sensitivity, specificity and DSC values. Under 8x8 voxels, errors occurred in the k-means algorithm due to a low number of data points.

125
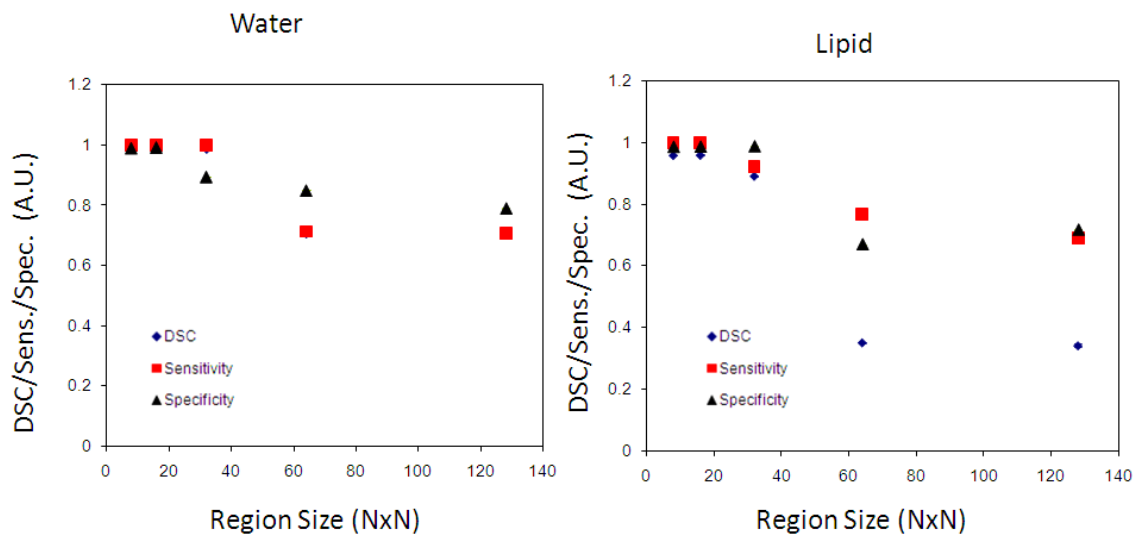
Figure 6-5 Sensitivity, specificity and DSC results as a function of region size

High sensitivity, specificity and DSC values were measured at regions sizes of 8x8 and 16x16. At higher region sizes each metric decreased in value. Most errors at these larger region sizes stemmed from misidentified regions of after the range of PRF values were identified. A lower number of water and lipid centroids increased the likelihood that peaks were identified due to a lower-sampled range of values. The k-means algorithm still separated out the peaks effectively as outlined in Figure 6-3. In this figure the field inhomogeneity was 1.13 ppm.

At 0.1 ppm and above, the sensitivity, specificity and DSC values of the maps were highly linear with the amount of frequency expansion allowed as shown in Figure 6-6. Using linear least-squares regression analysis, the water specificity and DSC curves were -0.0499 ± 0.0003 ppm^{-1} + 0.9984 ± 0.0018 (R^2=0.9497,) and -0.0061 ± 0.0002 ppm^{-1} + 0.9998 ± 0.0007 (R^2=0.9501), respectively. The sensitivity was measured as 1.0 from 0.1 to 1.0 ppm. Interestingly, the sensitivity at ppm=0 was 0.719 ± 0.001 showing that

126

some voxels containing water were missed if no frequency expansion was used. For the

lipid maps, the specificity and DSC curve fits were -0.0778 ± 0.0005 ppm^{-1} + 0.9977 ±

0.0024 (R^2=0.9973) and -0.2067 ± 0.0008 ppm^{-1} + 0.9774 ± 0.0037 (R^2=0.9993),

respectively. From 0 to 1.0 ppm, the sensitivity of the lipid map was above 0.998 even

when there was no frequency expansion.
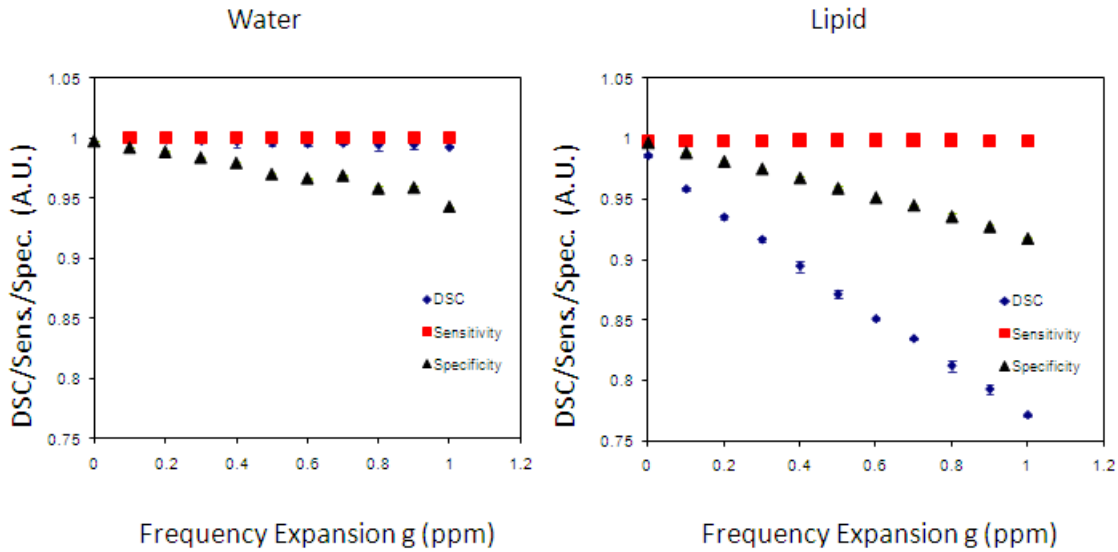
Figure 6-6 Sensitivity, specificity and DSC results with a frequency expansion in the 3D plots

Sensitivity was not affected as long as there was some expansion in the frequency axis to look for voxels

that had PRF values outside of the range the algorithm calculated in regions with water and lipid. In the

maps, if g=0, then some water voxels were missed since their PRF values lied just outside the range which

was calculated in the image. However, as g increases then the specificity and DSC decrease. In this plot,

the field inhomogeneity was 1.13 ppm with a 16x16 region size.

Figure 6-7 shows the sensitivity, specificity and DSC as a function of SNR. As SNR increases, each metric asymptotically approached 1.0. At SNR≥10, each parameter was at 0.95 or above. For mapping of two chemical shifts, a SNR of 10 and above should produce high sensitivity and specificity. For this plot, there was a field inhomogeneity of 1.13 ppm with a 0.1 ppm frequency expansion.
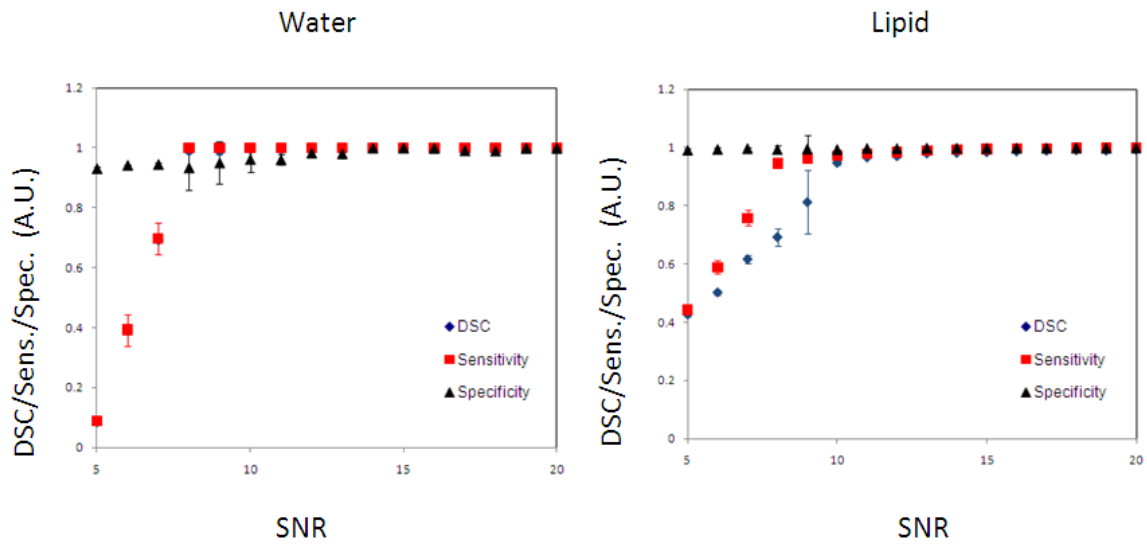
Figure 6-7 Sensitivity, specificity and DSC results at low SNR

The DSC values and sensitivity of the mapping algorithm asymptotically approached 1.0 at a SNR of approximately 10. Specificity was high even at low SNR of 5. SNR values of 10 and above are sufficient for sensitive and specific mapping under moderate field inhomogeneity (~1.0 ppm).

Table 6-1 summarizes how each parameter affects the sensitivity, specificity and DSC of the mapping algorithm. It can be noted that each parameter, with the exception of the frequency expansion, approaches unity as the limit approaches zero (field inhomogeneity, region size) or infinity (SNR).

Table 6-1 Parameter dependence on the algorithm's sensitivity, specificity and DSC

Parameter	Change	Sensitivity	Specificity	DSC
Field Inhomogeneity	↑	↔ then ↓	↔ then ↓	↔ then ↓
Region Size	↑	↔ then ↓	↔ then ↓	↔ then ↓
Freq. Expansion	↑	↔	↓	↓
SNR	↑	↑ then ↔	↑ then ↔	↑ then ↔

Most parameters showed an asymptotic behavior toward unity as the parameter approached zero or infinity. Generally, a low field inhomogeneity, region size and frequency expansion with high SNR is near-optimal conditions for the k-means mapping algorithm.

6.4 Demonstration of the k-means Mapping Algorithm in an In Vivo Swine Liver Model

6.4.1 MATERIALS AND METHODS

To test this algorithm with a near-realistic clinical scenario of a liver ablation, the MGE acquisition was utilized on swine being examined in a MR protocol study. The animals used in this study were handled in accordance with the Institutional Animal Care and Use Committee. For each pig, three axial slices were obtained through the liver (16-echoes, $TR/TE_0/ESP=500/1.8/3.0$ ms, flip angle=45/ , receiver bandwidth = 244 Hz/pixel, acquisition matrix = 128 x 128, acceleration factor = 2, voxel size = 1.6 x 1.6 x 4.0 mm^3, acquisition time = 32 s).

Based on our simulation results, region sizes of 16x16 voxels were used with a frequency expansion of 0.1 ppm. The PRF, T_2* and amplitude were all input parameters for the k-means cluster analysis. Images where then qualitatively compared to lipid-water images generated using a two-point, region growing, Dixon technique (FSPGR, 2-echoes, TR/TE$_1$/TE$_2$=175/1.8/4.3 ms, flip angle=80/ , receiver bandwidth = 244 Hz/pixel, acquisition matrix = 256 x 224, acceleration factor = 2, voxel size = 1.3 x 1.3 x 8.0 mm^3, acquisition time = 22.4 s/image) (135). Note that there was a difference in spatial resolution between this technique and two-point Dixon technique which made direct, quantitative, voxel by voxel comparisons difficult to ascertain. There was also breathing between the two acquisitions which also makes voxel-based comparisons difficult. Therefore, the generated images were qualitatively examined based on accurate mapping of known lipid-water tissues as well as the algorithms performance as predicted by simulations.

6.4.2 *RESULTS*

Figure 6-9 displays images processed by our technique with comparison to the Dixon-processed images. PRF, T_2* and amplitude maps were created of water and lipid (bulk methylene). Note that the Dixon technique identified intra-peritoneal organs (liver, stomach, spleen) as lipid. Using the MGE acquisition incorporated with the SM and k-means algorithms the organs were correctly mapped into the water image. One error seen in our mapping routine is an area of susceptibility on the anterior portion of the spleen. Figure 6-10 displays an axial slice where the k-means algorithm and Dixon technique

130

matches well. Motion between the two scans limited the ability for quantitative comparison on a voxel-by-voxel basis.
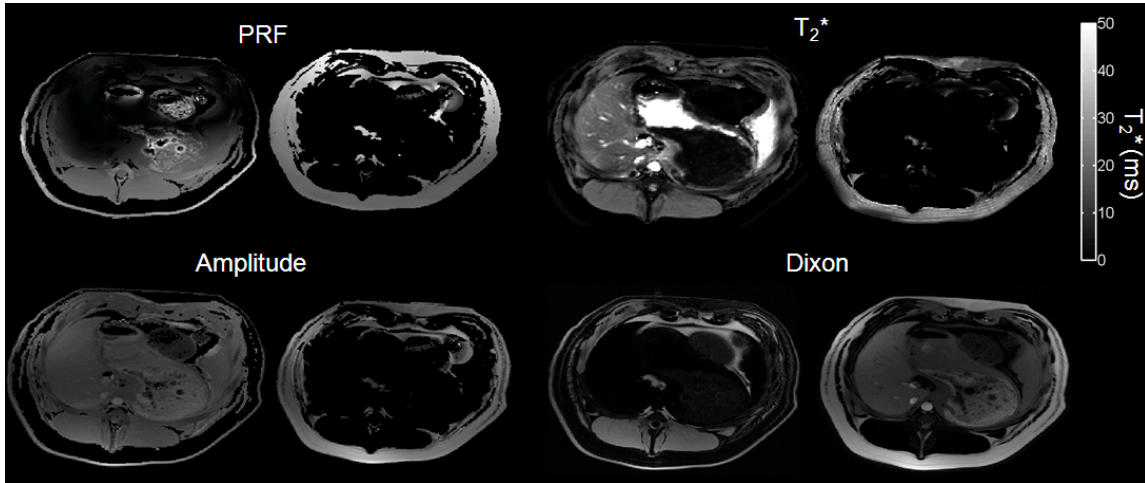
Figure 6-8 CSI mapping in porcine *in vivo* with artifact in Dixon imaging

PRF, T_2* and amplitude maps of lipid and water were created using the MGE acquisition with the SM and k-means algorithm. In addition, a Dixon-based method using a robust region-growing algorithm is shown (135). In this axial slice, the liver, spleen and stomach were mapped to the lipid image. The k-means algorithm correctly mapped these organs to the appropriate water image. Three slices were collected and the Dixon technique mapped the organs to the appropriate map as did the k-means algorithm.
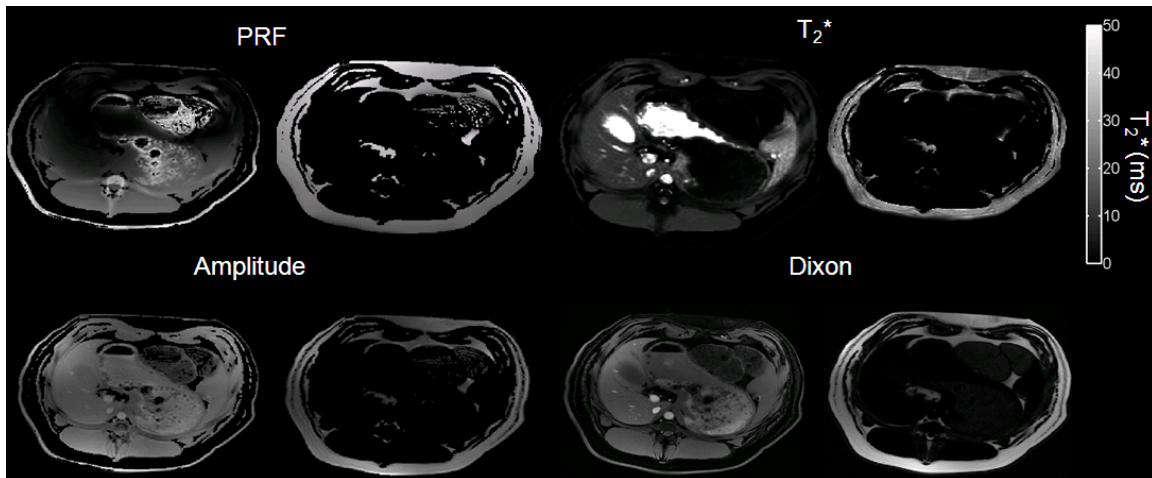
Figure 6-9 CSI mapping in porcine *in vivo*

PRF, T_2* and amplitude maps of lipid and water using the MGE acquisition with the SM and k-means algorithm in addition to Dixon-based lipid-water images. Qualitatively, there is good agreement between the two types of processing paradigms. Quantitative voxel-based measurements using Dixon as the true standard was not possible due to respiratory-based motion between the scans. Some errors can be seen in the k-means approach inside the stomach presumably due to low SNR.

Figure 6-10 presents an example where our simulations predicted lower specificity and DSC due to field inhomogeneity, which led to the misidentification of liver tissue as lipid. At the interface between the liver and subcutaneous tissue there was a measured field inhomogeneity of approximately 1.8 ppm. As seen in Figure 6-5, there should be lower specificity (*i.e.*, fewer true negatives) in the water map, which is seen in Figure 6-10. From the errors introduced from this field inhomogeneity areas with similar magnetic flux densities as liver (*i.e.*, skin) was also incorrectly mapped as lipid. This shows that although efficient mapping is possible, certain conditions can affect the efficacy of the algorithm.

132
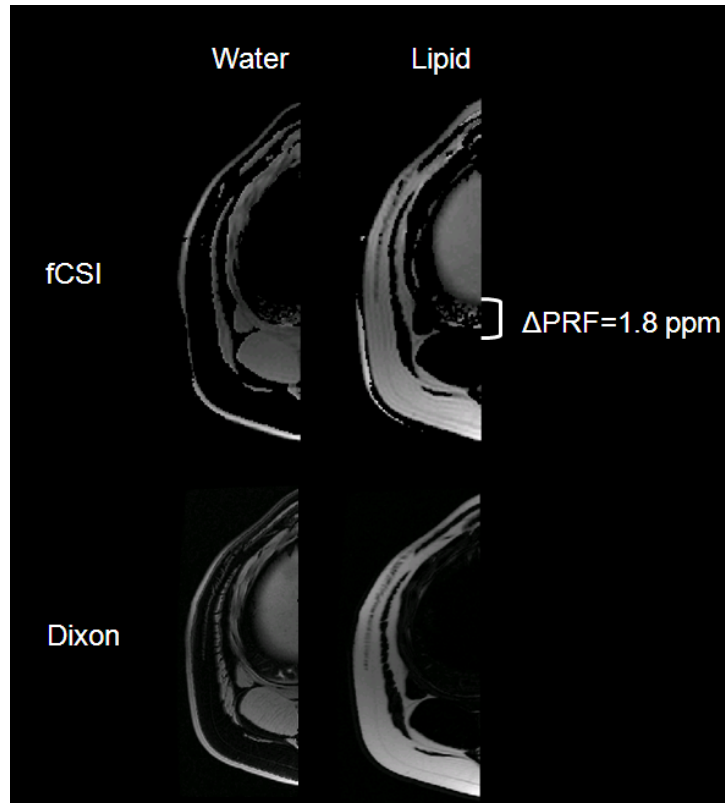
Figure 6-10 Effects of high field inhomogeneity *in vivo*

A 1.8 ppm field shift was measured between the liver and muscle just posterior to the liver. This inhomogeneity caused lower specificity between distinguishing water and lipid in CSI images as predicted by our simulation. The Dixon method correctly identified the liver as water-based tissue in contrast to Figure 6-8.

6.5 Demonstration of Thermal Therapy in Brain In Vivo

6.5.1 MATERIALS AND METHODS

We examined the feasibility of using the multi-parametric nature of the technique for guiding MR thermal therapy interventions in a large animal model by using the MGE acquisition to guide the application of laser induced thermal therapy in a canine brain *in vivo* using a 1.5T scanner. The animal used in this experiment was handled in accordance with Institutional Animal Care and Use Committee requirements. A water-cooled applicator containing a laser fiber (Biotex Inc., Houston, TX) with a 1-cm diffusing tip (808 nm) was inserted into the right hemisphere of the canine brain using MR guidance. Treatment was delivered using an exposure of 3.5 W/cm^2 for 180 seconds under continuous MGE monitoring (16-echoes, TR/TE$_0$=69 ms/2.1 ms, flip angle=30/ , receiver bandwidth = 244 Hz/pixel, acquisition matrix = 128 x 128, acceleration factor = 2, voxel size = 1.6 x 1.6 x 4.0 mm^3, acquisition time = 4.4 s/image). The ESP was 3.3 ms, giving a spectral bandwidth of 303 Hz. Using the PRF map from the SM algorithm, the shift in the PRF was measured to detect temperature changes (37) using a temperature sensitivity of -0.0098 ppm/°C (157). In addition, T$_2$* maps and T$_2$*-corrected T$_1$-W images (signal extrapolated to TE=0 ms) were created from the data and analyzed to demonstrate the potential usefulness.

6.5.2 RESULTS

The MGE acquisition (ETL=16) with SM algorithm processing was applied to monitor a laser-induced thermal therapy in canine brain *in vivo*. Figure 7(a) shows the

water proton field map, which is the source of the temperature images, and Figigure 7(b) displays the temperature map. The SM algorithm calculated the noise in the temperature map as 0.34 ± 0.09 °C in an unheated region contralateral to the therapy site. This is in excellent agreement with the calculated CRLB (SNR=39.5, T_2*=42.0 ms) of 0.35 °C. Using the CPD of a single echo from the same acquisition at TE= T_2* (which is the optimal value for CPD), the uncertainty approximately doubled to 0.69 ± 0.18 °C (p<0.01 when compared to CSI). Unlike the CPD technique, the sensitivity of the CSI technique is inherently driven by the SNR of the acquisition and is independent of the echo-time used (apart from the impact on SNR). Figure 7(d) is the T_1-W image, corrected for T_2* decay from our knowledge of the T_2*, which was also calculated at each time point. During treatment delivery, an anomalous artifact arose in the temperature images that correlated with a hyperintense area seen near the laser source on the T_1-W images. This was suspicious for an acute hemorrhage induced by the treatment. The suspected hemorrhage was confirmed by a post-treatment T_1-W SPGR acquisition [Figure 7(e)]. An image of the calculated T_2* for water [Figure 7(c)] shows a clearly hypointense lesion.
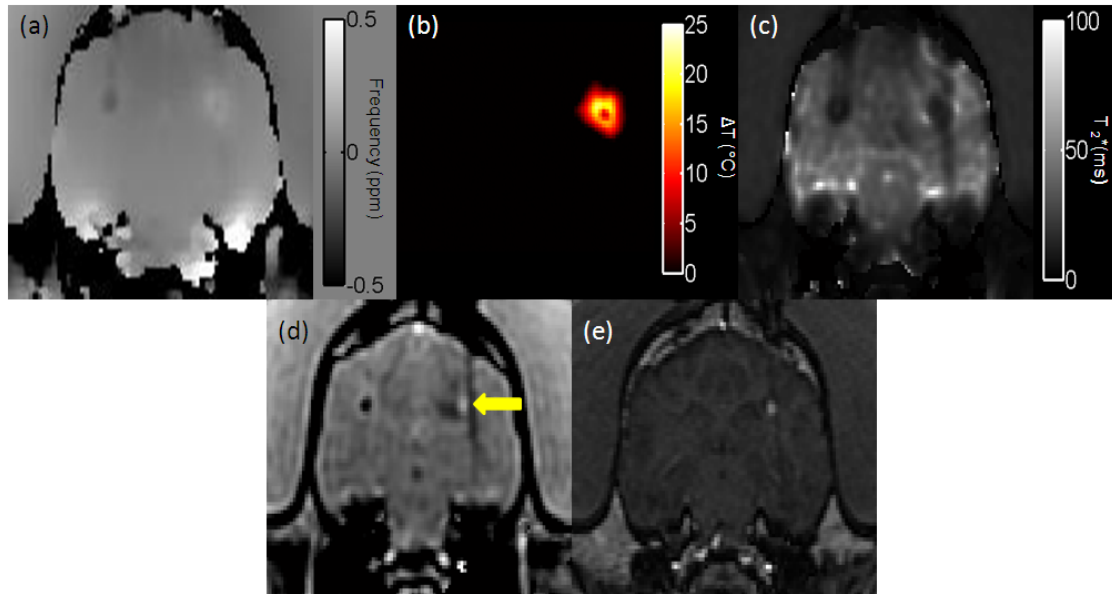
Figure 6-11 Multi-parametric monitoring in LITT in canine brain *in vivo*

The water PRF map of a canine brain used to create the temperature maps had a temperature sensitivity coefficient of -0.0098 ppm/°C (a). The temperature map for the thermal therapy in the canine brain (b). The noise calculated in an unheated region contralateral to the therapy site was 0.34 ± 0.09 °C. Using CPD at TE=T_2*, the uncertainty increased to a mean of 0.69 ± 0.18 °C. A T_2* map generated by the SM algorithm (c). The T_1-W images with T_2* correction simultaneously calculated at each acquisition along with the temperature maps (d). During treatment, a hyperintense area developed near the laser source, raising the suspicion of a treatment-induced hemorrhage (indicated by an arrow). The hyperintense lesion, clearly shown on (c), was confirmed as a treatment-induced hemorrhage on a posttreatment T_1-W SPGR acquisition (e). Reprinted with permission from the American Association of Physicists in Medicine, (150).

6.6 Demonstration of Thermal Therapy in Prostate In Vivo

6.6.1 MATERIALS AND METHODS

Laser-induced thermal therapy was performed in a canine prostate *in vivo*. As with previous experiment, this experiment was approved by the Institutional Animal Care and Use Committee. Two water-cooled interstitial lasers tuned to 980 nm (Biotex Inc., Houston, TX) were placed into the prostate from the anterior surface of the canine. The anesthetized animal was placed in a 1.5T clinical scanner with a 12-channel torso coil. Treatment was delivered under continuous MGE monitoring (16-echoes, TR/TE$_0$=69 ms/2.1 ms, flip angle=30/ , receiver bandwidth = 244 Hz/pixel, acquisition matrix = 128 x 128, acceleration factor = 2, voxel size = 1.9 x 1.9 x 4.0 mm^3, acquisition time = 4.4 s/image). The ESP was 3.2 ms. The SM and k-means algorithms were used to identify water and bulk methylene peaks to create temperature maps. The precision of the temperature estimates were recorded using the CSI and CPD techniques (TE=24.5 ms). The mean time it took to process one acquisition was also recorded.

6.6.2 RESULTS

Using the *k*-means algorithm with the parameters found in the mathematical phantom analysis, lipid and water was adequately separated. No lipid was found in the prostate itself so the differences in the water PRF map were multiplied by -0.0097 ppm/°C to calculate temperature. Using CSI, the uncertainty in the temperature map was 0.7 ± 0.2 °C whereas the CPD uncertainty was measured at 1.4 ± 0.3 °C (p=0.02). The time to process one acquisition was 33.2 ± 5.2 seconds.
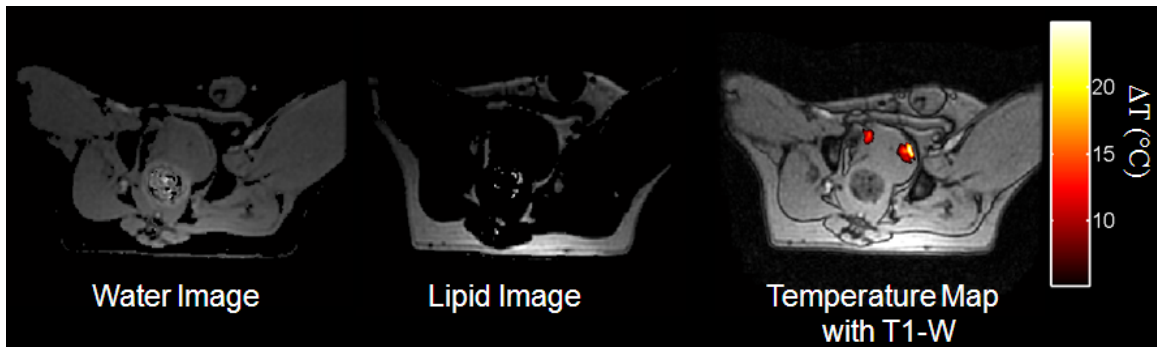
Figure 6-12 Water, lipid and temperature maps in canine *in vivo*

Water and lipid were separated which some error in the rectum due to susceptibility (air/tissue interfaces) and low SNR. The temperature maps were created using the difference of the water PRF map. The noise in the CSI maps was roughly half of what was seen in CPD (0.7 ± 0.2 °C for CSI and 1.4 ± 0.3 °C for CPD (p=0.02)).

6.7   *Regional CSI for Real-Time Mapping*

6.7.1   *MATERIALS AND METHODS*

To increase the temporal resolution while using computer processors which would make the processing easily accessible, a user-defined regional *k*-means algorithm was created. The parameters and code is the same as in the full FOV algorithm. However, with this algorithm the user defines a ROI to process that region alone. Note that in interventions we are usually focused only on the area of intervention.

The algorithm was tested on *ex vivo* bone marrow tissue as well as *in vivo* prostate. These tissues represent some of the more difficult areas to map due to heterogeneous lipid and water content. Mapping was done using data from laser-induced thermal treatments on *ex vivo* bone which was previously described in section 5.3.1. The difference between the fluoroptic probe readings and CSI or CPD readings were also

138

measured. Temperature was calculated using bulk methylene as an internal reference (-0.0087 ppm/°C).

In another canine, treatment was delivered using an endorectal high-intensity focused ultrasound (HIFU) device (Insightec, Inc., Hefei, Isreal). Again, in a 1.5T scanner, monitoring was done under continuous MGE acquisitions (16-echoes, TR/TE$_0$=69 ms/1.9 ms, flip angle=30/ , receiver bandwidth = 244 Hz/pixel, acquisition matrix = 128 x 128, acceleration factor = 2, voxel size = 1.9 x 1.9 x 5.0 mm^3, acquisition time = 4.4 s/image). In order to run in real-time, the SM and k-means algorithms were adapted where processing could be performed in real-time ($\leq$ 5 secs) by allowing the user to define a ROI to make the maps. Water and lipid PRF maps were created in a region encompassing the prostate and times to process were recorded.

6.7.2 RESULTS

Figure 6-13 shows the mapping in a small ROI around the heating region in bone. Note that water and lipid were detected throughout the marrow parenchyma. There was a low area of SNR due to the laser fiber placement which accounts for the voxels being absent in the center of the images. A fluoroptic probe was in this specimen. The RMSE, using the fluoroptic probe measurement as the true measurement, was 0.54 ± 0.13 °C for CSI and 1.75 ± 0.42 °C for CPD (p=0.04). The uncertainty was measured as 0.68 ± 0.09 °C using bulk methylene as an internal reference and the uncertainty was 1.98 ± 0.18 °C (p<0.01). The time to process one acquisition was greatly reduced compared to full FOV processing at 4.3 ± 0.2 seconds, which is adequate for real-time guidance.
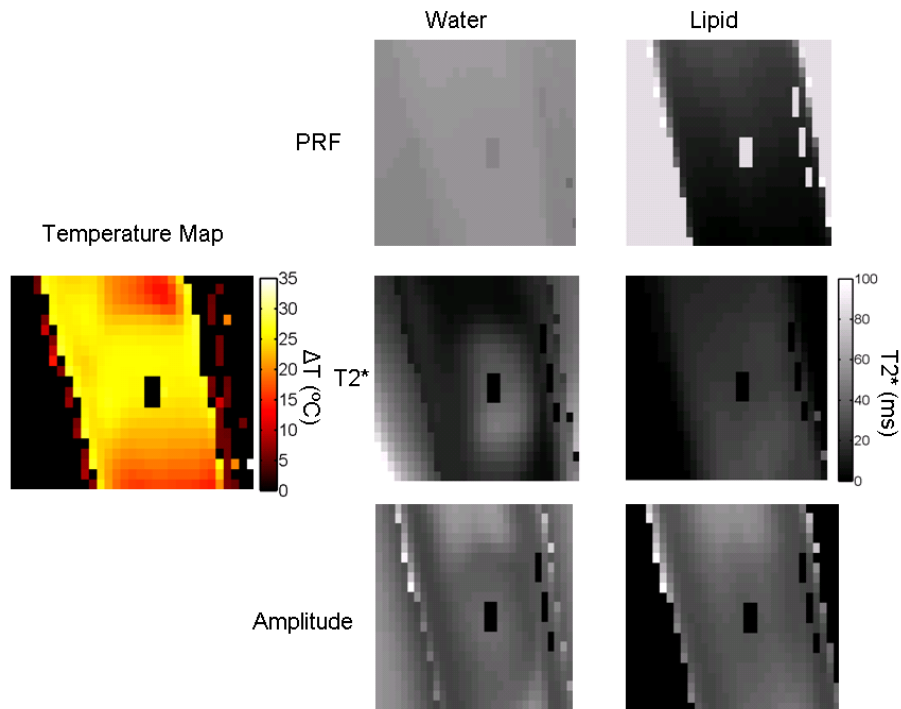
Figure 6-13 Water, lipid and temperature maps in canine bone marrow *ex vivo*

Water and lipid were separated in the bone marrow. The temperature maps were created using bulk methylene as an internal reference. As seen in the measurements in chapter 5, the RMSE was lower in CSI (0.54 ± 0.13 °C for CSI and 1.75 ± 0.42 °C for CPD (p=0.04)).

Areas of water, lipid and mixed voxels were seen in the *in vivo* prostate images analyzed by the regional CSI algorithm. As with the bone, image processing time was rapid at 4.7 ± 0.5 seconds per acquisition. Figure 6-14 shows the water and lipid PRF maps as well as a map of where water and lipid is both present. For verification, a FFT of voxels in each area were processed to confirm that there as indeed water and/or lipid peaks in those areas.
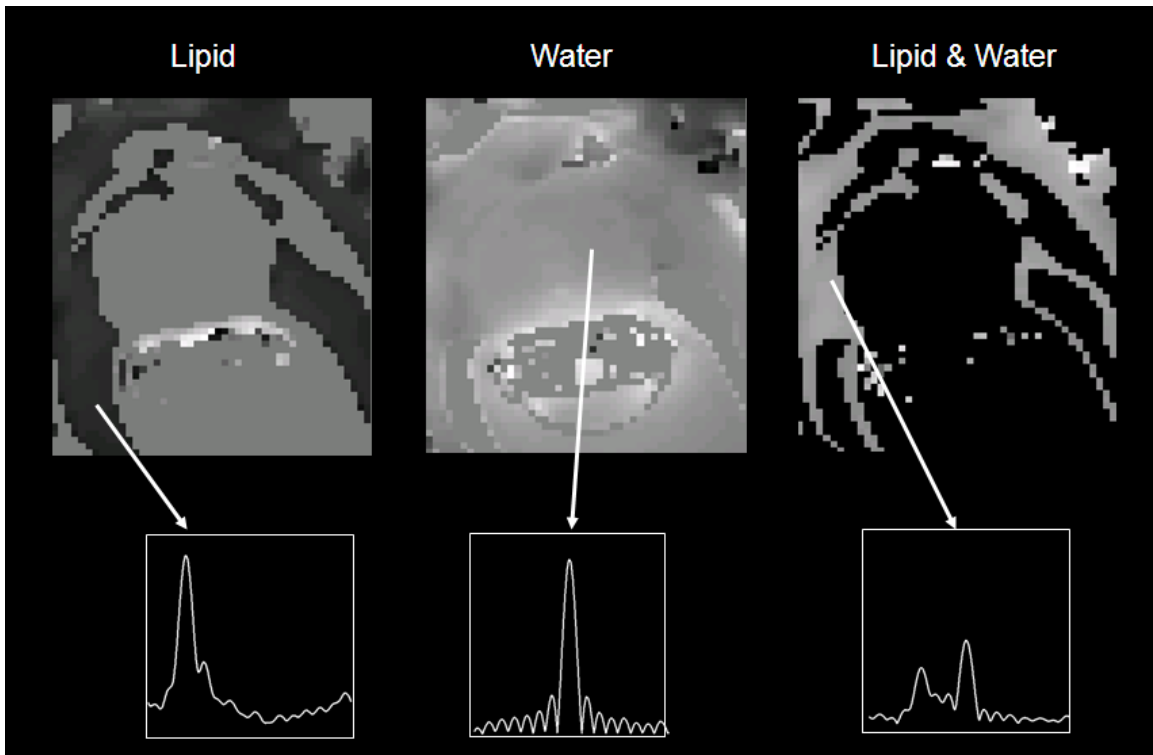
Figure 6-14 Water and lipid PRF maps in canine prostate *in vivo*

Areas of water and lipid were identified and confirmed by processing spectra manually in each area. One

area of error found was in the rectal area under the prostate which is an area of low SNR.

6.8   Discussion

The primary aim of the research described in this section was to take advantage of the wealth of multi-parametric data in order to provide robust mapping without requiring certain constraints (*i.e.*, constant chemical shift between lipid and water, equivalent T_2* between chemical shifts) which can affect the accuracy and precision of temperature mapping.

In the post-processing of many CSI acquisitions, assumptions are made in order to map a certain parameter. For example, in Dixon methods in addition to IDEAL (see section 3.4) there is typically an assumption that the chemical shift between water and lipid is constant. This is used in order to image the amplitude to either look at water-only images or calculate the fraction of lipid in the image. In PRF-based temperature imaging, the assumption of a constant chemical shift difference between water and lipid does not hold since the water PRF shifts with temperature. This shift, particularly at high temperatures, can lead to errors in the image separation. In addition, field maps are typically generated, which have been used to estimate temperature changes. This, however, does not give an independent map of the lipid field in order to correct for susceptibility, field drift and motion.

The choice of the k-means algorithm for mapping is multi-faceted. In addition to its known robustness in segmenting data it is computationally inexpensive, which is important since this needs to be implemented in near-real time for MR interventional procedures. It can be parallelized in order to decrease the processing time. The regional

142

processing method presented can also be implemented since in interventional procedures the site of the intervention is the primary point of interest and not the entire image.

The purpose of the mathematical phantom studies was to provide a highly-controlled setup in order to test the performance of the algorithm. From these simulations, we were able to choose appropriate parameters, such as PRF ranges and region sizes, to increase the sensitivity and specificity of the technique. Also, it was very useful to determine extrinsic (algorithm-based) and intrinsic (subject-based (SNR, inhomogeneity) parameters to show when the algorithm will fail. As an example, Figure 6-11 showed a misidentification of liver tissue as lipid. This was caused by field inhomogeneties which were shown to have lower specificity as seen in Figure 6-4. In this case, the large field inhomogeneity was highly localized to areas around the liver, which will make it difficult to properly map. In situations with field inhomogeneities across the FOV, the image can easily be separated into 2-4 images in which each image will presumably have a lower field inhomogeneity. This should work as long as lipid and water is present in each section of the image.

Our *in vivo* data in the canine brain highlight some of the potential advantages of multi-parametric monitoring for thermal therapy procedures because both physiologic (temperature) and anatomic (T_1-W, T_2* maps) information are available. In this case, a treatment-induced hemorrhage was monitored during treatment. In CPD techniques, the optimal echo time is given by the T_2* of the signal (38). Magnitude images are, therefore, contaminated by the T_2*-weighting of the signal ($\exp(-TE/T_2^*)$) which can

143

obscure T_1 changes in the image. This would make it difficult to observe the hemorrhage and, more importantly, determine when it occurred during treatment. The T_2* correction with this technique allowed us to view a T_1-W image at effectively TE=0, which, in this case, allowed visualization of hyperintensity that was not seen on the magnitude images at TE=T_2*. This example shows that this technique can be performed *in vivo* and shows increased precision compared to CPD. Accuracy in each *in vivo* experiment could not be measured due to the lack of an invasive temperature probe in the heated region.

One of the challenging areas in which to map the PRF is in bone marrow. Figure 6-13 demonstrates the ability to accurately and precisely measure the temperature in these areas. Currently, CPD-based MRTI is a challenge due to heavy lipid content. As seen in the PRF calibrations, this CSI technique is particularly useful in lipid-containing tissues in addition to tissues with no lipid, such as brain and kidney. The method is also useful to map lipid around the prostate, which may be used to approximate the field in the prostate.

Chapter 7: Conclusions and Future Directions

7.1 Concluding Remarks

Robust spectral processing and mapping algorithms have been developed, validated and applied to a MGE acquisition in order to provide CSI-based temperature imaging at higher spatiotemporal resolutions than what was previously available. In previous techniques, the acquisition and processing strategies were limited by avoiding spectral aliasing and by collecting enough samples to implement Fourier-based analysis as seen in high spectral resolution CSI (45-47). This degrades the spatiotemporal resolution by requiring interleaved shots, especially at 3.0T, to reduce the echo-spacing. A high number of samples (32 or higher) also requires a longer acquisition time. In addition, receiver bandwidths are raised which reduces the SNR, and thus sensitivity, of the technique (45-47).

After investigating the limitations of filtered Fourier methods, we researched alternative methods to accurately and precisely determine the spectral parameters from a low number of samples that could be translated into a rapid CSI acquisition. The ARMA model was deemed as an appropriate model since, unlike Fourier techniques, accounts not only for the PRF but also relaxation and noise. By incorporating this model, PRF, T_2* and amplitudes were measured accurately and precisely over a wide range of ETL and SNR values.

Another important contribution in this investigation was the incorporation of the CRLB not only to validate the model but also to use it to theoretically determine the

sensitivity as a function of extrinsic and intrinsic acquisition parameters. Using CRLB analysis, it was found that the sensitivity depends on more parameters than what is seen in CPD techniques (equations 4.2-3). Unlike another CRLB derivation for PRF-CSI, which looks only at the precision of the temperature estimate using lipid as a reference (164), this CRLB analysis provides theoretical estimates of the PRF as well as T_2* and amplitudes for each peak in the spectra. Details on the CRLB can be found in Appendix A. In both one-peak and two-peak models, measured uncertainties in phantom, *ex vivo*, and *in vivo* tissues agreed well with what was predicted by the CRLB.

Another important finding in the ARMA approach was the remarkable precision and accuracy even when the number of peaks in the model is underestimated. This appears to be due to the analysis being performed in the *z*-domain. The information is concentrated in poles in *z*-space, as seen in Figure 7-1. When one peak is chosen for the model, the algorithm gravitates to the dominate peak thus giving an accurate estimate for that peak.
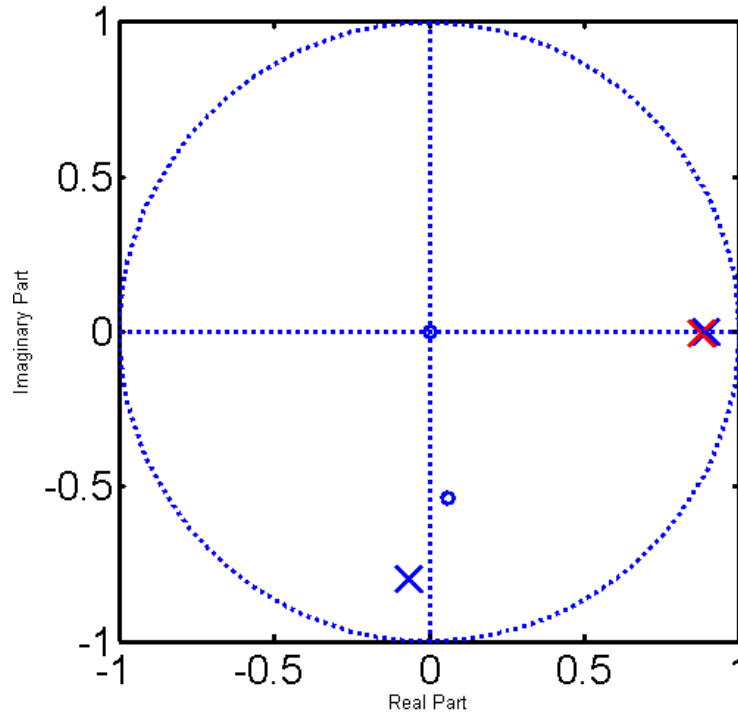
Figure 7-1 Z plot using a one and two peak ARMA model

The zeroes (o) and poles (X) for a one-peak (blue) and two-peak (red) ARMA model estimated by the SM algorithm. A two-peak model was simulated. When a one-peak model was applied to the simulated signal, the pole was calculated to be approximately where the two-peak model calculated to be.   This shows that even if the number of peaks is underestimated, the primary peaks are still calculated with high accuracy.

Overall, in terms of the first specific aim of developing, validating and characterizing via simulation a model-based spectral analysis algorithm, we found that the SM algorithm provided higher precision compared to CPD (Figure 4-16) and high precision/accuracy (<1.0 °C) over a wide range of ETL and SNR values.   This is in support of our hypothesis.

Using our CRLB analysis, we found that the SNR is directly proportional to the precision and accuracy of the spectral processing algorithm. Thus, we investigated the acquisition parameters that maintain high SNR in addition to acquisition parameters to

avoid for accomplishing the goal of accurate and precise temperature imaging. After several phantom experiments, we achieved the SNR that provided uncertainties that were predicted using our CLRB analysis as well as simulations. Thus, we showed that the MGE acquisition can provide the SNR and parameters necessary to use the ARMA model for temperature estimation, which also supports our hypothesis.

In tissues with multiple chemical shifts, it is very important to accurately identify the chemical shift in order to apply the correct, chemical shift-dependent, TSC for accurate temperature imaging. By taking advantage of the multi-parametric data, we utilized a clustering algorithm with high sensitivity and specificity while maintaining reasonable processing times for real-time implementation. This k-means algorithm has also been adapted to work with images across an entire FOV or in a smaller ROI defined by the user.

With highly sensitive and specific mapping, we were able to measure temperature changes and TSC values in a variety of phantoms and tissues. In cases where a temperature probe was used to compare between the CSI and CPD temperature estimates, the CSI method had statistically higher accuracy and precision, which supports our hypothesis.

In addition to higher precision in non-fatty tissues, an important and interesting finding was the TSC measurements when bulk methylene was used as an internal reference. If lipid is present in the tissue, the lipid susceptibility effect corrections are necessary in order to give more accurate measurements. This is an important finding

148

when CPD is used in certain organs, such as breast, bone marrow and, in some cases, liver. Basic suppression of lipid or selective excitation of water for PRF-based temperature measurements will not suppress the effects from lipid since water will still experience susceptibility from the lipid. As seen in this work, correcting for the susceptibility by using lipid as a reference provides higher accuracy and should be considered when monitoring therapies in fatty tissues.

In addition to the findings in support of our hypothesis, another important finding was discovered by measuring additional parameters calculated by the ARMA during thermal ablations. This technique provided the unique opportunity to explore changes in peak-specific T_2^* and T_1-W amplitude simultaneously with PRF-based temperature imaging at higher spatiotemporal resolutions than what was previously available. We found statistically significant changes when Arrhenius rate dose model analysis predicted thermal damage to the tissue. This could possibly be useful in verifying thermal damage in ablations during delivery. Another potential use is to measure differences in these curves in the presence of adjuvant therapies such as chemical ablations or irradiation.

Overall, through rigorous simulations and thermal treatments performed in phantoms as well as *ex vivo* tissues with CSI and CPD measurements, the increased precision and accuracy supports our hypothesis that through the use of a multi-gradient echo acquisition coupled with model-based spectral processing algorithms, CSI-based temperature maps can be generated with higher accuracy and precision compared to standard CPD techniques without sacrificing spatiotemporal resolution.

149

7.2 Future Directions

This research has opened doors for new investigations not only in thermal therapies but also in other MR applications such as image-guided chemical ablations, T_2* mapping, and dynamic contrast enhancement. In terms of thermal therapies, there are several avenues for future work. One is extrapolation of the lipid PRF map into water-only areas to help correct for susceptibility, field drift and motion. One excellent example would be in thermal treatments of the prostate. If the lipid PRF map can be fitted by a polynomial plane, it can be used as an internal reference instead of relying on the changes in the water PRF alone. This is done much the same way as referenceless thermometry is done with CPD-based temperature imaging (86, 158, 165).

Another area of research is the ability of using this technique for absolute thermometry. One unanswered question in MR temperature imaging is if the differences between water and lipid PRF values provide absolute temperature. One current problem with this is a wide variation in the PRF difference between water and lipid. Authors have cited several causes such as BOLD and J-coupling effects that affect the measurement *in vivo* (37). This leads to yet another potential area of research in mapping with more than two peaks. While the k-means algorithm used in this research focused on bulk methylene and water, the algorithm can be further investigated to higher order models to account for more peaks such as terminal methylene and methyl peaks. One possible means to accomplish this is to look for these subsequent peaks after the primary lipid peak has been identified.

In light what was seen in our multi-parametric studies, more studies need to be done *in vivo* to provide simultaneous temperature, T_2* mapping and T_1-W imaging to validate the non-linearities seen in *ex vivo* tissues. This must be correlated with histology to confirm damage as seen from the thermal dose and T_2*/T_1-W parametric imaging. The goal of this work is to see if the T_2* and/or T_1-W imaging helps validate thermal damage during the delivery and, as mentioned above, if adjuvant treatments change the T_2*/T_1-W temperature sensitivities that are correlated with damage. In addition, in some tissues a shift has been measured around 41 °C which corresponds to lipid bilayer disruption (166).

From a computational standpoint, work is still needed to improve the computing performance of the spectral processing and mapping algorithms to facilitate use in real time for interventional procedures. Theoretically, a parallel implementation on a stand-alone or portable workstation, which can be easily adapted to the MR scanner, is currently possible. For example, implementation of the algorithms on a single graphics processing unit (GPU) can, at best, achieve a speed up factor of 125 (*i.e.*, reduce the processing time by a factor of 125).

The current implementation of the codes must be thoroughly profiled to find the computing bottlenecks and the degree of parallelism inherent to this part of the current algorithms must be critically evaluated. The peak performance and speed up gains could be dramatically affected by the amount of inter-core communication needed by the

algorithm. The possibility exists that completely different algorithms may perform better on these parallel computing architectures.

Another major factor to consider is the programming language for the implementation. We currently use MATLAB (MathWorks, Natick, MA) for our spectral and image processing. Therefore, the quickest implementation would be to explore Mathwork's planned GPU support and determine if the future GPU support would be amenable to the goals of the project. As an alternative, several of the national lab code projects have begun work implementing their open source software on GPU architectures. Parallel implementation with respect to one of these code bases has several potential advantages and drawbacks. For example, one code's parallel interface hides low-level commands from the user and casting the algorithms in terms of its interface would allow future portabilty to both GPU and CPU clusters. The CPU cluster environment could also be used as a fail safe for algorithms that fail in the GPU environment. In this situation, remote visualization capabilities would have to be incorporated. It is important to note that the SM and k-means algorithms must be coded in C++ or be found in some other scientific computing library if it is to be implemented in many parallel coding structures. The development of these codes in other languages is possible and is a focus of future work.

Another application of this CSI technique is the monitoring of chemical ablations since many chemicals used in these procedures have MR-detectable chemical shifts. To demonstrate the feasibility for providing unique information for MR-guided chemical

ablations, we used the MGE acquisition (16-echoes, TR/TE_0=70 ms/2.1 ms, ESP=3.3 ms, flip angle=60/ , receiver bandwidth = 244 Hz/pixel, acquisition matrix = 128 x 128, acceleration factor = 2, voxel size = 1.6 x 1.6 x 4.0 mm^3, acquisition time = 4.5 s/image) and the ARMA modeling to monitor the injection of 2 ml ethanol in an *ex vivo* bovine liver sample. Ethanol is a agent used in interventions because it induces coagulation necrosis of tissue by protein denaturation, cellular dehydration and small vessel thrombosis (167). The location and the relative concentration of the ethanol were determined by locating the methyl (CH_3) peak versus the water peak. Changes in the chemical shift, T_2*, and amplitude of both the water peak and the ethanol-methyl peak were measured over time in a ROI.

Figure 7-2 contains the pre and post T_1-W images obtained with a fast spin echo (FSE) sequence in addition to T_1-W amplitude made from measurements taken during real-time monitoring of the percutaneous injection. Figure 7-2(a) shows the T_1-W FSE image used to localize the needle. Figure 7-2(b) displays the water amplitude image 60 seconds into the ethanol injection, while Figure 7-2(c) illustrates a map of the amplitude of the ethanol peak overlaid on a T_1-W amplitude image of water at the same time point. The region where the ethanol signal was located by the SM algorithm corresponds well with intra-treatment, T_2*-corrected, T_1-W images calculated using the measurements from the SM algorithm [Figure 7-2(b)] and the post-treatment T_1-W FSE image [Figure 5(d)]. Figure 7-2(e) illustrates the spectrum provided by our algorithm for an averaged signal over an ROI before and after the ethanol was percutaneously injected into the *ex*

vivo liver sample. The methyl (CH_3) peak from the ethanol is located 3.72 ppm away from water. Note the similar aliasing as seen with the lipid-water phantom. Figure 7-3 illustrates the observed changes in the chemical shift (a), T_2^* (b), and amplitude (c) of the untreated liver, treated liver, and the methyl peak of ethanol over time. The frequency difference between the water and methyl group had an uncertainty of 0.021 ppm. The chemical shifts in all three ROIs moved in the same direction after the injection, indicating changes from field drifts or susceptibility. The T_2^* value for ethanol steadily decreased [Fig. 7-3(b)], whereas the T_2^* of the liver tissue decreased to a value of approximately 24 ms, which is 27% lower than the value before the injection. Figure 7-3(c) shows that a 39% reduction in the T_1-W amplitude for water recovered by 16% as the ethanol diffused from the region.

Noise estimates in the liver tissue were 0.0022 ± 0.0005 ppm, 0.861 ± 0.272 ms, and 1.46 ± 0.24 % for the chemical shift, T_2^* and amplitude, respectively. The chemical shift and T_2^* noise measurements, which encompassed the calculated CRLBs at the 95% confidence level, were calculated as 0.0023 ppm for the chemical shift and 0.902 ms for T_2^*. At the measured SNR (40.0) and T_2^* (30.7 ms), the CRLB of the amplitude measurement was 0.34%. The mean amplitude noise estimates did not match the CRLB at the 95% confidence level.
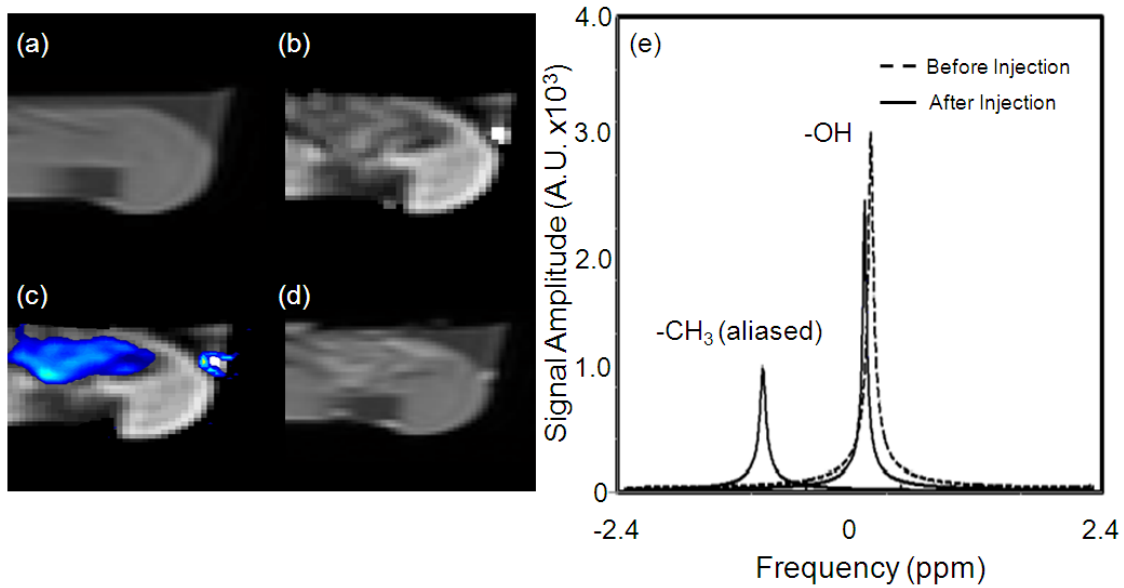
Figure 7-2 CSI monitoring of chemical injection of ethanol

T_1-W FSE acquisition used to localizing the injection needle (a). Image of the amplitude of water provided by the SM algorithm demonstrates a decrease in signal where the ethanol was injected (b). Map of the amplitude of the ethanol peak overlaid by a T_1-W image for the amplitude of water (c). The ethanol was located by detecting the presence of the methyl peak. Good correlation exists between areas of damage shown by a posttreatment T_1-W FSE acquisition (d) and measurements calculated with the SM algorithm for amplitude (b) and chemical shift (c) Spectral parameters in the liver before (dashed line) and after (solid line) the ethanol was percutaneously injected (e). Reprinted with permission from the American Association of Physicists in Medicine, (150).
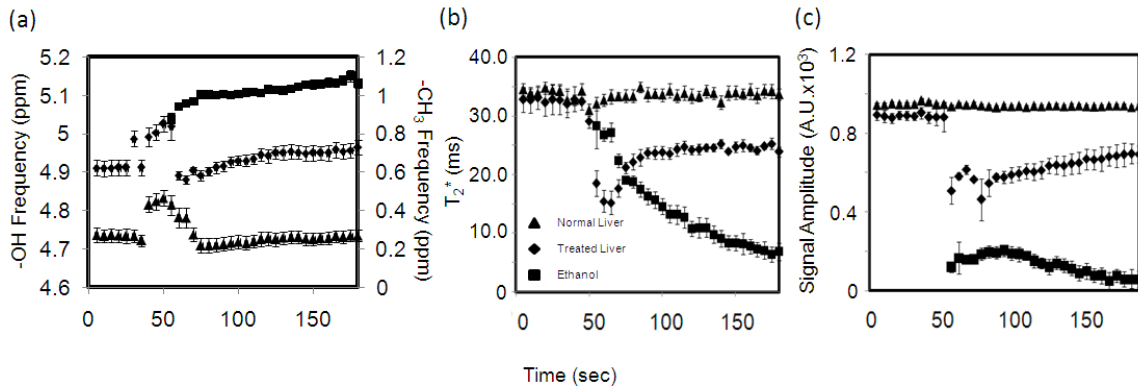
Figure 7-3   Changes in spectral parameters over time during injection of ethanol

The evolution of the chemical shift (a), T_2* (b), and amplitude (c) for water (triangles) and ethanol's methyl peak (squares) over the entire treatment time. A susceptibility shift can be seen in the water chemical shift in (a). The T_2* for water decreased by 27% after the introduction of ethanol. (b). A 39% reduction in the T_1-W amplitude for water recovered by 16% as the ethanol diffused from the region (c). Reprinted with permission from the American Association of Physicists in Medicine, (150).

Another area of future work is in the monitoring of nanoparticles that are used in conjunction to thermal therapies. For instance, T_2*-lowering superparamagnetic iron oxide (SPIO) particles have been coated with gold at a thickness where it absorbs light in the visible range (~808nm) to deliver thermal therapies (154). The SPIO cores were added to the gold since gold is not MR-detectable but the SPIO cores give effective T_2* contrast. With the multi-parametric capabilities of our CSI technique, we can use the T_2* to possibly determine the concentration of nanoshells to plan the treatment and use the PRF to measure the temperature during the treatment. This CSI technique can also be used to determine if the increase in susceptibility from the SPIOs affect the temperature sensitivity coefficient of water. In addition, this technique has the potential to monitor

156

release of gadolinium from temperature-sensitive liposomes (168). These liposomes release a T_1-shortening gadolinium compound which could be monitored by the T_1-W imaging provided by the CSI technique while at the same time, monitoring temperature changes via the PRF.

Along the same lines of gadolinium release, the simultaneous T_1-W imaging and T_2* mapping makes this technique attractive for simultaneous dynamic contrast enhancement (DCE) and dynamic susceptibility contrast (DSC) imaging. As an example, Figure 7-3 shows maps when a double-bolus of gadolinium was injected into the canine brain under MGE monitoring. The measurements over time are shown in Figure 7-4. Although for now the spatiotemporal resolution is lower with this method compared to other DCE methods, the use of fewer echoes as well as parallel imaging or undersampled reconstruction methods may increase this resolution for efficient estimation for simultaneous DCE and DSC measurements.
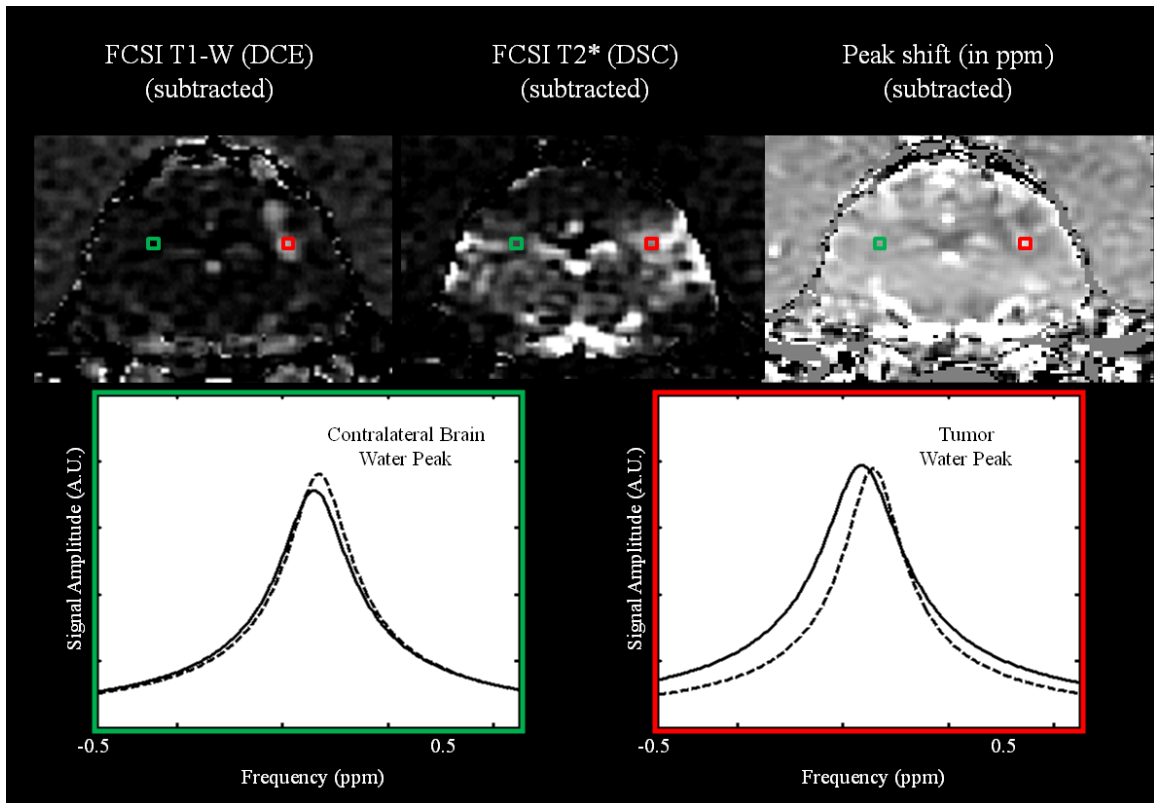
Figure 7-4 PRF, T_2* and T_1-W imaging during contrast injection

The multi-parametric imaging provided by this technique allows simultaneous T_1-W imaging and T_2* mapping while compensating for the field inhomogeneities by calculating the field map. The green box displays a spectrum in normal canine brain parenchyma and the red box displays a spectrum from a transmissible verneal tumor (TVT). In addition to the changes seen in the images, a shift in the PRF and broadening of the linewidth due to T_2* changes are seen when the gadolinium passes the blood-brain barrier.
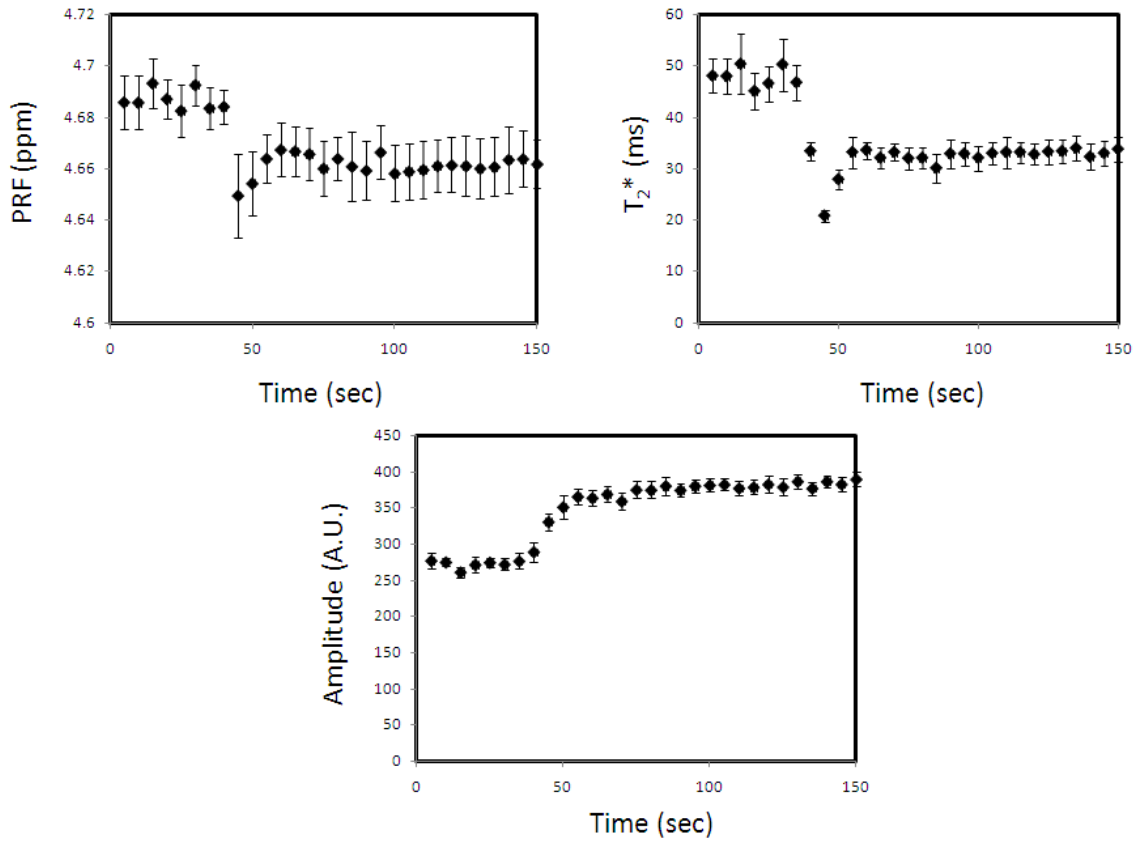
Figure 7-5 PRF, T$_2$* and T$_1$-W measurements during contrast injection

The PRF, T$_2$* and T$_1$-W amplitude of water was measured in 30 consecutive MGE acquisitions over 150 seconds. Upon injection of contrast, there is a PRF shift as well as a decrease in T$_2$* and an increase is the T$_1$-W signal.

Appendix A: The Cramer-Rao Lower Bound for a Sum of Complex, Damped Exponential Functions

The Cramer-Rao lower bound (CRLB) (148, 149) provides the lower bound on the uncertainty of parameter estimates from a certain model. In this research, the model can be described discretely as

$$y(n) = \sum_{k=1}^{M} C_k e^{i\theta_k} e^{-(i2\pi f_k + \alpha_k)n} + w(n) \tag{A.1}$$

where M is the number of damped exponential functions, C_k, θ_k, f_k and α_k is the complex amplitude, zero-order phase, frequency and damping factor, respectively. w is Gaussian noise with zero mean. Each real and imaginary part of w has variance σ^2. If β is the set of parameters that approximates y, then the probability density function for the measurements on the unknown parameter vector, β, can be written as

$$P(y|\beta) = \frac{1}{(2\pi\sigma^2)^N} e^{\left[\frac{-1}{2\sigma^2}\sum_{n=0}^{N-1}\left|y(n)-\sum_{k=1}^{m}C_k e^{i\theta}e^{-(i2\pi f_k+\alpha_k)n}\right|^2\right]} \tag{A.2}$$

where N is the number of samples. The CRLB states that for any unbiased estimate of β, $\hat{\beta}$,

$$Var(\hat{\beta}) \geq \frac{1}{I_{i,j}(\beta)} \tag{A.3}$$

160

where I is the Fisher information matrix defined by

$$I_{i,j}(\beta) = -E\left[\frac{\partial^2}{\partial\beta_i\partial\beta_j}\ln P\left(y|\beta\right)\Big|_\beta\right] \tag{A.4}$$

From these equations, we see that a model can approximate parameters that contain a lower bound in terms of uncertainty as shown in equation A-3. The key to this analysis is to calculate and invert I in order to ascertain the lower bounds. Note that I represents the natural logarithm of the likelihood function and E represents the expectation value. i and j represent each variable approximated by the model. This will result in a 4Mx4M matrix there are four parameters that are to be approximated. The matrix structure is as follows.

$$I = \begin{bmatrix} I_{1,1} & I_{1,2} & I_{1,3} & \cdots & I_{1,4M} \\ I_{1,2}^T & I_{2,2} & I_{2,3} & & \\ I_{1,3}^T & I_{2,3}^T & I_{3,3} & & \vdots \\ \vdots & & & \ddots & \\ I_{1,4M}^T & & \cdots & & I_{4M,4M} \end{bmatrix} \tag{A.5}$$

where T denotes the transpose of the matrix. Along the diagonal, I_{ii} can be expressed as

$$I_{i,i} = \begin{bmatrix} C_i^2 p_{i,i-1} & 0 & C_i^2 p_{i,i} & 0 \\ 0 & p_{i,i-1} & 0 & -C_i p_{i,i} \\ C_i^2 p_{i,1} & 0 & C_i^2 p_{i,i-1} & 0 \\ 0 & -C_i p_{i,i} & 0 & C_i^2 p_{i,i+1} \end{bmatrix} \tag{A.6}$$

where

$$p_{i,j} = \sum_{n=0}^{N} n^j e^{-2\alpha_i n} \tag{A.7}$$

The non-diagonal elements describe the system where peaks interact with each other where

$$I_{ij} = \begin{bmatrix} C_i C_j \gamma_j & C_i q_i & C_i C_j \gamma_i & -C_i C_j \gamma_j \\ -C_j q_i & \gamma_{i-1} & -C_j q_{i-1} & -C_j \gamma_i \\ C_i C_j \gamma_i & C_i q_{i-1} & C_i C_j \gamma_{i-1} & -C_i C_j q_i \\ C_i C_j q_j & -C_i \gamma_i & C_i C_j q_i & C_i C_j \gamma_j \end{bmatrix} \tag{A.8}$$

and

$$\Delta \theta_n = 2\pi \left(f_j - f_i \right) n + \theta_j - \theta_i \tag{A.9}$$

$$\gamma_k = \sum_{n=0}^{N-1} e^{-\left(\alpha_i + \alpha_j\right)n} n^k \cos\left(\Delta\theta_n\right) \tag{A.10}$$

$$q_k = \sum_{n=0}^{N-1} e^{-\left(\alpha_i + \alpha_j\right)n} n^k \sin\left(\Delta\theta_n\right) \tag{A.11}$$

(54). Once I is inverted, the elements in the diagonal can be multiplied by $(\sigma/C_i)^2$ for the CRLB of α_i and C_i and $(\sigma/2\pi C_i)^2$ for f_i. For example, when M=1, the diagonal of I^{-1} can be described analytically to derive the CRLB for each parameter where

$$Var\left(f_1 \right) \geq \frac{\sigma^2}{4\pi^2 C_1^2} \frac{p_{10}}{p_{10} p_{12} - p_{11}^2} \tag{A.12}$$

$$Var(\alpha_1) \geq \frac{\sigma^2}{C_1^2} \frac{p_{10}}{p_{10}p_{12} - p_{11}^2} \qquad \textbf{(A.13)}$$

$$Var\left(\left|C_1 e^{i\theta_1}\right|\right) \geq \frac{\sigma^2}{C_1^2} \frac{p_{12}}{p_{10}p_{12} - p_{11}^2} \qquad \textbf{(A.14)}$$

This analytical solution with M=1 was verified using *Mathematica* (Wolfram Research, Inc., Champaign, IL).

References

1.   Habash, R. W., R. Bansal, D. Krewski, and H. T. Alhafid. 2006. Thermal therapy, part 1: an introduction to thermal therapy. Critical reviews in biomedical engineering 34:459-489.

2.   Seegenschmiedt MH, V. C. 1995. A historical perspective on hyperthermia in oncology. In Thermoradiotherapy and thermochemotherapy. F. P. Seegenschmiedt MH, Vernon CC, editor. Springer Verlag, Berlin. 3-44.

3.   Diederich, C. J. 2005. Thermal ablation and high-temperature thermal therapy: overview of technology and clinical implementation. Int J Hyperthermia 21:745-753.

4.   Dewey, W. C. 1994. Arrhenius relationships from the molecule and cell to the clinic. Int J Hyperthermia 10:457-483.

5.   Cheung, A. Y. 1982. Microwave and radiofrequency techniques for clinical hyperthermia. The British journal of cancer 5:16-24.

6.   Babbs, C. F., and D. P. DeWitt. 1981. Physical principles of local heat therapy for cancer. Medical instrumentation 15:367-373.

7.   Field, S. B., and C. C. Morris. 1983. The relationship between heating time and temperature: its relevance to clinical hyperthermia. Radiother Oncol 1:179-186.

8.   Sapareto, S. A., and W. C. Dewey. 1984. Thermal dose determination in cancer therapy. Int J Radiat Oncol Biol Phys 10:787-800.

9.   Kaouk, J. H., M. Aron, J. C. Rewcastle, and I. S. Gill. 2006. Cryotherapy: clinical end points and their experimental foundations. Urology 68:38-44.

10.   Hildebrandt, B., P. Wust, O. Ahlers, A. Dieing, G. Sreenivasa, T. Kerner, R. Felix, and H. Riess. 2002. The cellular and molecular basis of hyperthermia. Crit Rev Oncol Hematol 43:33-56.

11.   Lepock, J. R., H. E. Frey, and K. P. Ritchie. 1993. Protein denaturation in intact hepatocytes and isolated cellular organelles during heat shock. The Journal of cell biology 122:1267-1276.

12.   Lepock, J. R. 2004. Role of nuclear protein denaturation and aggregation in thermal radiosensitization. Int J Hyperthermia 20:115-130.

13.   Lepock, J. R. 2005. How do cells respond to their thermal environment? Int J Hyperthermia 21:681-687.

14.   Goldstein, L. S., M. W. Dewhirst, M. Repacholi, and L. Kheifets. 2003. Summary, conclusions and recommendations: adverse temperature levels in the human body. Int J Hyperthermia 19:373-384.

15.   Michels, A. A., B. Kanon, A. W. Konings, K. Ohtsuka, O. Bensaude, and H. H. Kampinga. 1997. Hsp70 and Hsp40 chaperone activities in the cytoplasm and the nucleus of mammalian cells. The Journal of biological chemistry 272:33283-33289.

16.   Habash, R. W., R. Bansal, D. Krewski, and H. T. Alhafid. 2006. Thermal therapy, part 2: hyperthermia techniques. Critical reviews in biomedical engineering 34:491-542.

17. Raaphorst, G. P. 1990. Fundamental aspects of hyperthermic biology. In An introduction to the practical aspects of clinical hyperthermia. H. J. Field SB, editor. Taylor & Francis, London. 10-54.

18. Falk, M. H., and R. D. Issels. 2001. Hyperthermia in oncology. Int J Hyperthermia 17:1-18.

19. Hettinga, J. V., W. Lemstra, C. Meijer, N. H. Mulder, A. W. Konings, E. G. de Vries, and H. H. Kampinga. 1994. Hyperthermic potentiation of cisplatin toxicity in a human small cell lung carcinoma cell line and a cisplatin resistant subline. Int J Hyperthermia 10:795-805.

20. Huang, Q., J. K. Hu, F. Lohr, L. Zhang, R. Braun, J. Lanzen, J. B. Little, M. W. Dewhirst, and C. Y. Li. 2000. Heat-induced gene expression as a novel targeted cancer gene therapy strategy. Cancer research 60:3435-3439.

21. Huang, Q., and C. Li. 2001. [Using Hsp70 promoter to regulate target gene expression in tumor]. Zhonghua bing li xue za zhi Chinese journal of pathology 30:198-201.

22. Gerner, E. W., E. M. Hersh, M. Pennington, T. C. Tsang, D. Harris, F. Vasanwala, and J. Brailey. 2000. Heat-inducible vectors for use in gene therapy. Int J Hyperthermia 16:171-181.

23. Lohr, F., K. Hu, Q. Huang, L. Zhang, T. V. Samulski, M. W. Dewhirst, and C. Y. Li. 2000. Enhancement of radiotherapy by hyperthermia-regulated gene therapy. Int J Radiat Oncol Biol Phys 48:1513-1518.

24. Kinuya, S., K. Yokoyama, T. Michigishi, and N. Tonami. 2004. Optimization of radioimmunotherapy interactions with hyperthermia. Int J Hyperthermia 20:190-200.

25. Henriques, F. C. 1947. The predictability and significance of thermally induced rate processes leading to irreversible epidermal injury. Arch Pathol 43:489.

26. Welch, A. J. 1984. The thermal response of laser irradiated tissue. IEEE Journal of Quantum Electronics QE-20:11.

27. Henle, K. J., and L. A. Dethlefsen. 1980. Time-temperature relationships for heat-induced killing of mammalian cells. Annals of the New York Academy of Sciences 335:234-253.

28. Vosburgh, K. G., and F. A. Jolesz. 2003. The concept of image-guided therapy. Acad Radiol 10:176-179.

29. Daniels, M. J., T. Varghese, E. L. Madsen, and J. A. Zagzebski. 2007. Non-invasive ultrasound-based temperature imaging for monitoring radiofrequency heating-phantom results. Phys Med Biol 52:4827-4843.

30. Fallone, B. G., P. R. Moran, and E. B. Podgorsak. 1982. Noninvasive thermometry with a clinical x-ray CT scanner. Med Phys 9:715-721.

31. Salomir, R., F. C. Vimeux, J. A. de Zwart, N. Grenier, and C. T. Moonen. 2000. Hyperthermia by MR-guided focused ultrasound: accurate temperature control based on fast MRI and a physical model of local energy deposition and heat conduction. Magn Reson Med 43:342-347.

32. Denis de Senneville, B., B. Quesson, and C. T. Moonen. 2005. Magnetic resonance temperature imaging. Int J Hyperthermia 21:515-531.

33. Rieke, V., and K. Butts Pauly. 2008. MR thermometry. J Magn Reson Imaging 27:376-390.

34. Hindman, J. C. 1966. Proton resonance shift of water in the gas and liquid states. Journal of Chemical Physics 44:4582-4592.

35. Schneider, W. G., Bernstein, H.J., Pople, J.A. 1958. Proton Magnetic Resonance Chemical Shift of Free (gaseous) and Associated (liquid) Hydride Molecules. J. Chem. Phys. 284:601.

36. de Zwart, J. A., P. van Gelderen, D. J. Kelly, and C. T. Moonen. 1996. Fast magnetic-resonance temperature imaging. J Magn Reson B 112:86-90.

37. Kuroda, K. 2005. Non-invasive MR thermography using the water proton chemical shift. Int J Hyperthermia 21:547-560.

38. Ishihara, Y., A. Calderon, H. Watanabe, K. Okamoto, Y. Suzuki, and K. Kuroda. 1995. A precise and fast temperature mapping using water proton chemical shift. Magn Reson Med 34:814-823.

39. de Senneville, B. D., C. Mougenot, B. Quesson, I. Dragonu, N. Grenier, and C. T. Moonen. 2007. MR thermometry for monitoring tumor ablation. Eur Radiol 17:2401-2410.

40. Kuroda, K., K. Oshio, A. H. Chung, K. Hynynen, and F. A. Jolesz. 1997. Temperature mapping using the water proton chemical shift: a chemical shift selective phase mapping method. Magn Reson Med 38:845-851.

168

41. de Zwart, J. A., F. C. Vimeux, C. Delalande, P. Canioni, and C. T. Moonen. 1999. Fast lipid-suppressed MR temperature mapping with echo-shifted gradient-echo imaging and spectral-spatial excitation. Magn Reson Med 42:53-59.

42. Hynynen, K., O. Pomeroy, D. N. Smith, P. E. Huber, N. J. McDannold, J. Kettenbach, J. Baum, S. Singer, and F. A. Jolesz. 2001. MR imaging-guided focused ultrasound surgery of fibroadenomas in the breast: a feasibility study. Radiology 219:176-185.

43. De Poorter, J. 1995. Noninvasive MRI thermometry with the proton resonance frequency method: study of susceptibility effects. Magn Reson Med 34:359-367.

44. De Poorter, J. D. W., C. De Deene, Y. Thomsen, C. Stahlberg, F. Achten, E. 1994. The proton-resonance-frequency-shift method compared with molecular diffusion for quantitative measurement of two-dimensional time-dependent temperature distribution in a phantom. J Magn Reson B 103:234.

45. McDannold, N., K. Hynynen, K. Oshio, and R. V. Mulkern. 2001. Temperature monitoring with line scan echo planar spectroscopic imaging. Med Phys 28:346-355.

46. Kuroda, K., Y. Suzuki, Y. Ishihara, and K. Okamoto. 1996. Temperature mapping using water proton chemical shift obtained with 3D-MRSI: feasibility in vivo. Magn Reson Med 35:20-29.

47.   Kuroda, K., R. V. Mulkern, K. Oshio, L. P. Panych, T. Nakai, T. Moriya, S. Okuda, K. Hynynen, and F. A. Jolesz. 2000. Temperature mapping using the water proton chemical shift: self-referenced method with echo-planar spectroscopic imaging. Magn Reson Med 43:220-225.

48.   Mulkern, R. V., L. P. Panych, N. J. McDannold, F. A. Jolesz, and K. Hynynen. 1998. Tissue temperature monitoring with multiple gradient-echo imaging sequences. J Magn Reson Imaging 8:493-502.

49.   Candy, J. V. 2006. Model-Based Signal Processing. John Wiley & Sons, Inc., Hoboken, NJ.

50.   Koehl, P. 1999. Linear Prediction Spectral Analysis of NMR Data. Progress in Nuclear Magnetic Resonance Spectroscopy 34:257-299.

51.   Belkic, D., and K. Belkic. 2005. The fast Pade transform in magnetic resonance spectroscopy for potential improvements in early cancer diagnostics. Phys Med Biol 50:4385-4408.

52.   Williamson, D. C., Hawesa, H., Thacker, N.A., Williams, S.R. 2006. Robust Quantification of Short Echo Time 1H Magneic Resonance Spectra using the Pade' Approximant. Magnetic Reson Med:762-771.

53.   Taylor, B. A., K. P. Hwang, A. M. Elliott, A. Shetty, J. D. Hazle, and R. J. Stafford. 2008. Dynamic chemical shift imaging for image-guided thermal therapy: analysis of feasibility and potential. Med Phys 35:793-803.

54. Kumaresan, R., Tufts D.W., . 1982. Estimating the Parameters of Exponentially Damped Sinusoids and Pole-Zero Modeling in Noise. IEEE Trans Acoustics, Speech, Sig, Processing 30:833-840.

55. Bammer, R. 2003. Basic principles of diffusion-weighted imaging. Eur J Radiol 45:169-184.

56. Morvan, D., A. Leroy-Willig, A. Malgouyres, C. A. Cuenod, P. Jehenson, and A. Syrota. 1993. Simultaneous temperature and regional blood volume measurements in human muscle using an MRI fast diffusion technique. Magn Reson Med 29:371-377.

57. Bleier, A. R., F. A. Jolesz, M. S. Cohen, R. M. Weisskoff, J. J. Dalcanton, N. Higuchi, D. A. Feinberg, B. R. Rosen, R. C. McKinstry, and S. G. Hushek. 1991. Real-time magnetic resonance imaging of laser heat deposition in tissue. Magn Reson Med 21:132-137.

58. Moseley, M. E., Y. Cohen, J. Mintorovitch, L. Chileuitt, H. Shimizu, J. Kucharczyk, M. F. Wendland, and P. R. Weinstein. 1990. Early detection of regional cerebral ischemia in cats: comparison of diffusion- and T2-weighted MRI and spectroscopy. Magn Reson Med 14:330-346.

59. Johnson, F. E., H. Stover, B. 1974. Theory of rate processes in biology and medicine. John Wiley & Sons, New York, NY.

60. Chen, J., B. L. Daniel, and K. B. Pauly. 2006. Investigation of proton density for measuring tissue temperature. J Magn Reson Imaging 23:430-434.

61. Gultekin, D. H., and J. C. Gore. 2005. Temperature dependence of nuclear magnetization and relaxation. J Magn Reson 172:133-141.

62. Bloembergen, N. P., E.M. Pound, R.V. . 1948. Relaxation effects in nuclear magnetic resonance absorption. Phys Rev 73:679-712.

63. Matsumoto, R., R. V. Mulkern, S. G. Hushek, and F. A. Jolesz. 1994. Tissue temperature monitoring for thermal interventional therapy: comparison of T1-weighted MR sequences. J Magn Reson Imaging 4:65-70.

64. Parker, D. L., V. Smith, P. Sheldon, L. E. Crooks, and L. Fussell. 1983. Temperature distribution measurements in two-dimensional NMR imaging. Med Phys 10:321-325.

65. Hynynen, K., N. McDannold, R. V. Mulkern, and F. A. Jolesz. 2000. Temperature monitoring in fat with MRI. Magn Reson Med 43:901-904.

66. Matsumoto, R., K. Oshio, and F. A. Jolesz. 1992. Monitoring of laser and freezing-induced ablation in the liver with T1-weighted MR imaging. J Magn Reson Imaging 2:555-562.

67. Lewa, C. J., and Z. Majewska. 1980. Temperature relationships of proton spin-lattice relaxation time T1 in biological tissues. Bulletin du cancer 67:525-530.

68. Cline, H. E., K. Hynynen, C. J. Hardy, R. D. Watkins, J. F. Schenck, and F. A. Jolesz. 1994. MR temperature mapping of focused ultrasound surgery. Magn Reson Med 31:628-636.

69. Peller, M., H. M. Reinl, A. Weigel, M. Meininger, R. D. Issels, and M. Reiser. 2002. T1 relaxation time at 0.2 Tesla for monitoring regional hyperthermia: feasibility study in muscle and adipose tissue. Magn Reson Med 47:1194-1201.

70. Graham, S. J., M. J. Bronskill, and R. M. Henkelman. 1998. Time and temperature dependence of MR parameters during thermal coagulation of ex vivo rabbit muscle. Magn Reson Med 39:198-203.

71. Wolff, S. D., and R. S. Balaban. 1989. Magnetization transfer contrast (MTC) and tissue water proton relaxation in vivo. Magn Reson Med 10:135-144.

72. Young, I. R., J. W. Hand, A. Oatridge, and M. V. Prior. 1994. Modeling and observation of temperature changes in vivo using MRI. Magn Reson Med 32:358-369.

73. Graham, S. J., G. J. Stanisz, A. Kecojevic, M. J. Bronskill, and R. M. Henkelman. 1999. Analysis of changes in MR properties of tissues after heat treatment. Magn Reson Med 42:1061-1071.

74. Haacke, E. M., R. W. Brown, M. R. Thompson, and R. Venkatesan. 1999. Magnetic Resonance Imaging : Physical Principles and Sequence Design. John Wiley & Sons, Inc., New York City, NY.

75. McDannold, N. 2005. Quantitative MRI-based temperature mapping based on the proton resonant frequency shift: review of validation studies. Int J Hyperthermia 21:533-546.

76. Peters, R. D., R. S. Hinks, and R. M. Henkelman. 1999. Heat-source orientation and geometry dependence in proton-resonance frequency shift magnetic resonance thermometry. Magn Reson Med 41:909-918.

77. Peters, R. D., and R. M. Henkelman. 2000. Proton-resonance frequency shift MR thermometry is affected by changes in the electrical conductivity of tissue. Magn Reson Med 43:62-71.

78. McDannold, N. J., R. L. King, F. A. Jolesz, and K. H. Hynynen. 2000. Usefulness of MR imaging-derived thermometry and dosimetry in determining the threshold for tissue damage induced by thermal surgery in rabbits. Radiology 216:517-523.

79. Peters, R. D., R. S. Hinks, and R. M. Henkelman. 1998. Ex vivo tissue-type independence in proton-resonance frequency shift MR thermometry. Magn Reson Med 40:454-459.

80. Cady, E. B., P. C. D'Souza, J. Penrice, and A. Lorek. 1995. The estimation of local brain temperature by in vivo 1H magnetic resonance spectroscopy. Magn Reson Med 33:862-867.

81. Corbett, R. J., A. R. Laptook, G. Tollefsbol, and B. Kim. 1995. Validation of a noninvasive method to measure brain temperature in vivo using 1H NMR spectroscopy. Journal of neurochemistry 64:1224-1230.

82. Conturo, T. E., and G. D. Smith. 1990. Signal-to-noise in phase angle reconstruction: dynamic range extension using phase reference offsets. Magn Reson Med 15:420-437.

83.   Stafford, R. J., R. E. Price, C. J. Diederich, M. Kangasniemi, L. E. Olsson, and J. D. Hazle. 2004. Interleaved echo-planar imaging for fast multiplanar magnetic resonance temperature imaging of ultrasound thermal ablation therapy. J Magn Reson Imaging 20:706-714.

84.   Morikawa, S., T. Inubushi, Y. Kurumi, S. Naka, K. Sato, K. Demura, T. Tani, and H. A. Haque. 2004. Feasibility of respiratory triggering for MR-guided microwave ablation of liver tumors under general anesthesia. Cardiovascular and interventional radiology 27:370-373.

85.   Lepetit-Coiffe, M., B. Quesson, O. Seror, E. Dumont, B. Le Bail, C. T. Moonen, and H. Trillaud. 2006. Real-time monitoring of radiofrequency ablation of rabbit liver by respiratory-gated quantitative temperature MRI. J Magn Reson Imaging 24:152-159.

86.   Rieke, V., K. K. Vigen, G. Sommer, B. L. Daniel, J. M. Pauly, and K. Butts. 2004. Referenceless PRF shift thermometry. Magn Reson Med 51:1223-1231.

87.   Young, I. R., J. V. Hajnal, I. G. Roberts, J. X. Ling, R. J. Hill-Cottingham, A. Oatridge, and J. A. Wilson. 1996. An evaluation of the effects of susceptibility changes on the water chemical shift method of temperature measurement in human peripheral muscle. Magn Reson Med 36:366-374.

88.   El-Sharkawy, A. M., M. Schar, P. A. Bottomley, and E. Atalar. 2006. Monitoring and correcting spatio-temporal variations of the MR scanner's static magnetic field. Magma (New York, N.Y 19:223-236.

89. De Poorter, J., C. De Wagter, Y. De Deene, C. Thomsen, F. Stahlberg, and E. Achten. 1995. Noninvasive MRI thermometry with the proton resonance frequency (PRF) method: in vivo results in human muscle. Magn Reson Med 33:74-81.

90. Das, S. K., J. Macfall, R. McCauley, O. Craciunescu, M. W. Dewhirst, and T. V. Samulski. 2005. Improved magnetic resonance thermal imaging by combining proton resonance frequency shift (PRFS) and apparent diffusion coefficient (ADC) data. Int J Hyperthermia 21:657-667.

91. Hussain, K., and H. B. El-Serag. 2009. Epidemiology, screening, diagnosis and treatment of hepatocellular carcinoma. Minerva gastroenterologica e dietologica 55:123-138.

92. Mulkern, R. V., A. H. Chung, F. A. Jolesz, and K. Hynynen. 1997. Temperature monitoring of ultrasonically heated muscle with RARE chemical shift imaging. Med Phys 24:1899-1906.

93. McDannold, N., A. S. Barnes, F. J. Rybicki, K. Oshio, N. K. Chen, K. Hynynen, and R. V. Mulkern. 2007. Temperature mapping considerations in the breast with line scan echo planar spectroscopic imaging. Magn Reson Med 58:1117-1123.

94. Bankson, J. A., R. J. Stafford, and J. D. Hazle. 2005. Partially parallel imaging with phase-sensitive data: Increased temporal resolution for magnetic resonance temperature imaging. Magn Reson Med 53:658-665.

95.   Du, W., Y. P. Du, X. Fan, M. A. Zamora, and G. S. Karczmar. 2003. Reduction of spectral ghost artifacts in high-resolution echo-planar spectroscopic imaging of water and fat resonances. Magn Reson Med 49:1113-1120.

96.   Lu, W., H. Yu, A. Shimakawa, M. Alley, S. B. Reeder, and B. A. Hargreaves. 2008. Water-fat separation with bipolar multiecho sequences. Magn Reson Med 60:198-209.

97.   Mansfield, P. 1984. Spatial mapping of the chemical shift in NMR. Magn Reson Med 1:370-386.

98.   Posse, S., G. Tedeschi, R. Risinger, R. Ogg, and D. Le Bihan. 1995. High speed 1H spectroscopic imaging in human brain by echo planar spatial-spectral encoding. Magn Reson Med 33:34-40.

99.   Duyn, J. H., and C. T. Moonen. 1993. Fast proton spectroscopic imaging of human brain using multiple spin-echoes. Magn Reson Med 30:409-414.

100.   Mulkern, R. V., H. Chao, J. L. Bowers, and D. Holtzman. 1997. Multiecho approaches to spectroscopic imaging of the brain. Annals of the New York Academy of Sciences 820:97-122.

101.   Oshio, K., W. Kyriakos, and R. V. Mulkern. 2000. Line scan echo planar spectroscopic imaging. Magn Reson Med 44:521-524.

102.   Bonekamp, D., M. A. Smith, H. Zhu, and P. B. Barker. 2010. Quantitative SENSE-MRSI of the human brain. Magn Reson Imaging 28:305-313.

103. Tsai, S. Y., R. Otazo, S. Posse, Y. R. Lin, H. W. Chung, L. L. Wald, G. C. Wiggins, and F. H. Lin. 2008. Accelerated proton echo planar spectroscopic imaging (PEPSI) using GRAPPA with a 32-channel phased-array coil. Magn Reson Med 59:989-998.

104. Hu, S., M. Lustig, A. P. Chen, J. Crane, A. Kerr, D. A. Kelley, R. Hurd, J. Kurhanewicz, S. J. Nelson, J. M. Pauly, and D. B. Vigneron. 2008. Compressed sensing for resolution enhancement of hyperpolarized 13C flyback 3D-MRSI. J Magn Reson 192:258-264.

105. Hu, S., M. Lustig, A. Balakrishnan, P. E. Larson, R. Bok, J. Kurhanewicz, S. J. Nelson, A. Goga, J. M. Pauly, and D. B. Vigneron. 2010. 3D compressed sensing for highly accelerated hyperpolarized (13)C MRSI with in vivo applications to transgenic mouse models of cancer. Magn Reson Med 63:312-321.

106. Abragam, A. 1961. The Principles of Nuclear Magnetism. Clarendon Press, Oxford.

107. Hoch, J. C. S., A.S. 1996. NMR Data Processing. Wiley-Liss, New York.

108. Bracewell, R. 1978. The Fourier Transform and its Applications. McGraw-Hill, Inc., New York.

109. Vanhamme, L., T. Sundin, P. V. Hecke, and S. V. Huffel. 2001. MR spectroscopy quantitation: a review of time-domain methods. NMR in biomedicine 14:233-246.

110. van der Veen, J. W., R. de Beer, P. R. Luyten, and D. van Ormondt. 1988. Accurate quantification of in vivo 31P NMR signals using the variable projection method and prior knowledge. Magn Reson Med 6:92-98.

111. Vanhamme, L., A. van den Boogaart, and S. Van Huffel. 1997. Improved method for accurate and efficient quantification of MRS data with use of prior knowledge. J Magn Reson 129:35-43.

112. Osborne, M. 1972. Some aspects of non-linear least squares calculatons. . In Numerical Methods for Non-linear Optimization. Academic Press, London.

113. Poullet, J. B., D. M. Sima, and S. Van Huffel. 2008. MRS signal quantitation: a review of time- and frequency-domain methods. J Magn Reson 195:134-144.

114. Sandgren, N., Y. Selen, P. Stoica, and J. Li. 2004. Parametric methods for frequency-selective MR spectroscopy-a review. J Magn Reson 168:259-272.

115. de Graaf, A. A., and W. M. Bovee. 1990. Improved quantification of in vivo 1H NMR spectra by optimization of signal acquisition and processing and by incorporation of prior knowledge into the spectral fitting. Magn Reson Med 15:305-319.

116. Marshall, I., J. Higinbotham, S. Bruce, and A. Freise. 1997. Use of Voigt lineshape for quantification of in vivo 1H spectra. Magn Reson Med 37:651-657.

117. Belkic, D. 2005. Quantum-Mechanical Signal Processing and Spectral Analysis. Institute of Physics Publishing, London.

118. Belkic, D. 2006. Exponential convergence rate (the spectral convergence) of the fast Pade transform for exact quantification in magnetic resonance spectroscopy. Phys Med Biol 51:6483-6512.

119. Barbosa, R. S. T. M., J.A.; Silva, M.F. 2006. Time domain design of fractional differintegrators using least-squares. Signal Processing 86:2567-2581.

120. Jackson, L. B. 1996. Digital Filters and Signal Processing with Matlab Exercises. Kulwer Academic Publishers.

121. Steiglitz, K., and L. McBride. 1965. A technique for the identification of linear systems. IEEE Transactions on Automatic Control 10:461-464.

122. Amindavar, H., and A. M. Reza. 2005. A New Simultaneous Estimation of Directions of Arrival and Channel Parameters in a Multipath Environment. IEEE Transactions on Signal Processing 53:471-483.

123. Kwock, L., J. K. Smith, M. Castillo, M. G. Ewend, F. Collichio, D. E. Morris, T. W. Bouldin, and S. Cush. 2006. Clinical role of proton magnetic resonance spectroscopy in oncology: brain, breast, and prostate cancer. The lancet oncology 7:859-868.

124. Haase, A., J. Frahm, W. Hanicke, and D. Matthaei. 1985. 1H NMR chemical shift selective (CHESS) imaging. Phys Med Biol 30:341-344.

125. Schick, F. 1998. Simultaneous highly selective MR water and fat imaging using a simple new type of spectral-spatial excitation. Magn Reson Med 40:194-202.

126. Bydder, G. M., J. M. Pennock, R. E. Steiner, S. Khenia, J. A. Payne, and I. R. Young. 1985. The short TI inversion recovery sequence--an approach to MR imaging of the abdomen. Magn Reson Imaging 3:251-254.

127. Dixon, W. T. 1984. Simple proton spectroscopic imaging. Radiology 153:189-194.

128. Glover, G. H., and E. Schneider. 1991. Three-point Dixon technique for true water/fat decomposition with B0 inhomogeneity correction. Magn Reson Med 18:371-383.

129. Bley, T. A., O. Wieben, C. J. Francois, J. H. Brittain, and S. B. Reeder. 2010. Fat and water magnetic resonance imaging. J Magn Reson Imaging 31:4-18.

130. Skinner, T. E., and G. H. Glover. 1997. An extended two-point Dixon algorithm for calculating separate water, fat, and B0 images. Magn Reson Med 37:628-630.

131. Coombs, B. D., J. Szumowski, and W. Coshow. 1997. Two-point Dixon technique for water-fat signal decomposition with B0 inhomogeneity correction. Magn Reson Med 38:884-889.

132. Ma, J. 2008. A single-point Dixon technique for fat-suppressed fast 3D gradient-echo imaging with a flexible echo time. J Magn Reson Imaging 27:881-890.

133. Xiang, Q. S., and L. An. 1997. Water-fat imaging with direct phase encoding. J Magn Reson Imaging 7:1002-1015.

134. Ma, J., J. B. Son, J. A. Bankson, R. J. Stafford, H. Choi, and D. Ragan. 2005. A fast spin echo two-point Dixon technique and its combination with sensitivity encoding for efficient T2-weighted imaging. Magn Reson Imaging 23:977-982.

135. Ma, J. 2004. Breath-hold water and fat imaging using a dual-echo two-point Dixon technique with an efficient and robust phase-correction algorithm. Magn Reson Med 52:415-419.

136. Ma, J., C. M. Costelloe, J. E. Madewell, G. N. Hortobagyi, M. C. Green, G. Cao, F. Sun, and V. Kundra. 2009. Fast dixon-based multisequence and multiplanar MRI for whole-body detection of cancer metastases. J Magn Reson Imaging 29:1154-1162.

137. Reeder, S. B., A. R. Pineda, Z. Wen, A. Shimakawa, H. Yu, J. H. Brittain, G. E. Gold, C. H. Beaulieu, and N. J. Pelc. 2005. Iterative decomposition of water and fat with echo asymmetry and least-squares estimation (IDEAL): application with fast spin-echo imaging. Magn Reson Med 54:636-644.

138. Yu, H., C. A. McKenzie, A. Shimakawa, A. T. Vu, A. C. Brau, P. J. Beatty, A. R. Pineda, J. H. Brittain, and S. B. Reeder. 2007. Multiecho reconstruction for simultaneous water-fat decomposition and T2* estimation. J Magn Reson Imaging 26:1153-1161.

139. Yu, H., A. Shimakawa, C. A. McKenzie, E. Brodsky, J. H. Brittain, and S. B. Reeder. 2008. Multiecho water-fat separation and simultaneous R2* estimation with multifrequency fat spectrum modeling. Magn Reson Med 60:1122-1134.

140. Srinivasan, A., C. J. Galban, T. D. Johnson, T. L. Chenevert, B. D. Ross, and S. K. Mukherji. 2010. Utility of the k-means clustering algorithm in differentiating apparent diffusion coefficient values of benign and malignant neck pathologies. Ajnr 31:736-740.

141. Deoni, S. C., B. K. Rutt, A. G. Parrent, and T. M. Peters. 2007. Segmentation of thalamic nuclei using a modified k-means clustering algorithm and high-resolution quantitative magnetic resonance imaging at 1.5 T. NeuroImage 34:117-126.

142. Filzmoser, P., R. Baumgartner, and E. Moser. 1999. A hierarchical clustering method for analyzing functional MR images. Magn Reson Imaging 17:817-826.

143. Carano, R. A., A. L. Ross, J. Ross, S. P. Williams, H. Koeppen, R. H. Schwall, and N. Van Bruggen. 2004. Quantification of tumor tissue populations by multispectral analysis. Magn Reson Med 51:542-551.

144. Lloyd, S. P. 1982. Least squares quantization in PCM. IEEE Transactions on Information Theory 28:129-137.

145. MacQueen, J. B. 1967. Some methods for classification and analysis of multivariate observations. In Fifth Berkeley Symposium on Mathematical Statistics and Probability. University of California Press. 281-297.

146. Landini, L., Positano, V, Santarelli, MF. 2005. Advanced Image Processing in Magnetic Resonance Imaging. Taylor and Francis, Boca Raton, FL.

147. Johnson, R. 2000. Miller and Freund's Probability and Statistics for Engineers. Prentice Hall, Upper Saddle River, NJ.

148. Cramer, H. 1946. Mathematical Methods of Statistics. Princeton Univ. Press.

149. Rao, C. 1945. Information and the accuracy attainable in the estimation of statistical parameters. Bull. Calcutta Math. Soc. 37:81-89.

150.   Taylor, B. A., K. P. Hwang, J. D. Hazle, and R. J. Stafford. 2009. Autoregressive Moving Average Modeling for Spectral Parameter Estimation from a Multi-Gradient Echo Chemical Shift Acquisition. Med Phys 36:753-764.

151.   Oude Engberink, R. D., S. M. van der Pol, E. A. Dopp, H. E. de Vries, and E. L. Blezer. 2007. Comparison of SPIO and USPIO for in vitro labeling of human monocytes: MR detection and cell function. Radiology 243:467-474.

152.   Shmatukha, A. V., P. R. Harvey, and C. J. Bakker. 2007. Correction of proton resonance frequency shift temperature maps for magnetic field disturbances using fat signal. J Magn Reson Imaging 25:579-587.

153.   Akhlaghpoor, S., A. Tomasian, A. Arjmand Shabestari, M. Ebrahimi, and M. R. Alinaghizadeh. 2007. Percutaneous osteoid osteoma treatment with combination of radiofrequency and alcohol ablation. Clinical radiology 62:268-273.

154.   Ji, X. S., R; Elliott, A.M.; Stafford, R.J.; Esparza-Coss, E.; Bankson, J.A., Liang, G; Luo Z.P.; Park, K.; Markert, J.T.; Li, C. . 2007. Bifunctional gold nanoshells with a superparamagnetic iron oxide-silica core suitable for both MR imaging and photothermal therapy J. Phys. Chem. C. 111:6245-6251.

155.   Machann, J., N. Stefan, and F. Schick. 2008. (1)H MR spectroscopy of skeletal muscle, liver and bone marrow. Eur J Radiol 67:275-284.

156.   Schick, F. 1996. Bone marrow NMR in vivo. J Prog Nuc Mag Spect 29:169-227.

157.   Chen, L., J. P. Wansapura, G. Heit, and K. Butts. 2002. Study of laser ablation in the in vivo rabbit brain with MR thermometry. J Magn Reson Imaging 16:147-152.

158.	Rieke, V., A. B. Ross, W. H. Nau, C. J. Diederich, G. Sommer, and K. Butts. 2004. MRI-temperature mapping during ultrasound prostate ablation using fat for phase estimation. Conf Proc IEEE Eng Med Biol Soc 4:2500-2502.

159.	Carpentier, A., R. J. McNichols, R. J. Stafford, J. Itzcovitz, J. P. Guichard, D. Reizine, S. Delaloge, E. Vicaut, D. Payen, A. Gowda, and B. George. 2008. Real-time magnetic resonance-guided laser thermal therapy for focal metastatic brain tumors. Neurosurgery 63:ONS21-28; discussion ONS28-29.

160.	McNichols, R. J., A. Gowda, M. Kangasniemi, J. A. Bankson, R. E. Price, and J. D. Hazle. 2004. MR thermometry-based feedback control of laser interstitial thermal therapy at 980 nm. Lasers in surgery and medicine 34:48-55.

161.	Mallamace, F., S. H. Chen, M. Broccio, C. Corsaro, V. Crupi, D. Majolino, V. Venuti, P. Baglioni, E. Fratini, C. Vannucci, and H. E. Stanley. 2007. Role of the solvent in the dynamical transitions of proteins: the case of the lysozyme-water system. The Journal of chemical physics 127:045104.

162.	Bouchard, L. S., and M. J. Bronskill. 2000. Magnetic resonance imaging of thermal coagulation effects in a phantom for calibrating thermal therapy devices. Med Phys 27:1141-1145.

163.	Dice, L. R. 1945. Measures of the amount of ecologic association between species. Ecology 26:297-302.

164.	Li, C., X. Pan, K. Ying, Q. Zhang, J. An, D. Weng, W. Qin, and K. Li. 2009. An internal reference model-based PRF temperature mapping method with Cramer-Rao lower bound noise performance analysis. Magn Reson Med 62:1251-1260.

165. Rieke, V., A. M. Kinsey, A. B. Ross, W. H. Nau, C. J. Diederich, G. Sommer, and K. B. Pauly. 2007. Referenceless MR thermometry for monitoring thermal ablation in the prostate. IEEE Trans Med Imaging 26:813-821.

166. Bischof, J. C., J. Padanilam, W. H. Holmes, R. M. Ezzell, R. C. Lee, R. G. Tompkins, M. L. Yarmush, and M. Toner. 1995. Dynamics of cell membrane permeability changes at supraphysiological temperatures. Biophysical journal 68:2608-2614.

167. Poon, R. T., S. T. Fan, F. H. Tsang, and J. Wong. 2002. Locoregional therapies for hepatocellular carcinoma: a critical review from the surgeon's perspective. Annals of surgery 235:466-486.

168. Peller, M., A. Schwerdt, M. Hossann, H. M. Reinl, T. Wang, S. Sourbron, M. Ogris, and L. H. Lindner. 2008. MR characterization of mild hyperthermia-induced gadodiamide release from thermosensitive liposomes in solid tumors. Invest Radiol 43:877-892.

Vita

Brian Allen Taylor, son of Ricky and Rosemarie Taylor, was born in Hayti, Missouri, on January 25, 1983. He is the brother of Aaron Taylor. After graduating from Portageville High School in 2001, Brian attended Union University in Jackson, Tennessee, where he earned the Bachelor of Science degree with a double-major in Mathematics and Physics. In 2005, Brian matriculated into the Medical Physics program at the University of Texas Graduate School of Biomedical Sciences at Houston.

Permanent Address:

4554 State Highway F
Portageville, MO 63873